Developing a Large-Scale, Programmable Trapped Ion Quantum Simulator with In Situ Mid-Circuit Measurement and Reset

by

Sainath Motlakunta

A thesis
presented to the University of Waterloo
in fulfillment of the
thesis requirement for the degree of
Doctor of Philosophy
in
Physics (Quantum Information)

Waterloo, Ontario, Canada, 2023

Examining Committee Membership

The following served on the Examining Committee for this thesis. The decision of the Examining Committee is by majority vote.

External Examiner:	Joseph H. Thywissen Professor of Physics, University of Toronto
Supervisor(s):	Kazi Rajibul Islam Associate professor, Dept. of Physics and Astronomy, University of Waterloo
Internal Member:	Christine Muschik Associate Professor, Dept. of Physics and Astronomy, University of Waterloo
Internal Member:	Raffi Budakian Professor, Dept. of Physics and Astronomy, University of Waterloo
Internal-External Member:	Michal Bajcsy Associate Professor, Dept. of Physics and Astronomy, University of Waterloo

Author's Declaration

I hereby declare that I am the sole author of this thesis. This is a true copy of the thesis, including any required final revisions, as accepted by my examiners.

I understand that my thesis may be made electronically available to the public.

Abstract

Quantum simulators are a valuable resource for studying complex many-body systems. With their ability to provide near-term advantages, analog quantum simulators show great promise. In this thesis, my aim is to describe the construction of a large-scale trapped-ion based analog quantum simulator with several objectives in mind: controllability, minimal external decoherence, an expandable toolkit for quantum simulations, enhanced stability through robust design practices, and pushing the boundaries of error correction.

One of the techniques that significantly expands the range of simulations possible in trapped ions is site-selective mid-circuit measurements and resets. This technique enables the exploration of new classes of quantum simulations, including measurement-based phase transitions and reservoir engineering with controlled dissipation. Additionally, mid-circuit measurements play a crucial role and serve as one of the key factors in achieving error-correction in trapped ions. In this thesis, I address the challenges associated with implementing mid-circuit measurements and discuss strategies for achieving state-of-the-art fidelities in these processes within our simulator.

In this thesis, I present the results demonstrating the high-fidelity preservation of an "asset" ion qubit while simultaneously resetting or measuring a neighboring "process" qubit located a few microns away. The results show that we achieve a probability of accidental measurement of the asset qubit below 1×10^{-3} while resetting the process qubit. Similarly, when applying a detection beam on the same neighboring qubit to achieve fast detection times, the probability remains below 4×10^{-3} at a distance of 6 μm, which is four times the addressing Gaussian beam waist. These low probabilities correspond to the preservation of the quantum state of the asset qubit with fidelities above 99.9% for state reset and 99.6% for state measurement.

One of the many fascinating aspects of physics that can be explored through the use of site-selective mid-circuit resets is reservoir engineering. In this thesis, I discuss a protocol utilizing reservoir engineering to efficiently cool the spin state of a subsystem that is coupled to a reservoir with controlled dissipation. I demonstrate the effectiveness of this protocol through numerical simulations performed to optimize it for our experimental parameters. By leveraging the site-selective mid-circuit resets mentioned earlier, I successfully conduct a proof-of-principle dissipative many-body cooling experiment based on reservoir engineering. Through analog quantum simulation, I am able to demonstrate the lowering of energy within the system.

In addition to the above explorations, another important aspect of this thesis is the description of the design, fabrication, and assembly of a large-scale trapped ion quantum

simulator called the Blade trap. I discuss the essential features of this system that include accommodating a significant number of ions, extending ion lifetimes and coherence times, enabling precise control of ion spins and interactions, implementing efficient detection methods, and incorporating mid-circuit measurement capabilities. I also provide a detailed account of our approach to optimizing the design and fabrication of the blade-trap system, covering the trap itself, mechanical components, system internals, optics, and the critical ultra-high vacuum (UHV) assembly. Furthermore, comprehensive testing procedures are presented to evaluate the performance and stability of the Blade trap.

I also describe the details about one of the significant challenge we faced in achieving and maintaining ultra-low pressure levels in the UHV system to ensure uninterrupted quantum simulation experiments with around 50 ions. High pressures can lead to detrimental collisions between ions and background atoms, necessitating re-trapping and introducing substantial overhead. Therefore, we aimed to achieve pressures in the range of 5×10^{-13} to 1×10^{-12} mbar at room temperature, demanding meticulous optimization at the component level. Our journey to attain these pressures took approximately 2 to 3 years, complicated further by COVID-19 restrictions and equipment malfunctions. Despite the exhausting efforts, we successfully reached base pressures of less than 9×10^{-13} mbar in the vacuum chamber with partial internals. It is important to note that this measurement represents an upper limit due to gauge limitations.

Acknowledgements

Firstly, I would like to express my heartfelt gratitude to my supervisor, Kazi Rajibul Islam, for his invaluable support throughout my entire PhD journey. His guidance, encouragement, and expertise have played a pivotal role in shaping my research and personal growth. Starting a new research group is indeed a significant challenge, and Rajibul has done an outstanding job in steering the lab in the right direction. He has dedicated meticulous attention to shaping both the future of our research endeavors and fostering a collaborative lab culture that is not only productive but also enjoyable to work within. Rajibul possesses a unique blend of scientific knowledge and emotional intelligence. He consistently ensures that everyone participating in discussions or meetings has at least a basic understanding, even if they are first-year undergraduates. I have had the privilege of learning a great deal from working with him, whether it is in solving complex research problems from a simple bottom-up approach or assisting with his coursework.

I would also like to extend my thanks to Dr. Joseph Thywissen for his role as my external examiner. I deeply appreciate his willingness to dedicate his time to provide me with invaluable insights and corrections for my thesis. His thought-provoking questions during my defense presentation were particularly enlightening. Furthermore, I am grateful for the time he spent with me after the defense, explaining the systematic issues in my thesis and offering guidance on improving my writing.

Furthermore, I extend my deepest gratitude to my esteemed committee members: Dr. Christine Muschik, Dr. Michal Bajcsy, and Dr. Raffi Budakian. Their valuable contributions and insights have been indispensable throughout my PhD journey. Their expertise, constructive criticism, and collaborative spirit have played a pivotal role in the successful completion of my doctoral work. I always eagerly anticipated the questions they would pose during our meetings. It never ceased to amuse me how, from a brief presentation by me during committee meetings and my defense, they would generate thought-provoking questions that showcased their profound expertise in the field of quantum physics. This process immensely aided me in gaining fresh insights into my research from an outsider's perspective.

I am also thankful for the opportunity to work with various theory collaborators, including Dr. Jim Freericks and Dr. Azadeh Mazloom. They not only assisted me in exploring new kinds of problems that could be solved with our experiments but also helped me gain a deeper understanding of many-body physics.

I would like to express my gratitude to my QITI (Quantum Information with Trapped Ions) family, with whom I spent most of my PhD journey. It was a great pleasure working

alongside them, and I eagerly anticipated each day in the lab. Completing this thesis would have been impossible without their invaluable contributions. I extend my heartfelt thanks to my fellow graduate students: Nikhil Kotibhakar, Chung-You (Gilbert) Shih, Manas Sajjan, Anthony Vogliano, Lewis Hahn, Jingwen (Monica) Zhu, and the postdocs Roland Hablützel, Fereshte Rajabi, and Yu-Ting Chen from the QSim group. One of the most memorable moments of my PhD journey was when we successfully trapped the ions for the first time, alongside Nikhil, Gilbert, Manas, and Roland. The excitement we all felt on that occasion remains etched in my memory. Nikhil and Gilbert were not just exceptional lab partners but also wonderful friends. We had a lot of fun setting up and occasionally dismantling the lab. Nikhil and I spent a significant amount of time on vacuum assembly, meticulously planning each step in detail before commencing. It was an enjoyable experience devising these plans with him, even though they were sometimes quite ambitious for a single day's work. Every now and then, distant ducks in a pond would seem to mock our plans with their loud laughter. I learned a great deal from working with Nikhil, especially his constant drive to solving new and intriguing problems and his eagerness to constantly acquire new knowledge. Gilbert, with his boundless energy, taught me the importance of exploring unconventional solutions to arrive at answers quickly. I am grateful for the insightful conversations I had with Anthony and Roland, encompassing both physics and life in general. Lewis's strong work ethic and Monica's laid-back attitude left lasting impressions on me. Fereshte has been both an inspiration and a dear friend, her fearless approach to achieving her goals serving as a constant source of motivation for me. Yu-Ting, who joined during the latter part of my PhD journey, has been a pleasure to work with, thanks to her calm attitude. I would also like to thank Nikhil, Anthony, and Lewis for helping me proofread parts of my thesis.

I had lots of fun working with various undergraduates and research assistants Sakshee, Gaurav, Ashley, Alisa, Frank, Josh, Austin, Duale, Natasha, Daniel and many others who brought their fresh energy and perspective in solving various difficult problems. I was impressed by how mature their thought processes were given their young age.

I would also like to extend my gratitude to Dr. Crystal Senko and the graduate students from her group, including Brendan White, Pei-Jiang Low, Noah Greenberg, and Rich Rademacher. Their ongoing efforts in the field of experiments on trapped ions have been a constant source of inspiration for me. Additionally, our exchange of knowledge and lab tools has been invaluable to our work.

Starting almost from scratch in our experimental AMO lab, I constantly faced the challenge of designing and building various projects. None of this would have been possible without the invaluable support provided by the staff at Science Technical Services (STS) at the University of Waterloo. STS not only provided me with machining services to bring

my projects to life but also offered essential guidance on machining fundamentals. They were always available to discuss how I could enhance my mechanical designs to make them more feasible, machinable, and cost-effective. I want to extend my heartfelt thanks to the STS staff, including but not limited to Hiruy Haily and Harmen Vander Heide. Hiruy, in particular, has been not just a colleague but also a great friend. His exceptional machining skills often led him to come up with ingenious techniques for machining various designs that left me awestruck. Additionally, I would also like to express my gratitude to the faculty at QNC Nano Fab, who often went above and beyond their requirements to assist me with what I needed. Especially, I would like to thank Taso Alkiviades for his constant support. I would like to express my gratitude to the staff at the Institute for Quantum Computing (IQC), including but not limited to Roberto Romero, Chris Kleven and Steve Wiess, for their constant support and willingness to go above and beyond to assist us in various situations.

I am also incredibly grateful for the unwavering support of my friends at Waterloo who helped me through the challenging times of my PhD journey. I want to express my heartfelt thanks to Prathamesh, a long-term friend from undergrad, an amazing roommate, and a constant pillar of support during the difficult times of the pandemic lockdown. I also extend my gratitude to my wonderful roommates and officemates over the years of my PhD – Haibo, Dinakaran, Matt, Cristobal, Varsha, and Victor – who not only helped maintain a clean and harmonious living environment but also made the journey more enjoyable. I would like to express my appreciation to my landlord, Olexander Bykov, who is not only an outstanding individual but also the best landlord one could hope for. He promptly addressed any issues we had with the house, ensuring that I had a peaceful and comfortable place to live. I am also thankful for the consistent support, even from a distance, of my long-term undergraduate friends Shiva, Mihir, and Utkarsh. I would also like to extend my gratitude to my friends and fellow animal rights activists, including Mo Markham, Uday, David, Andrew, Kirsten, Jen, and many more from various organizations. Working alongside them has not only been fulfilling but has also provided a meaningful sense of purpose in my life. I'm especially grateful to Mo and her cats for providing a sense of family here at Waterloo while I've been living far from home.

I am also grateful to all the essential workers who have worked tirelessly during the COVID-19 pandemic to help control the spread of cases.

I feel lucky and fortunate for the boundless love and support received from Vipula. Saying thanks would be something less, I feel privileged from the support I got from my parents Chennaiah and Laxmi, my sister Himabindu, whose blessings I always had.

Dedication

This thesis is dedicated to the efforts of generations of physicists.

Table of Contents

List of Figures

Chapter 1

Introduction

The study of complex interacting spin systems is currently a prominent topic in physics, with applications spanning from quantum magnetism [4] and understanding superconductivity [39] to gaining insights into high-energy physics [22, 5]. However, these systems are too complex and intricate to be effectively studied using classical computers alone. A quantum simulator is essential to explore the rich phenomena associated with them [9, 30].

For instance, solving for the ground state of arbitrary fully connected spin-1/2 systems using exact diagonalization (without any approximate methods) on a classical computer necessitates exponentially scaling memory requirements. To illustrate, the memory needed can reach up to 9000 Terabytes for 25 spins and a staggering 40,000,000 Terabytes for 36 spins (estimated naively). Consequently, the solution to such arbitrary problems demands the utilization of a quantum simulator.

A quantum simulator serves as a highly controllable test bed that can emulate the interactions of an uncontrollable quantum system [9, 30]. It involves several steps, including state preparation, evolution under simulated set of operations, and subsequent state measurements [9]. These steps are essential for effectively simulating the dynamics and properties of the target quantum systems within a simulator.

Quantum simulators can be broadly categorized into two main types (Figure 1.1): analog quantum simulators and digital quantum simulators [9]. Analog quantum simulators aim to replicate the dynamics of quantum systems by directly mapping the interactions and properties of the simulated system onto the simulator itself. On the other hand, digital quantum simulators utilize universal quantum computers to simulate quantum systems using a sequence of universal quantum gates and algorithms. In contrast, hybrid analog-digital quantum simulators, which have been proposed in recent years [84], simulate a

temporal series of native Hamiltonians to achieve the desired target dynamics.

To better understand the differences between these two approaches of quantum simulators, let us draw an analogy to solving problems in aerodynamics [20]. When studying the aerodynamics of a car or an aircraft, there are two primary methods that can be employed. One approach is to use a physical wind tunnel with a real test piece or a scaled-down model to directly observe and analyze the aerodynamic behavior of the system of interest. This corresponds to the analog quantum simulator in our analogy.

Alternatively, one can mathematically model the system using equations such as the Navier-Stokes equations and numerically solve them on a classical (digital) computer. This computational approach allows for the simulation of the system's aerodynamics, although with the limitations and approximations inherent in the numerical methods employed. This aligns with the digital quantum simulator in our analogy. Thus, the wind tunnel testing represents the analog quantum simulator, where the physical system is directly mapped onto the simulator, while using a computer to solve the equations corresponds to the digital quantum simulator, which relies on computational methods to simulate the quantum system.

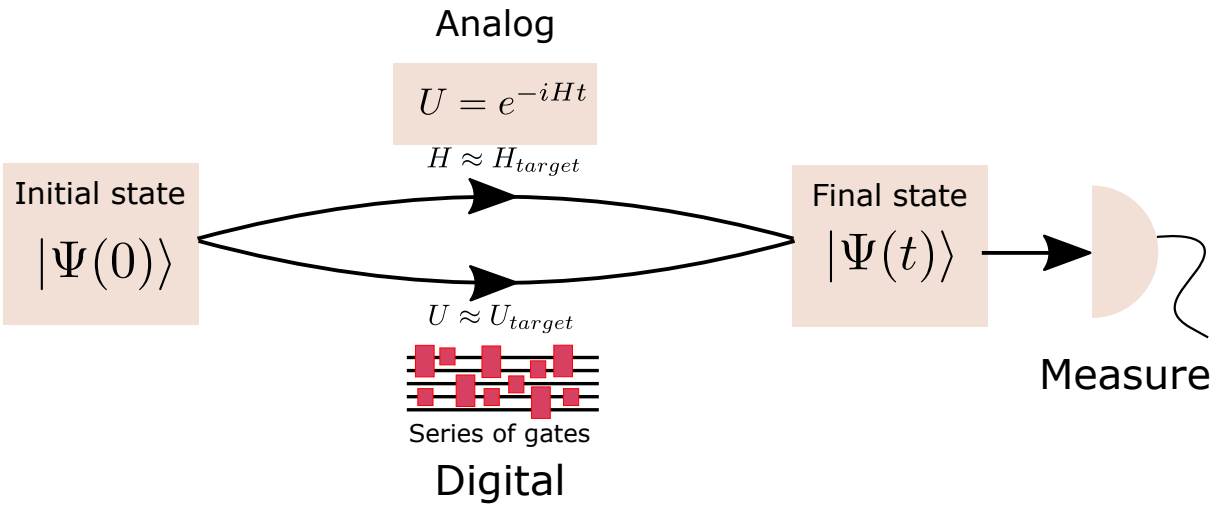

Figure 1.1: **Different Kinds of Quantum Simulators:** A quantum simulator is initialized to an initial state $|\Psi(0)\rangle$ and subjected to evolution under simulated Hamiltonian (for analog quantum simulation) or set of single qubit and two qubit gates (for Digital quantum simulation) emulating the target unitary. This is followed by the measurement of the final state $|\Psi(t)\rangle$.

Both analog and digital quantum simulators have distinct advantages and limitations. Analog quantum simulators are constrained in the types of problems they can effectively study, as they are typically limited to a selective set of native Hamiltonians. Additionally, they are susceptible to errors caused by decoherence and calibration. However, the decoherence resulting from the external environment can be estimated, bounded, and corrected for in the models. When the decoherence is controlled, it has been established, especially for local models, that the accuracy of quantum simulations is determined by the quality of calibration [30, 20, 83].

On the other hand, digital quantum simulators have the potential to tackle a wider range of problems. However, this comes at the cost of requiring a significant number of two-qubit and single-qubit gates, which can introduce errors during the digitization process, such as Trotterization [20]. Furthermore, the physical realization of fault-tolerant, error-corrected quantum systems is still not a reality.

While some experimental implementations of quantum computers have claimed to demonstrate quantum supremacy [31, 2, 110], these achievements have primarily been for highly tailored problems optimized to showcase quantum advantage [20]. The notion of achieving quantum advantage has been discussed for a considerable period of time. In the current era of NISQ (Noisy Intermediate-Scale Quantum) computers, where practical error-corrected quantum computing is not yet feasible, analog quantum simulators have the potential to surpass classical computers in terms of accuracy. These simulators can actually be built with current technologies to achieve quantum advantage during this transitional phase, offering improved performance compared to classical computers [20].

Figure 1.2 displays an estimation from Ref. [20], comparing the dynamics of a 1D Hubbard model on a lattice of size 20. The model's dynamics are governed by the Hamiltonian:

$$\hat{H} = -J\sum_{\langle i,j\rangle,\sigma} \hat{c}^{\dagger}_{j\sigma}\hat{c}_{i\sigma} + U\sum_{i} \hat{n}_{i\uparrow}\hat{n}_{i\downarrow} \tag{1.1}$$

This model represents the electrons with two spin components located in one orbital of each site. The first term in Eq.1.1 represents the tunneling of electrons between neighboring sites while the second term represents the electron-electron interactions. Figure 1.2 illustrates the estimation of errors in estimating two-particle correlation functions using classical, analog, and digital quantum simulators. Here, the particle dynamics are calculated when the system properties undergo sudden changes, such as in quench experiments. In the case of classical computer simulations, the errors grow exponentially due to truncation in the size of the matrix product state. Analog quantum simulation is limited by calibration errors, which are assumed to be around 1%. The errors in fault-tolerant digital simulations grow at a slower rate, mostly due to digitization. However, as the system size increases,

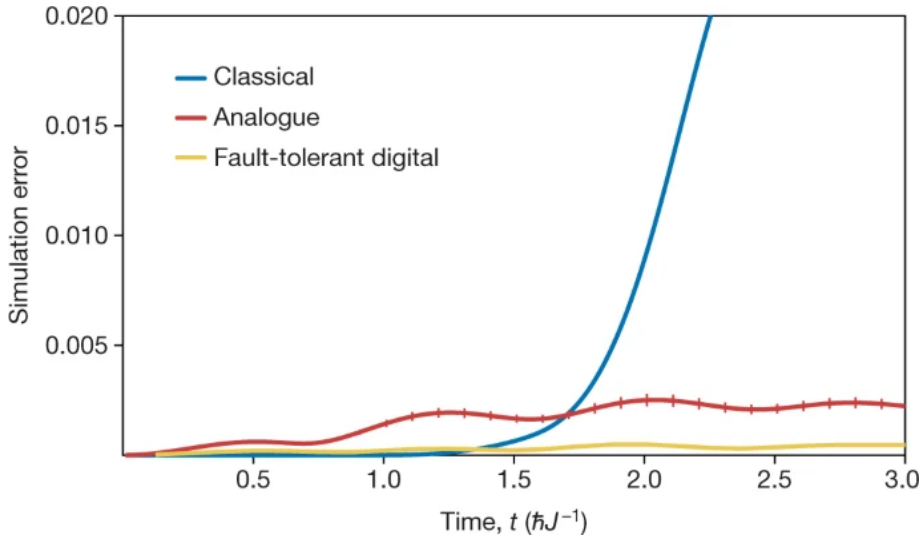

Figure 1.2: **Scaling of Simulation Errors:** Shows the error in simulating the target dynamics using classical, Analog and Digital quantum simulations. The results are taken from Ref. [20].

such as to 100 particles (a 2D lattice of 10x10), the requirements of a digital quantum simulator grow rapidly, necessitating over a million gates. On the other hand, performing analog quantum simulation with 100 particles is achievable with current technology [78].

In summary, based on the example mentioned above, while digital quantum simulators have fewer errors, current technology cannot yet meet the requirements of implementing large number of gates. In contrast, analog quantum simulators of near-term achievable sizes have a scope to demonstrate quantum advantage [20]. But this does not imply that we should cease our efforts in developing digital quantum simulators. Instead, we must continue working on various aspects that currently hinder us from achieving a realizable error-corrected logical qubit.

Based on the insights discussed, I believe the following heuristics should be prioritized for current quantum simulators to demonstrate real practical quantum advantage in addition to the goals of increasing the system size and controllability:

1. Build quantum simulators with **minimal external decoherence** for analog quantum simulations.

2. **Expand the toolkit of models** that can be effectively simulated using analog quantum simulations.

3. Maximize the efficacy of **calibrations** by enhancing system stability and implementing robust systems engineering practices.

4. Push the boundaries of **error correction** to advance towards fault-tolerant digital quantum simulation.

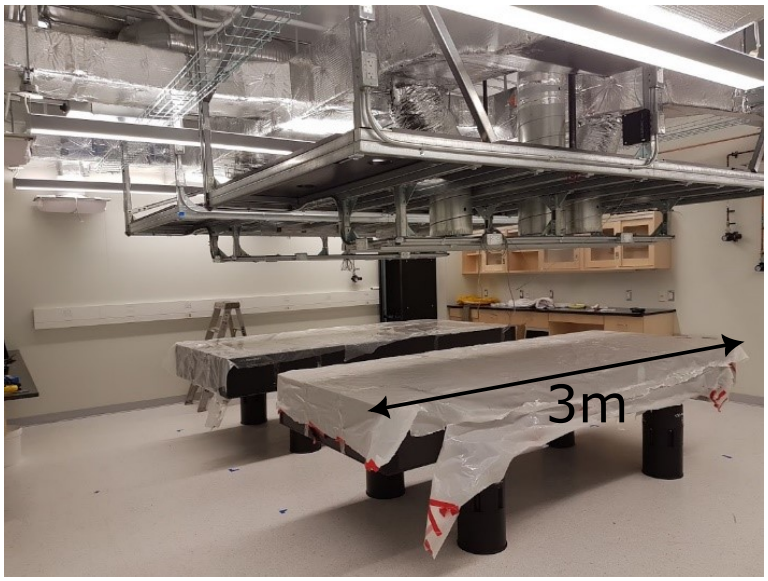

Figure 1.3: **Empty Lab with Optical Tables:** Shows the picture of our lab (QNC B221B) in the early stages of my PhD in June 2019.

Experimentally achieving calibration errors of <1% for larger systems, requires stability and continuous feedback in various experimental components. Designing experiments from scratch while considering systems engineering principles is necessary in order to meet these requirements. This involves in detailed planning on how to design, integrate, and manage complex systems over their life cycles. By focusing on these heuristics, we can make substantial progress in developing quantum simulators that demonstrate tangible practical quantum advantage.

With the insights gained from the discussions above, as an experimentalists starting from an empty lab (Figure 1.3), our goal is to strategically establish a roadmap for building

quantum systems capable of studying problems that are computationally intractable for classical computers.

1.1 Trapped ions as quantum simulators

There are several platforms that are considered as candidates for quantum simulators, including atomic quantum systems [10, 32, 68, 9], superconducting systems [41, 35], and photonic-based systems [3, 34]. Atomic quantum systems, such as laser-cooled trapped ions, are excellent candidates [68, 9] for quantum simulators due to their many excellent properties. These properties include long coherence times exceeding one hour for single qubits [108], ease of state preparation and isolation, and controllable long-range spin interactions with all-to-all couplings.

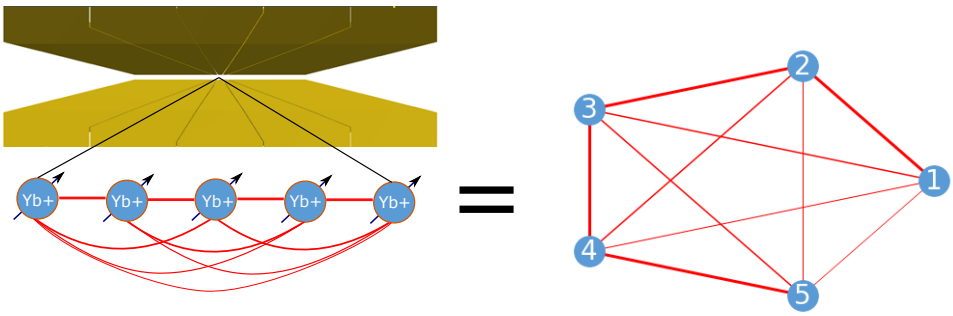

Figure 1.4: **Ion Trap Equivalence:** A chain of 5 $^{171}Yb^{+}$ ions in an ion trap demonstrates equivalence to a fully connected graph, with the edges symbolizing the spin-spin interactions.

Despite trapped ions typically being arranged in a chain-like structure, the system effectively behaves as if it were fully connected. This behavior arises from the interconnectedness of the ions (Figure 1.4), facilitated by the spin-spin interaction mediated through the common phonon bus. In the subsequent chapters (Chapters 2,3), I will delve into the details of how a chain of ions levitated in ultra-high vacuum can serve as a quantum simulator.

With the interactions mediated through phonons, the widely used Mølmer-Sørensen interaction scheme [67] in trapped ions allows for performing analog quantum simulations. In this scheme, the effective Ising Hamiltonian is given by:

$$H_{eff} = H_{XX} = \sum_{i,j} J_{i,j} \sigma_i^x \sigma_j^x \tag{1.2}$$

The Ising interaction Hamiltonian mentioned above, has been utilized in the study of various rich phenomena using trapped ions as programmable systems [68]. These studies encompass a wide range of topics, including adiabatic quantum simulations in effective spin models [27, 91], many-body localization [99, 12] and prethermalization [73], dynamical phase transitions in quantum magnetic systems [48, 109], and variational quantum algorithms [112, 37].

However, it is worth noting that most of the problems studied using trapped ions have been restricted to unitary Ising-type interactions or their extensions, such as utilizing fermionic Hamiltonians through transformations like Wigner transformations [22]. This restriction in the available toolkit of Hamiltonians has limited the scope of problems that can be addressed using trapped ions as quantum simulators. One of the techniques that immediately expands the kinds of simulation toolkit in trapped ions is the site-selective mid-circuit measurements and reset. This enables the study of new classes of quantum simulations such as measurement-based phase transitions [76, 19, 58, 98, 14, 89, 55] and reservoir engineering with controlled dissipation [66, 33, 105]. Furthermore, mid-circuit measurements are crucial [52, 87, 94], and they represent one of the limiting factors in achieving error-correction in trapped ions. With this motivation in mind, Chapter 4 of my thesis delves into the intricacies of implementing mid-circuit measurements and resets. Within this chapter, I explore the challenges arising in the process of achieving mid-circuit measurements and attain state-of-the-art fidelities in those processes in our simulator.

As discussed in the first paragraph, one of the hardest problems to solve on a classical computer is exact diagonalization, especially when it comes to finding the ground state of an arbitrary system without any symmetries or using approximate methods. However, analog quantum simulation offers a potential solution by utilizing adiabatic quantum simulation [49, 85, 45, 46] to find the ground state of a Hamiltonian. In this approach, the system is initially prepared in the ground state of a simple Hamiltonian that can be easily prepared. Then, the system is gradually transitioned or ramped to the target system's Hamiltonian. By ensuring that this process is done slowly enough [68] (according to the adiabatic theorem), the final state of the system will be the ground state of the target system.

However, adiabatic quantum simulation has limitations in terms of the types of Hamiltonians that can be effectively solved, and the speed of ramping the Hamiltonian can get

rapidly slow as the system size increases [21, 69]. To overcome these limitations, an alternative approach is to employ reservoir engineering with controlled dissipation to prepare a subsystem to its ground state [66, 33]. By leveraging the site-selective mid-circuit resets [71] mentioned earlier, I have successfully demonstrated a proof of principle experiment for lowering the energy of a subsystem using analog quantum simulation driven by dissipation on a reservoir. The preliminary results of this research are presented in Chapter 5 of my thesis, with additional details on the crucial task of calibrating the system's native Hamiltonian in analog quantum simulations.

Thus, through the work presented in Chapters 4 and 5, I address goals 2 and 4, as outlined earlier.

1.1.1 Building a trapped ion quantum simulator

Now, let us comprehend the requirements for constructing a quantum simulator based on the aforementioned heuristics. Usually, a Paul trap is employed to trap the chain of ions within an ultra-high vacuum chamber, which maximizes the lifetime of ions and minimizes decoherence errors resulting from background gas collisions. The optical and electronic systems responsible for controlling the ions are positioned outside the vacuum chamber, where they interact with the ions.

The process of constructing the entire apparatus from scratch necessitates the optimization of various parameters to achieve the aforementioned objectives. These parameters encompass a range of aspects, including trap geometry, the design of the vacuum apparatus, high-fidelity detection, addressing optics, electronic control systems, and more. A few significant considerations are presented as a mind map in Figure 1.5.

While it is indeed important to construct a system from the ground up and optimize each step along the way, dedicating excessive time to improving the initial building process could hinder optimization efforts in later stages. This would result in a prolonged period before meaningful optimizations can be undertaken in every stage.

Figure 1.5: **Quantum Simulation Mind Map:** This diagram illustrates the consideration of various parameters when constructing a trapped ion quantum simulator.

In particular, the vacuum chamber and its internals are required to trap the ions, and the ions are necessary to optimize parameters outside the vacuum chamber (Vacuum externals in Figure 1.5). However, it is crucial not to rush the construction of the vacuum

chamber with all its internals (Vacuum internals in Figure 1.5) without fulfilling our heuristic goals. Notably, the process of building and assembling the vacuum chamber and its internals often takes a considerable amount of time, and once completed, it is typically not opened during the lifetime of an experimental apparatus ($\approx$ 10 years) unless necessary due to an accident or maintenance.

To address these challenges, we have adopted a strategy of constructing two trapped-ion quantum simulators. The first system, called the four-rod trap, is primarily designed based on an existing and proven architecture. We managed to build the entire vacuum system in approximately six months, while also optimizing certain technologies along the way, such as developing new recipes for building the trap electrodes [51]. Once this system was constructed, we began optimizing and designing various techniques, including site-selective mid-circuit measurements and resets, new classes of quantum simulations with dissipation. Simultaneously, we are constructing a second system called the blade-trap, employing careful optimizations of parameters such as ultra-high vacuum, trap geometries, and stable referencing.

Thus, the heuristic goals of building a quantum simulator are divided into parallel efforts. The four-rod trap system is focused on achieving goals 2 and 4, which involve expanding the quantum simulation toolkit and pushing the boundaries of error correction. This system serves as a platform for exploring new techniques and methodologies in quantum simulation. On the other hand, the blade trap system adopts a systems engineering approach and is optimized to meet goals 1 and 3 in the initial stages followed by the goals 2,4. Goal 1 entails minimizing external decoherence to ensure the system remains isolated from external disturbances that can introduce errors. Goal 3 involves increasing the system's stability, which enhances the effectiveness of calibrations and overall performance. By splitting the goals and strategies between the two systems, we can pursue parallel advancements and address specific objectives in each system, thereby maximizing the overall progress towards building an efficient and robust quantum simulator.

1.2 Guide to the thesis

The following is a guide to the structure and content of the thesis:

- **Chapter 2:**
  This chapter provides an overview of the theoretical foundations necessary for understanding the operation of a trapped ion quantum simulator. It covers topics such as

ionization, trapping, cooling, state preparation, and measurement techniques. Additionally, coherent operations performed in this system using Raman transitions are briefly described.

- **Chapter 3:**
  Chapter 3 presents a comprehensive description of the experimental architecture of the four-rod trap quantum simulator. This section outlines the construction and setup of the experimental system, which has been developed collaboratively with colleagues throughout the course of my PhD. The experimental setup detailed in this chapter serves as the basis for the experiments presented in Chapters 4 and 5.

- **Chapter 4:**
  This chapter focuses on the challenges associated with implementing mid-circuit measurements and resets in the trapped ion quantum simulator. It discusses the mitigation strategies employed, as well as the methods used for characterizing and benchmarking the achieved fidelities in these incoherent processes.

- **Chapter 5:**
  This chapter outlines an analog quantum simulation approach employed to cool the spin sub-system close to the ground state of the guiding Hamiltonian. This scheme leverages the mid-circuit reset capabilities described in Chapter 4. The chapter provides a detailed account of the preliminary simulations and the results obtained.

- **Chapter 6:**
  This chapter documents the parallel efforts in building a next-generation large-scale trapped ion quantum simulator. The chapter delves into the design, fabrication, and testing of each component of the system, highlighting their alignment with the main goals of the project. Notably, the chapter showcases the achievement of base pressures below 9×10^{-13} mbar in the vacuum chamber.

- **Chapter 7:**
  The final chapter concludes the thesis and presents an outlook on future experiments and potential research directions. It provides a summary of the findings, their implications, and suggests areas for further exploration and development.

Chapter 2

Basics of a trapped ion quantum simulator

In this chapter I present some of the basic tools to understand the working of a trapped ion quantum simulator. Other theoretical tools needed specifically to understand the later chapters are described in them when needed. The derivations of various mathematic forms presented in this chapter are well described in other numerous references and thesis.

2.1 Overview

Trapping charged particles using Radio Frequency (RF) traps was first proposed by Wolfgang Paul in the 1950s, hence the name "Paul traps" [80]. Since then, ion traps have found wide-ranging applications, from mass spectrometers to trapped ion quantum computers and simulators.

A Paul trap operates by combining oscillating and static potentials to create an effective pseudo-potential that confines the charged particles or ions [80]. In our work, we specifically focus on ytterbium ions ($^{171}Yb^{+}$). These ions are created by subjecting neutral ytterbium atoms to a two-step ionization process. Once trapped, the ions are cooled using techniques such as Doppler cooling, which causes them to crystallize into equilibrium positions, often forming a chain based on the relative strengths of the trapping forces in different directions.

We assign the ground state hyperfine levels of $^{171}Yb^{+}$ ions as the basis states $|\downarrow_z\rangle$ and $|\uparrow_z\rangle$ of a spin-1/2 particle, representing qubits [77]. The state of the qubits can be inferred by measuring the state-dependent fluorescence when 369 nm light resonant with the

$^2S_{1/2}\,|F=1\rangle \rightarrow {}^2P_{1/2}\,|F=0\rangle$ (denoted as $D_1^{(10)}$) transition is applied and detected [77]. To reset the ions, we use resonant light to drive the $^2S_{1/2}\,|F=1\rangle \rightarrow {}^2P_{1/2}\,|F=1\rangle$(denoted as $D_1^{(11)}$) transition, optically pumping the ion to the $|\downarrow_z\rangle$ state [77]. Coherent operations on the ions are performed using pairs of far-detuned Raman beams at a wavelength of 355 nm. When the beatnote frequency of the Raman beams matches the frequency difference between the qubit levels (hyperfine splitting), the Raman beams effectively drive Rabi oscillations. The interactions between the ions are mediated through the collective motional modes of the ion chain [67]. By off-resonantly exciting and de-exciting the phonons in the chain, a pair of Raman beams can create entangling operations, generating an effective spin interaction Hamiltonian. Further details on the manipulation of the ions are presented in this chapter and the experimental techniques employed are presented in the subsequent chapters of the thesis.

2.2 Basics of an RF Paul trap

Due to the limitations imposed by Earnshaw's theorem [24], it is not possible to trap a charged particle solely using static electric fields. As a consequence, a trapping potential generated by a static electric field in one direction would result in an anti-trapping potential in another direction, resembling a saddle shape. To overcome this challenge, RF Paul traps [80] utilize oscillating electric fields to confine ions in space. Various implementations of Paul traps exist, accommodating ions in different shapes and geometries. The focus of this thesis revolves around a specific trap geometry known as a linear RF Paul trap, particularly a four-rod trap (refer to Fig. 2.1). This linear Paul trap generates a two-dimensional (radial) confining potential by employing oscillating potential through quadrupole electrodes. On the other hand, confinement in the axial direction is achieved using endcaps that generate a static field, resulting in a harmonic trapping potential. This particular geometry is employed to trap a linear chain of ions oriented along the axial direction.

In the given geometry, the quadrupole electrodes shown in Fig. 2.1 are subjected to oscillating voltages with an amplitude of V_0 and a frequency of Ω_{RF}. Specifically, the diagonal pair of electrodes are driven in phase, while the pair in the anti-diagonal is driven 180 degrees out of phase.

This voltage configuration approximately generates a potential in the radial plane, represented by the equation:

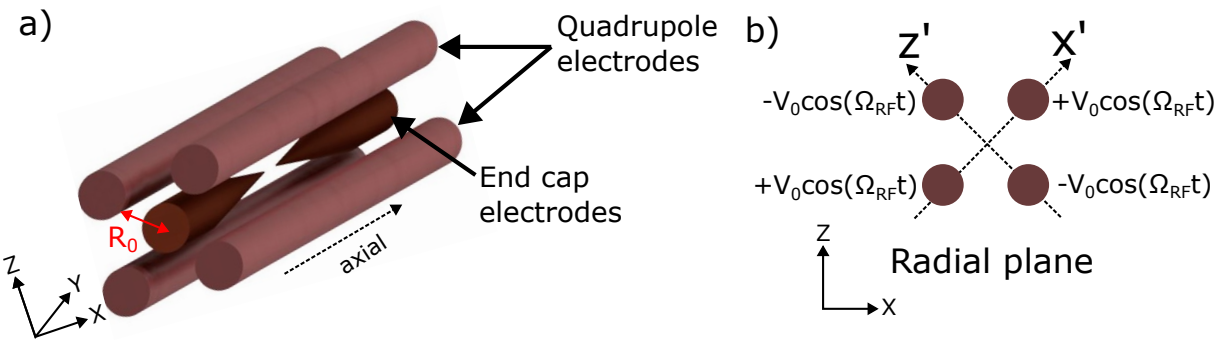

Figure 2.1: **Four-Rod Trap Geometry:** a) The trap consists of four parallel quadrupole electrodes and two end-cap electrodes aligned along the axial (Y) direction. b) Cross-section of the trap geometry along the radial (XZ) plane, showing the voltage configuration.

$$\Phi_r = \eta \frac{V_0}{R_0^2} \cos(\Omega_{RF} t)((X')^2 - (Z')^2) \tag{2.1}$$

Here, Φ_r represents the potential in the radial direction, R_0 signifies the distance between the symmetry axis of the quadrupole electrode surface, and η is the geometric fudge factor that arises from deviations in the trap's geometry, which diverge from the ideal hyperbolic electrode geometry

The equations of motion describing the motion of a charged particle (ion) in the radial plane, utilizing the above oscillating potential, can be represented by the Mathieu equations in the following form:

$$\ddot{r} + 2q\cos(2\tau)r = 0 \tag{2.2}$$

Here r represents the co-ordinate in the radial plane, $q = \frac{2\eta e V_0}{m\Omega_{RF}^2 R_0^2}$, $\tau = \Omega_{RF} t/2$, m is the mass of the particle and e is the charge of the particle. The parameter q, known as the Mathieu parameter, plays a significant role in determining whether the ion's trajectory in the trap is bounded or unbounded. In typical experimental conditions, the regime of operation maintains $q \ll 1$, approximately 0.1, ensuring that the trajectory of the ion remains bounded. Under the approximation of $q \ll 1$, we can solve the equations of motion and find that the radial position of the particle is given by the following form:

$$r(t) = A\cos(\omega_r t + \phi_r)(1 - \frac{q}{2}\cos(\Omega_{RF} t)) \tag{2.3}$$

Here, the term $\omega_r = \frac{\sqrt{2}\eta e V_0}{m\Omega_{RF} R_0^2}$ is commonly referred to as the secular frequency, also known as

the radial trap frequency. Meanwhile, the variables A and ϕ_r correspond to the amplitude and phase of the ion's motion, respectively.

By examining the above equation, we can observe that the motion of the ion is primarily governed by the secular frequency, which is a significant component of the ion's trajectory in the radial plane. However, there exists an additional component known as "micromotion." This micromotion exhibits a small amplitude oscillation.

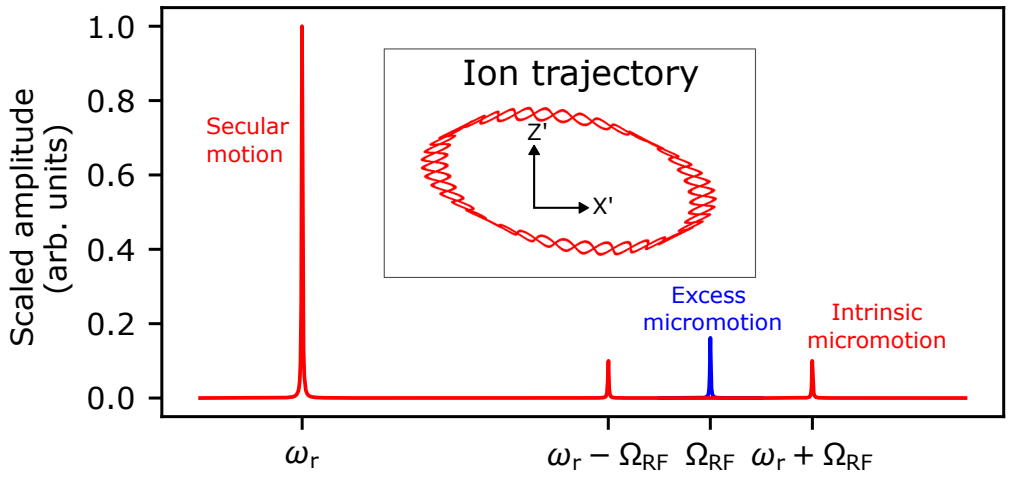

Figure 2.2: **Trajectory and Frequency Spectrum of Ion Motion in an RF Paul Trap:** The inset illustrates the simulated ion trajectory within the XZ plane. The main plot displays the spectrum of the ion's motion, emphasizing the contributions of secular, intrinsic, and excess micromotion.

The trajectory of the ion calculated using Eq. 2.3 in above potential is illustrated in the inset of Fig. 2.2. Furthermore, Fig. 2.2 displays the frequency spectrum of the trajectory in the inset (red trace), which is primarily influenced by the secular frequency. This frequency is distinct from the intrinsic micromotion and is separated in frequency space. The motion of the ion can be approximated as a harmonic oscillator with angular frequency ω_r when observed over timescales on the order of multiples of $2\pi/\Omega_{RF}$. However, this trajectory is only valid when the ion is positioned near the center of the RF null line, which is the symmetry axis where the potential resulting from the quadrupole vanishes. If an external field displaces the ion from this position, additional motional components at the frequency Ω_{RF} emerge. These additional components are referred to as "excess

micromotion" and can be visualized as the blue trace in Fig. 2.2. This additional external field could arise from the imperfections in the orientation of the quadrupole electrodes or the presence of additional static potential from other electrodes, such as the end caps. This excess micromotion leads to unwanted effects including heating of ions and decrease in lifetime of ions. Consequently, it becomes necessary to minimize and compensate for this unwanted electric field causing the excess micromotion [8]. Typically, this issue is addressed through the utilization of additional compensating electrodes. These electrodes are designed to counteract the influence of external stray static fields and guide the ion towards the RF null, where the excess micromotion is minimized. By effectively canceling out these external fields, the compensating electrodes help ensure that the ion remains in proximity to the RF null and experiences reduced levels of excess micromotion. More experimental details of the trap and the excess micromotion minimization are presented in Chapter 3.

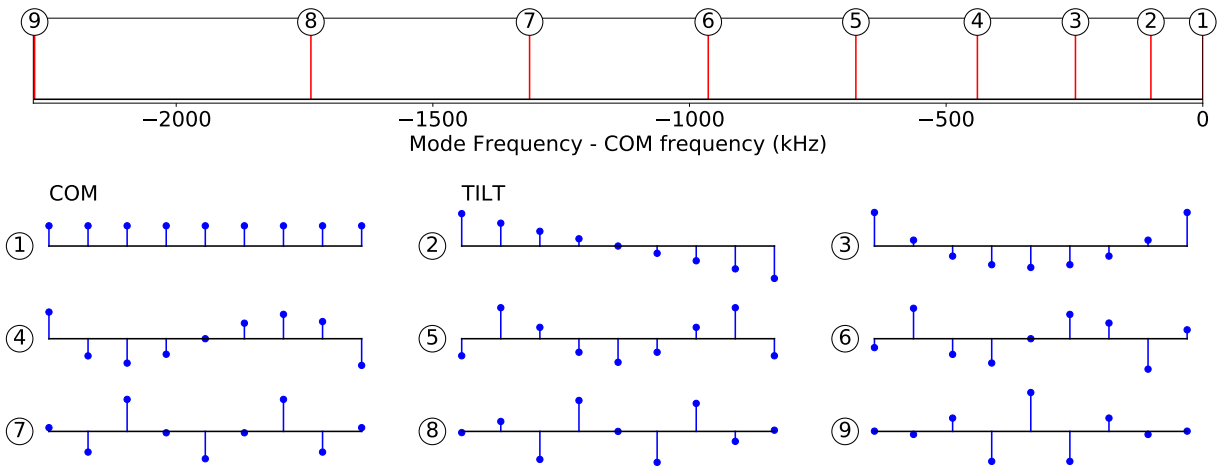

Figure 2.3: **Normal Modes of Oscillation in a Chain of Nine Trapped Ions:** The frequencies of normal modes along the radial (X' or Z') direction for a chain of N=9 ions are displayed at the top. In this context, the ions are confined within a potential with a radial trap frequency of $\omega_{X'} \approx \omega_{Z'} = 2\pi \times 5$ MHz and an axial trap frequency of $\omega_{\mathrm{Y}} = 2\pi \times 1$ MHz. The amplitudes of oscillation for each ion in a specific normal mode are depicted using blue ball-and-stick figures at the bottom.

With the effective harmonic potential created by the Paul trap in the radial direction, the confinement in the axial direction is created by the harmonic potential from the end-cap electrodes of trapping frequency ω_{Y}. In this configuration, the radial trapping frequency

$\omega_{X'} \approx \omega_{Z'}$ is typically much larger than the axial trapping frequency ω_Y. As a result, when the ions are cooled, they form a chain aligned along the axial direction due to the dominant radial confinement. The equilibrium positions of ions in a chain are determined by the combined effect of the confining potential generated by the electrodes and the Coulomb repulsion between the ions. At equilibrium, the chain of ions behaves as a system of coupled harmonic oscillators, exhibiting various normal modes of oscillation in all directions. Figure 2.3 [70] illustrates the normal modes along the radial direction for a chain of nine ions trapped in a potential with a radial trap frequency of $\omega_{X'} \approx \omega_{Z'} = 2\pi \times 5$ MHz and an axial trap frequency of $\omega_Y = 2\pi \times 1$ MHz. The radial center of mass (COM) mode where all the ions oscillate in phase has the highest frequency among all the modes in that direction. The subsequent normal mode is known as the tilt mode, characterized by ions at the ends of the chain exhibiting higher amplitudes of oscillation.

2.3 Ytterbium ions

With properties such as convenient hyperfine structure due to nuclear spin of $I = 1/2$, relatively simple closed-cycling transitions that can be excited using commercially achievable lasers, and being stable isotopes, $^{171}Yb^+$ ions emerge as excellent candidates for qubits. Figure 2.4 illustrates the complex energy level diagram of $^{171}Yb^+$ ions, highlighting significant transitions in red. The short-lived state (half life of ≈ 8 ns) $P_{1/2}$ is employed as the primary cycling transition, crucial for processes like Doppler cooling, state detection, and optical pumping. The transition between $S_{1/2}$ and $P_{1/2}$ levels possesses a natural linewidth of $\Gamma = 2\pi \times 19.6$ MHz and is driven by a quasi-monochromatic laser with a wavelength of 369 nm.

This transition is nearly closed, as ions excited to the $P_{1/2}$ level have a 99.5% probability of relaxing back to one of the levels in $S_{1/2}$. However, there exists a $< 0.5\%$ probability for the ions to decay to the $D_{3/2}$ state. To address this, a repump laser beam with a wavelength of 935 nm is employed to excite these ions in the $D_{3/2}$ state to the $[3/2]_{1/2}$ level which then decay and subsequently return to the $S_{1/2}$ state. The repump transition has a slightly narrower natural linewidth of $\Gamma = 2\pi \times 4.2$ MHz compared to the main cycling transition. Furthermore, when an ion is in the $D_{3/2}$ state, a collision with a background gas could transfer the state of the ion to the very long lived (half-life of 5.4 years) $F_{7/2}$ state. We use another repump beam of wavelength 760 nm to pump the ion back to the qubit manifold.

With the brief understanding of the energy level structure for $^{171}Yb^+$ ions, let us understand how the ions are generated.

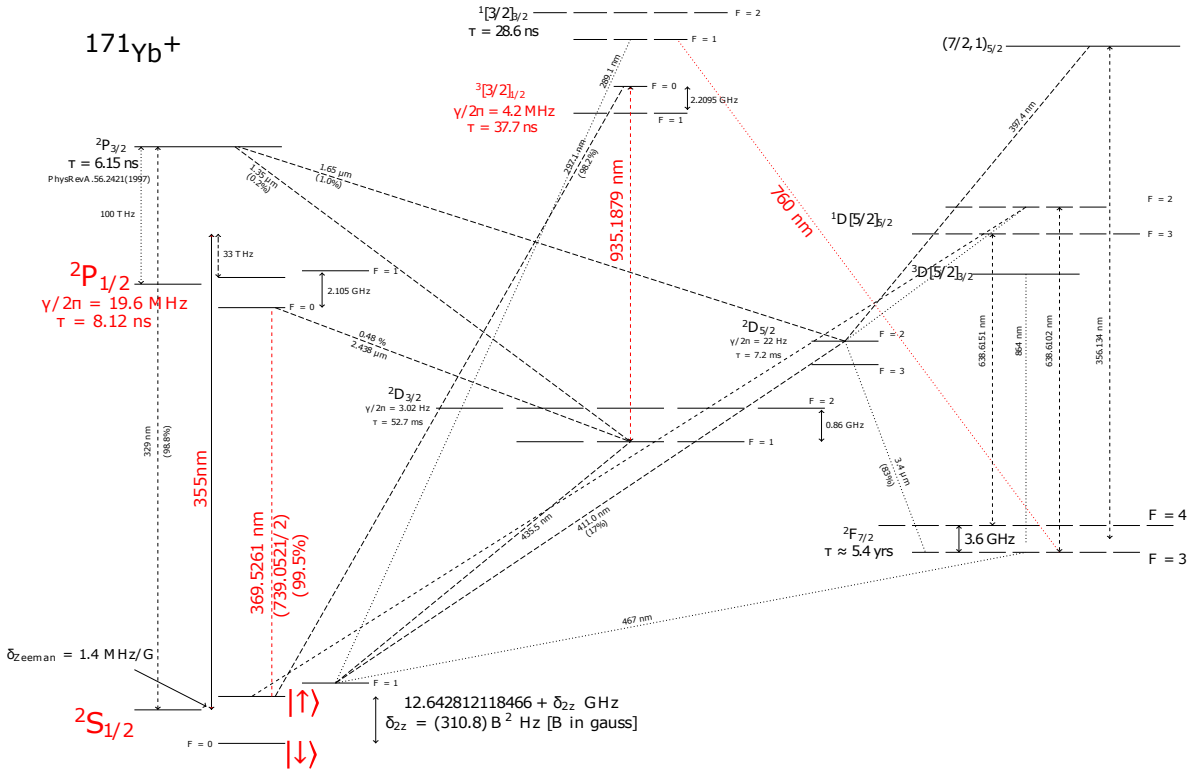

Figure 2.4: $^{171}Yb^{+}$ **Energy Level Diagram:** Complex energy level diagram of $^{171}Yb^{+}$ ions with relevant transitions highlighted [70].

2.3.1 Photoionization

$^{171}Yb^{+}$ ions are generated by photoionizing neutral Yb atoms within the trapping region. This photoionization process involves two steps. First, a neutral atom in the $^{1}S_0$ state is excited to the $^{1}P_1$ state using a 399 nm laser. Subsequently, the atom is ionized by further exciting the electron from the $^{1}P_1$ state to the continuum using either a 369 nm or 355 nm laser. The resonant transition in the first step has a frequency that varies for different isotopes of Yb, differing by hundreds of MHz [54]. This frequency difference allows for the selective excitation of only ^{171}Yb atoms. Further details on isotope selectivity are discussed in Chapter 6.

2.3.2 Doppler cooling

The cycling transition from $S_{1/2}$ to $P_{1/2}$ described above is utilized for Doppler cooling the ions. The Doppler cooling beam is detuned by approximately $\Gamma/2 \approx 2\pi \times 10$ MHz from the $S_{1/2}\,|F=1\rangle \rightarrow P_{1/2}\,|F=0\rangle$ transition. However, in order to cool the ions in all states, a sideband of 14.7 GHz is added to the light, allowing for Doppler cooling on the $S_{1/2}\,|F=0\rangle \rightarrow P_{1/2}\,|F=1\rangle$ transition with the same detuning of $\Gamma/2 \approx 2\pi \times 10$ MHz. Typically, the ions are Doppler cooled for a duration of 2.5 ms using a Doppler cooling beam with a power of approximately 20 μW. The beam has a beam waist($1/e^2$ radius) of 100 μm. While the saturation intensity of this transition being $I_{\text{sat}} = 51$ mW/cm^2 [26].

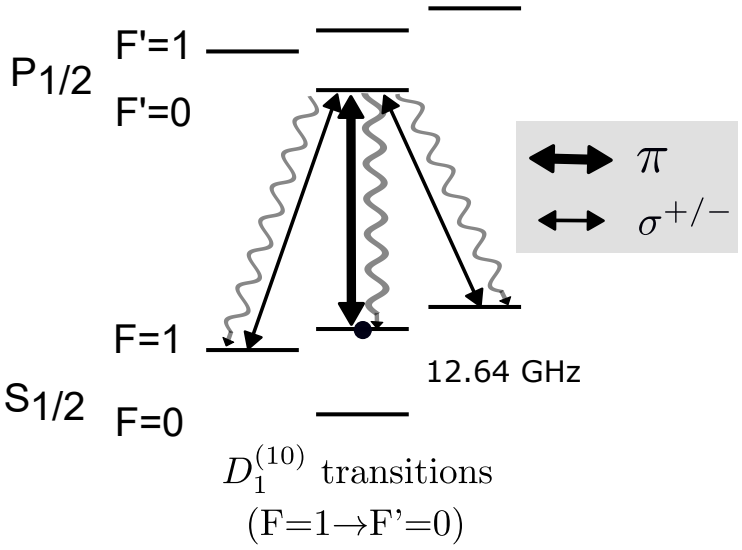

Figure 2.5: **State detection:** Schematic representation of the state detection process for $^{171}\text{Yb}^+$ ions. The ion is illuminated with light resonant to the $S_{1/2}\,|F=1\rangle \rightarrow P_{1/2}\,|F=0\rangle$ transition, labeled as $D_1^{(10)}$.

2.3.3 State detection

To determine whether the ion is in the $|\uparrow_z\rangle$ or $|\downarrow_z\rangle$, we measure the fluorescence emitted by the ion when it is illuminated with light resonant to the $S_{1/2}\,|F=1\rangle \rightarrow P_{1/2}\,|F=0\rangle$

transition,([77]). This transition is referred to as $D_1^{(10)}$, as shown in Fig.2.5.

If the ion is in the $|\uparrow_z\rangle$, it gets excited to the $P_{1/2}\,|F=0\rangle$ state and subsequently decays back to the $S_{1/2}\,|F=1\rangle$ state through spontaneous emission. However, it does not decay to the $|\downarrow_z\rangle$ because this transition is forbidden. The detector detects the light emitted during this spontaneous emission process to determine the state of the ion. On the other hand, if the ion is in the $|\downarrow_z\rangle$, it does not get excited by this light and therefore does not scatter any light. Consequently, the detector infers that the ion is in the $|\downarrow_z\rangle$ if it does not detect any light. It is the presence of this closed cycling transition that enables the state detection of $^{171}Yb^+$ ions. If the ion is initially in a superposition of $|\uparrow_z\rangle$ and $|\downarrow_z\rangle$, the first photon that the atom scatters upon detection probabilistically collapses the qubit state to either $|\uparrow_z\rangle$ or $|\downarrow_z\rangle$ due to the projective measurement. However, it is important to note that the cycle of excitation and spontaneous emission continues even after this initial measurement. The ion remains in the resulting state (either $|\uparrow_z\rangle$ or $|\downarrow_z\rangle$) and undergoes subsequent cycles of excitation and spontaneous emission. This process continues until the detector collects a sufficient number of photons to accurately determine the state of the ion.

It should be noted that the ion in the $|\uparrow_z\rangle$ could decay to levels other than the $|\uparrow_z\rangle$ in $S_{1/2}\,|F=1, m_F=\pm1\rangle$. However, if the illuminated light contains $\sigma^{\pm}$, the ion in $S_{1/2}\,|F=1, m_F=\pm1\rangle$ can be excited, and the detection process continues. Multiple cycles of excitation and deexcitation are required due to the limited collection efficiency of imaging systems. Typically, imaging systems have photon collection efficiencies on the order of a few percent. As a result, the ion may need to undergo hundreds of scattering cycles before its state can be inferred reliably.

In addition to the collection efficiency issue, background scattering and detector noise pose further challenges. The detector must receive a sufficiently strong signal to distinguish it from the background noise. Consequently, the detection time, which refers to the duration for which the detection light is illuminated on the ion, needs to be extended to accumulate an adequate signal above the noise level. Thus, the fidelity of accurately inferring the state of the ion increases with longer detection times. However, there is another process that competes with this and deteriorates the detection fidelity as the detection time increases. This process involves bright state pumping and dark state pumping.

Even though the detection light is far detuned (2.1 GHz) from the $S_{1/2}\,|F=1\rangle \rightarrow P_{1/2}\,|F=1\rangle$ transition, there is still a probability of off-resonantly exciting this transition. When this transition is excited, the ion can decay from the $|\uparrow_z\rangle$ to the $|\downarrow_z\rangle$ state. This mixing of states leads to a loss of information. Similarly, dark state pumping refers to the off-resonant pumping of the ion in the $|\downarrow_z\rangle$ to the $|\uparrow_z\rangle$. A more formal analysis of the state

detection fidelity as a function of detection time is discussed in Chapter 3 when addressing this issue in the context of mid-circuit measurements.

Another important aspect to consider in state detection is the polarization of the detection light. As mentioned earlier, for the cyclic scattering process to continue, the detection light should contain components of σ^+ and σ^-. However, it has been found that the optimal polarization for efficient state detection is the one that consists of equal portions of π, σ^+, and σ^- components [26].

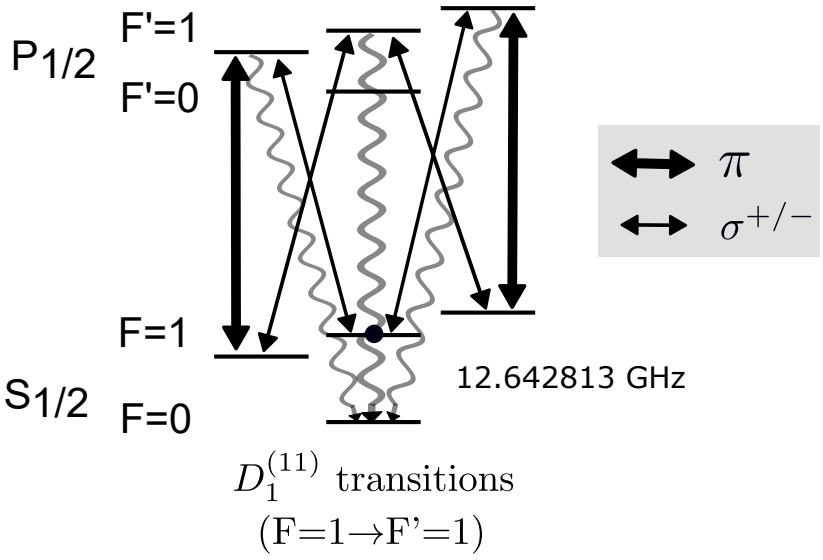

Figure 2.6: **Optical Pumping:** Schematic representation of the optical pumping process for $^{171}Yb^+$ ions. The ion is illuminated with light resonant to the $S_{1/2}\,|F=1\rangle \rightarrow P_{1/2}\,|F'=1\rangle$ transition, labeled as $D_1^{(11)}$.

2.3.4 State reset/optical pumping

The state-reset process involves incoherently resetting the ion to the $|\downarrow_z\rangle$ state. This is achieved by illuminating the ion with light that drives the $S_{1/2}\,|F=1\rangle \rightarrow P_{1/2}\,|F=1\rangle$ transition, also known as the $D_1^{(11)}$ transition. When the ion is in the $|\downarrow_z\rangle$, this light does

not excite the ion. However, if the ion is in the $|\uparrow_z\rangle$, it gets excited to the $P_{1/2}|F=1\rangle$ state, which can either decay back to the $S_{1/2}|F=1\rangle$ state or directly to the $|\downarrow_z\rangle$. By repeating this process, the ion eventually accumulates in the $|\downarrow_z\rangle$.

Similar to the state measurement described earlier, the first photon scattered by the atom during the reset process performs a projective measurement on the ion. To ensure efficient pumping of the ion to the $|\downarrow_z\rangle$, light with various polarizations is required, as the ion can also end up in $S_{1/2}|F=1, m_F=\pm 1\rangle$ states. Consequently, multiple excitations are needed to ensure that the ion accumulates in the $|\downarrow_z\rangle$, as direct decay from the $|\uparrow_z\rangle$ to the $|\downarrow_z\rangle$ with unit probability is not guaranteed.

The probability of the ion being reset to the $|\downarrow_z\rangle$ increases exponentially as the duration of illumination with the optical pump beam increases. Consequently, the probability of the ion, initially in the $|\uparrow_z\rangle$, being in the $|\uparrow_z\rangle$ state as a function of pumping time can be fitted with an exponential decay curve. This curve can then be used to determine the time required for the ion to be reset to the $|\downarrow_z\rangle$ with a high probability, such as 99.9%.

It is important to note that the characteristic of this exponential decay curve depends on the power and polarization of the optical pumping light. Therefore, by analyzing the decay curve, it is possible to estimate the power and polarization of the input light. Further details regarding this estimation process can be found in Chapter 3. In our experiment, the time required for the reset process typically ranges between 1-10 µs, depending on the power and polarization of the pumping light. Furthermore, the pumping process serves as a mechanism to introduce incoherent dissipation to the ion chain, as discussed in Chapters 3 and 4.

2.4 Coherent operations

The coherent operations of the ion spins in our system utilize stimulated Raman transitions in the $^{171}Yb^{+}$ ion chain. For driving these transitions, we employ a 355 nm laser. We have two beams of the 355 nm laser, labeled as Raman1 and Raman2, with frequencies ω_1 and ω_2, respectively. The Rabi frequencies for these beams are denoted as Ω_1 and Ω_2. These laser beams are directed onto the ion at a 90-degree angle to each other.

The frequency difference between the Raman beams, $\Delta\omega$, is chosen to be close to the qubit transition from the $|\downarrow_z\rangle$ state to the $|\uparrow_z\rangle$ state. By applying these laser beams, we couple the $|\downarrow_z\rangle$ and $|\uparrow_z\rangle$ states to the $P_{1/2}$ states, using a large detuning of $\Delta = 33$THz. This large detuning allows us to simplify the three-level dynamics to a two-level system by adiabatically eliminating the excited states of $P_{1/2}$. Consequently, we can treat the effect

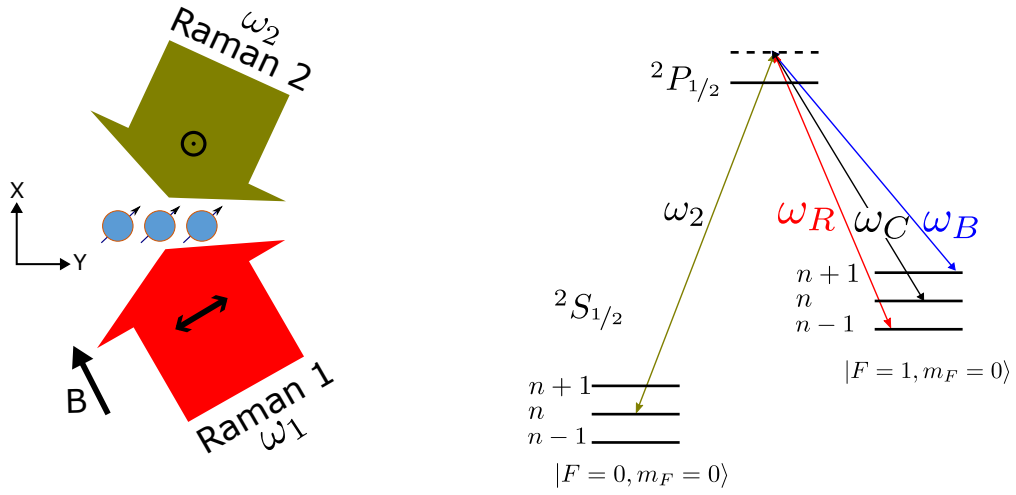

Figure 2.7: **Carrier, Red Sideband, and Blue Sideband Transitions:** The left figure shows the orientation of the Raman lasers with respect to the chain of ions. The polarization of each beam and the magnetic field is also shown. The right figure illustrates the energy level diagram and the frequencies of Raman lasers driving carrier, red sideband, and blue sideband transitions.

of the pair of Raman beams with a beat-note frequency $\Delta\omega$ as a single laser driving the two levels from the $|\downarrow_z\rangle$ to the $|\uparrow_z\rangle$.

With this approximation, we can express the Hamiltonian describing the interaction between the ion and the laser, after applying the rotating wave approximation, as follows [44, 68, 6]:

$$H = \frac{\Omega}{2}\left(\sigma^+ e^{i(\Delta k \cdot r - \mu t + \phi)} + \sigma^- e^{-i(\Delta k \cdot r - \mu t + \phi)}\right)$$

In this expression, σ^+ and σ^- represent the raising and lowering operators corresponding to the qubit (spin degree of freedom), $\Omega = \frac{\Omega_1 \Omega_2}{\Delta}$ represents the effective Rabi frequency. The term Δk corresponds to the difference in the wave vectors of the lasers along the radial direction of the ions, while $\mu = \omega_{\text{qubit}} - \Delta\omega$ denotes the laser detuning.

The spatial component of the Hamiltonian can be written in terms of the Lamb-Dicke parameter η as [6]

$$e^{i\Delta k\cdot r} = \exp\left[i\eta(ae^{-i\omega_r t} + a^\dagger e^{i\omega_r t})\right]$$

Here, ω_r represents the radial trap frequency. $a^\dagger$ and a represent the creation and annihilation operators that relate to the radial coordinate as $\hat{r} = \sqrt{\frac{\hbar}{2m\omega_r}}(\hat{a}^\dagger + \hat{a})$, and the Lamb-Dicke parameter is defined as $\eta = \Delta k\sqrt{\frac{\hbar}{2m\omega_r}}$.

The Lamb-Dicke regime is characterized by $\eta\sqrt{2\langle n\rangle + 1} \ll 1$, and especially when the ion is sufficiently close to the motional ground state, this condition reduces to $\eta \ll 1$. This requirement can be roughly interpreted as the wavelength of the laser being much larger than the ion's wave packet. In this regime, the spatial part of the Hamiltonian can be approximated as [6]

$$\exp\left(i\eta(ae^{-i\omega x t} + a^\dagger e^{i\omega x t})\right) \approx 1 + i\eta(ae^{-i\omega x t} + a^\dagger e^{i\omega x t})$$

With this approximation, neglecting higher-order terms of η, the Hamiltonian becomes

$$H = \frac{\Omega}{2}\sigma^+\left(1 + i\eta[ae^{-i\omega_r t} + a^\dagger e^{i\omega_r t}]\right)e^{-i\mu t + i\phi} + \text{h.c.}$$

The Hamiltonian takes a special form based on the parameter regime defined by μ.

When $\mu = 0$, which means the beatnote frequency $\Delta\omega = \omega_2 - \omega_1$ is tuned to be equal to the qubit frequency ω_{qubit} (where $\omega_1 = \omega_c$ as shown in Fig.2.7), the Hamiltonian takes the form of a carrier transition: [6]

$$H_{\text{Carrier}} = \frac{\Omega}{2}\left(\sigma^+ e^{i\phi} + \sigma^- e^{-i\phi}\right)$$

The Hamiltonian becomes $\frac{\Omega}{2}\sigma^x$, where σ^x represents the Pauli-x operator, when the phase $\phi = 0$. This term drives the single-qubit transition and is used to simulate a transverse magnetic field.

When $\mu = -\omega_r$ (where $\omega_1 = \omega_R$), the Hamiltonian takes the form:

$$H_{\text{RSB}} = \frac{\Omega}{2}\eta\left(\sigma^+ a e^{i\phi + \frac{\pi}{2}} + \sigma^- a^\dagger e^{-(i\phi + \frac{\pi}{2})}\right)$$

In this case, we can observe that this Hamiltonian both flips the qubit state and adds a motional phonon (when the qubit is in $|\downarrow_z\rangle$ state) to the system. It is important to

note that the effective rate is suppressed by the Lamb-Dicke parameter η compared to the carrier transition.

Similarly, when $\mu = +\omega_r$ (where $\omega_1 = \omega_B$), the Hamiltonian takes the form:

$$H_{\text{BSB}} = \frac{\Omega}{2}\eta\left(\sigma^+ a^\dagger e^{i\phi+\frac{\pi}{2}} + \sigma^- a e^{-(i\phi+\frac{\pi}{2})}\right)$$

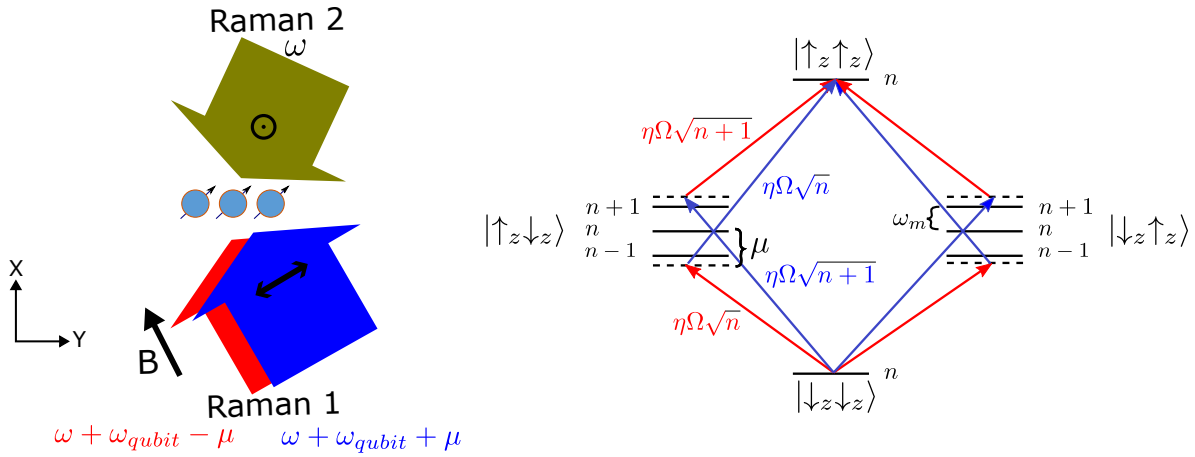

Figure 2.8: **Mølmer-Sørensen Scheme:** The left figure shows the orientation of the Raman lasers for the Mølmer-Sørensen scheme. Raman-1 beam consists of symmetrically detuned blue sideband and red sideband frequencies. The right figure shows the level diagram and illustrates how the frequencies of Raman lasers drive the entangling operations via off-resonant phonon excitation.

2.4.1 Mølmer-Sørensen Scheme

The Molmer-Sorensen scheme (Fig.2.8) [67] is a method for performing entangling operations between two qubits by leveraging the interaction between the qubits and collective motion. Detailed explanations of this protocol are presented in numerous reputable sources, including but not limited to references [68, 44, 92, 6]. Without delving into extensive detail here, I will provide a brief overview needed to understand the subsequent chapters.

In this scheme, both the blue sideband (BSB) and red sideband (RSB) transitions are simultaneously employed, with symmetric detuning given by $\mu_{RSB} = -\mu_{BSB} = \mu$ but with different phases. The Hamiltonian for a single ion is described as [6]:

$$H_{\mathrm{MS}} = \frac{\Omega}{2}\left(\sigma^{+}\left(1+i\eta(ae^{-i\omega_r t}+a^{\dagger}e^{i\omega_r t})\right)e^{-i\mu t+\phi_{\mathrm{RSB}}}+\mathrm{h.c.}\right) + \frac{\Omega}{2}\left(\sigma^{+}\left(1+i\eta(ae^{-i\omega_r t}+a^{\dagger}e^{i\omega_r t})\right)e^{i\mu t+\phi_{\mathrm{BSB}}}+\mathrm{h.c.}\right)$$

When accounting for multiple ions and various motional modes, this expression takes on a more complex form, [68, 44, 92, 6]:

$$H_{\mathrm{MS}} = \sum_{m=1}^{N}\sum_{j=1}^{N}\eta_{j,m}\Omega_j\cos(\mu t+\phi_m)\sigma_j^{\phi_s}(a_m e^{-i\omega_m t}+a_m^{\dagger}e^{i\omega_m t}) \tag{2.4}$$

By performing a Magnus expansion on the evolution operator, it is found that higher-order terms cancel out. In the regime where:

$$(|\mu-\omega_m| \gg \eta\Omega)$$

the effective Hamiltonian reduces to:

$$H = \sum_{i,j} J_{i,j}\sigma_i^x\sigma_j^x$$

with:

$$J_{i,j} = \Omega_i\Omega_j\left(\frac{\hbar\Delta k^2}{2m}\right)\sum_k \frac{b_i^k b_j^k}{\mu^2-\omega_k^2}$$

Here, Ω_i represents the carrier Rabi frequency determined by the intensity of the Raman beams, while μ refers to the detuning of the beams from the carrier transition. The terms b_i^k are amplitudes and ω_k are eigen frequencies shown in (Fig.2.3) depend on the trap parameters.

By varying the parameter μ in Eq.2.4.1, different interaction profiles can be obtained, as shown in Fig.2.9.

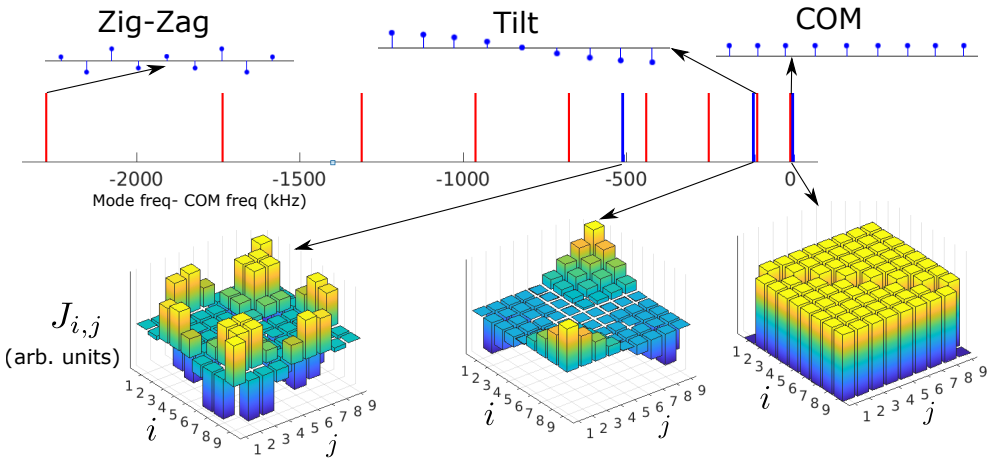

Figure 2.9: **Plethora of Interaction Profiles:** This figure illustrates the accessibility of various interaction profiles using the Molmer-Sorensen scheme by simply adjusting the detuning parameter μ. The plot considers 9 ions with trapping frequencies $\omega_{X'} = 5$ MHz and $\omega_Y = 1$ MHz.

Chapter 3

The Four-rod trap apparatus

This chapter provides a detailed description of the experimental apparatus used for the research presented in Chapters 4 and 5. The construction of the trap and vacuum chamber was undertaken in the first year of my PhD (2018-19), in collaboration with my colleagues Nikhil Kotibhaskar and Roland Hablützel. Additionally, various other components of the experiment, including but not limited to the laser and optical setup, individual addressing setup, Raman laser optics, electronics, and control system, were built in collaboration with Chung-You (Gilbert) Shih, Nikhil Kotibhaskar, Dr. Roland Hablützel, Dr. Manas Sajjan, Anthony Vogliano, Jingwen Zhu, Lewis Hahn, Dr. Yu-Ting Chen along with the help of various undergraduate research assistants. One of the main aspects of our experimental apparatus is the ability to perform the holographic beam shaping [93] led by Chung-You (Gilbert) Shih, enabled the experiments presented in subsequent chapters. This chapter aims to provide a comprehensive understanding of the working principles and detailed specifications of the four-rod trap quantum simulator apparatus. The work presented in these chapters has been partially published in the following references: [51, 93, 71].

3.1 Overview

The goals for building this apparatus are to trap a linear chain of approximately 10 ions to perform small-scale quantum simulations. The following are some of the unique features of the four-rod trapped ion quantum simulator:

- Trap a laser cooled chain of up to 10 ions with radial trap frequencies of about 1.2 MHz, with global and site-resolved high-fidelity detection

- Perform site-selective addressing of ions using resonant laser beams that can perform operations such as reset and detection
- Perform global coherent operations such as all single qubit rotations along the x,y,z axes, and two-qubit entangling operations

At the heart of the experimental apparatus lies the vacuum chamber that houses the four-rod Paul trap (Figure 3.1c), which in turn traps a linear chain of ions (Figure 3.1, top). The vacuum chamber that maintains a level of approximately 2×10^{-11} mbar pressure using the mounted vacuum pumps. The vacuum chamber also houses the atomic source and other electrical connections needed to power the Paul trap. Multiple coils needed for generating the required magnetic field are mounted to the chamber.

The vacuum chamber, placed on the optical table, is surrounded by various optics components, such as those delivering laser light needed for ionization (399 nm), Doppler cooling (369 nm), repumping (935 nm and 760 nm), and state detection (369 nm). This light is generated from external cavity diode lasers placed on the other end of the table (Figure 3.1j), which is transmitted through optical fibers to their respective preparation zones. At each preparation zone (Figure 3.1f, i), these laser light are split into multiple beams, frequency modulated, and then combined. These zones are also equipped with modulators that provide temporal control of these laser beams. Once necessary changes are made to their power and frequency, they are then coupled to another set of fibers that travel all the way to the chamber to be delivered to the trapped ions. In parallel, the frequency of these lasers is stabilized using measurements from either a wavemeter (Figure 3.1h) or a scanning cavity (Figure 3.1l).

The oscillating and static voltages needed for the electrodes in the trap are generated using various voltage sources that are modulated and amplified as required. The ions trapped in the trap are imaged from the top of the chamber using a microscope objective placed outside the viewport attached to the chamber. The light collected from the ions is detected using a detector (Figure 3.1a) to infer the presence and quantum state of the ions. Additionally, through the same path, another set of resonant laser beams is used to individually address the ions. The individually addressing light is spatially modulated using a Digital Micromirror Device (Figure 3.1a).

The coherent operations of the ions are driven using a pair of Raman laser beams. These beams are generated from an 8W pulsed laser (Figure 3.1e, g), which is split into two different paths: Raman 1 (Figure 3.1b) and Raman 2 (Figure 3.1d). These paths involve frequency modulation and beam shaping before addressing the ions.

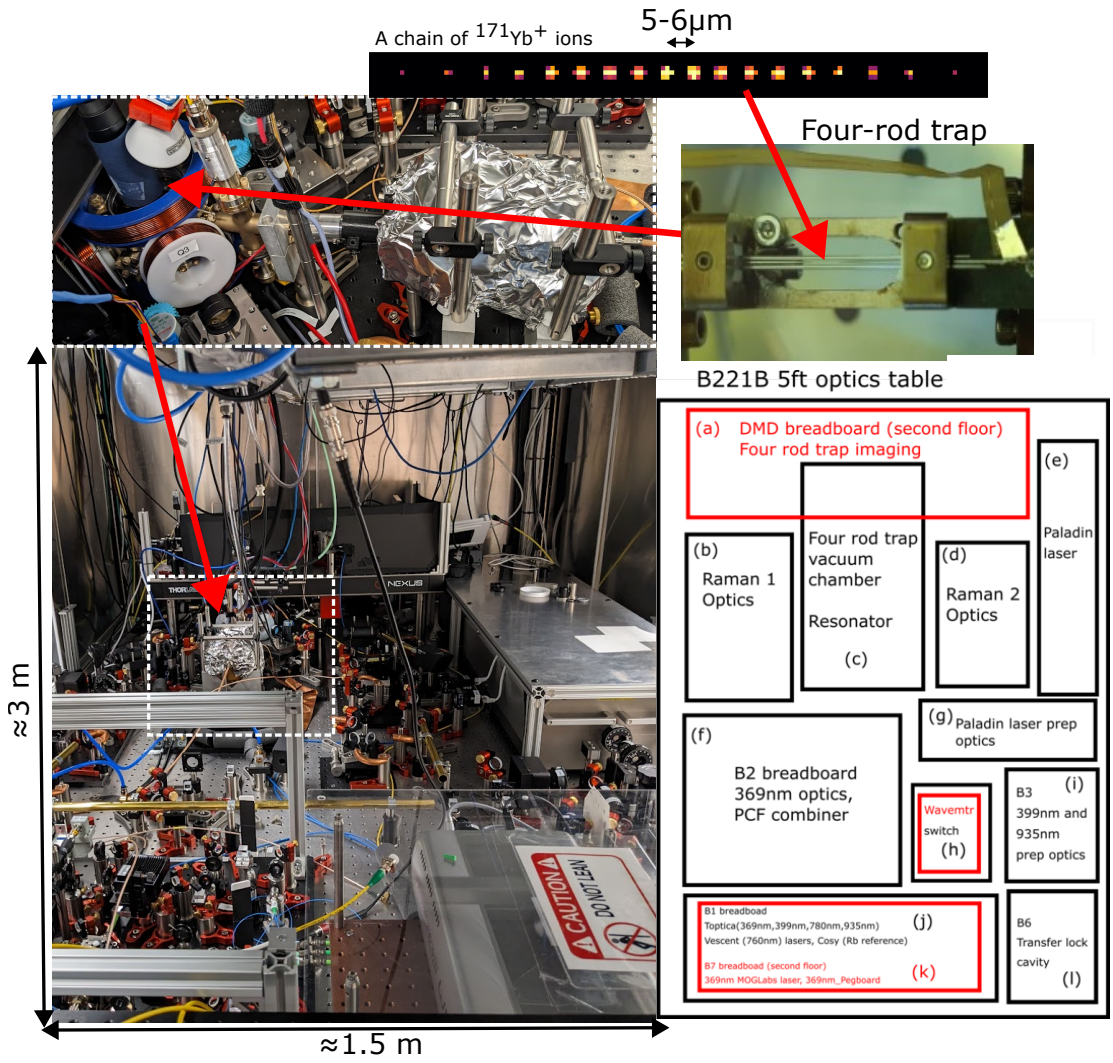

Figure 3.1: **Overall View of the Experimental Setup on a Single 5 ft x 10 ft Optics Table:** The vacuum chamber housing the four-rod Paul trap geometry (c) and the ions is shown. The external cavity diode lasers (j) generate the laser light for various processes, which is transmitted through fibers to the preparation zones (f, i). The light is then delivered to the chamber using optical fibers for the trapped ions. The Raman laser beams (b, d) are generated from the pulsed laser (e, g) and used for coherent operations. Note, that components in red denote components placed on a raised platform.

All these different equipment are controlled using an FPGA-based control system (developed by Sandia National Laboratory) that regulates the timing of when different components need to be turned on or off. The control system also collects light from various detectors to infer the state of the ions. Various independent feedback loops are in place to stabilize different parameters, ensuring the smooth operation of the experiment.

A typical experimental sequence on a given day contains an initial phase of initialization and calibration of the setup for the day. Here is an overview of the initialization process:

1. Turning on the lasers and frequency-locking them.
2. Trapping the ions (if there are none already) by activating the atomic oven and ionization lasers.
3. Verifying if the number of ions is as required for subsequent experiments.
4. Doppler cooling the ions.
5. Calibrating various other experimental parameters.

Once initialized, the following sequence of operations is performed for each quantum simulation experiment:

1. Doppler cooling the ions.
2. Initializing the ions to $|\downarrow_z\rangle$ using optical pumping.
3. Performing a π rotation using microwaves if the ions need to be initialized in the $|\uparrow_z\rangle$ state.
4. Performing a Raman sideband cooling sequence to cool the ions to the Lamb-Dicke regime.
5. Applying a sequence of Raman laser beam pulses to perform coherent operations.
6. Applying a sequence of mid-circuit reset beams in between the Raman laser pulses as needed for the experiment.
7. Applying the state detection beam and measuring the fluorescence using a detector to infer the state of the experiment.

Typically, each such sequence is repeated multiple times (100-200) to infer the state of the ion with a probability. A typical experimental sequence ranges from a few milliseconds to tens of milliseconds, and the ions in the trap do not need to be loaded every time, which greatly reduces the overhead of an experimental sequence.

With an overview of the operation of a trapped ion quantum simulator, the following sections delve into detailed information about our experimental apparatus.

3.2 Trap geometry

As discussed in Chapter 2, a Paul trap is utilized to create a confining potential for trapping a chain of ions by generating oscillating and static potentials. The trap geometry (Figure 3.2) consists of four tungsten rod electrodes and two tungsten needle electrodes, hence known as a four-rod trap. Each rod has a diameter of 0.5 mm. The rods are oriented parallel to the Y-axis and arranged in a square configuration in the XZ plane with a side length of d=1 mm. The distance between the surface of the rods and the Y axis, denoted by R_0, is 0.46 mm. The two needle electrodes, with pointed tips [51], are placed along the Y axis, facing towards the trap center, with a distance of 2.8 mm between their tips. The rods and needles are held together on a Macor holder, which is secured in place using a stainless steel bridge connected to the vacuum chamber.

An oscillating voltage of $V_0 \cos(\Omega t)$ is applied to two diagonally opposite rods, while a voltage of $-V_0 \cos(\Omega t)$ is applied to the other diagonal rods. Additionally, each rod can be biased independently with a static voltage, denoted as V^i_{bias}, where i is the rod index. A static voltage of V_{DC} is applied on the needle electrodes. The rods and needles provide radial and axial confinement with trapping frequencies $\omega_{\text{X}'}$ and $\omega_{\text{Z}'}$ along radial direction and ω_{Y} along axial direction. To remove the degeneracy of $\omega_{\text{X}'}$ and $\omega_{\text{Z}'}$ in the XZ plane, a bias voltage of V_{diag} is added to a pair of diagonally opposite electrodes, creating radial frequencies $\omega_{\text{Z}'}$ and $\omega_{\text{X}'}$ along the diagonal and anti-diagonal directions, respectively.

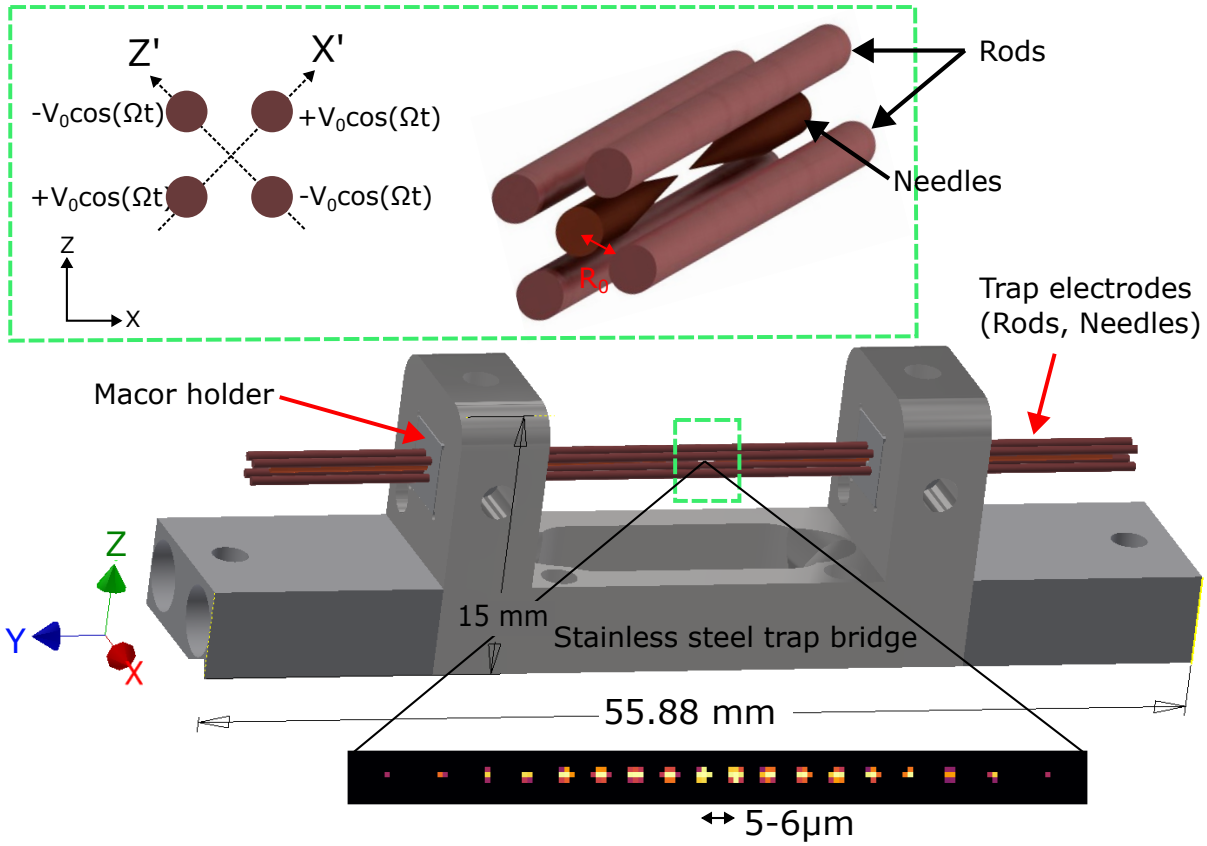

Figure 3.2: **Four-Rod Trap Geometry:** Tungsten rod electrodes (0.5 mm diameter) form a square configuration parallel to the Y axis in the XZ plane, with 1 mm spacing. Two pointed-tip needle electrodes are positioned along the Y axis, facing the trap center, with a 2.8 mm separation. Rods and needles are mounted on a Macor holder connected to the vacuum chamber with a stainless steel bridge. The dimensions mentioned in parentheses are in mm.

Our trap is driven at a frequency of $\Omega = 2\pi \times 20.28$ MHz with a voltage that generates an effective radial frequency of $\omega_{X'} \approx \omega_{Z'} \approx 2\pi \times 1.13$ MHz. With $V_{DC} \approx 100$ V, the trap provides an axial confinement of approximately $\omega_Y = 2\pi \times 200$ kHz. This trap geometry creates a potential that effectively traps a linear chain of ions aligned along the Y axis.

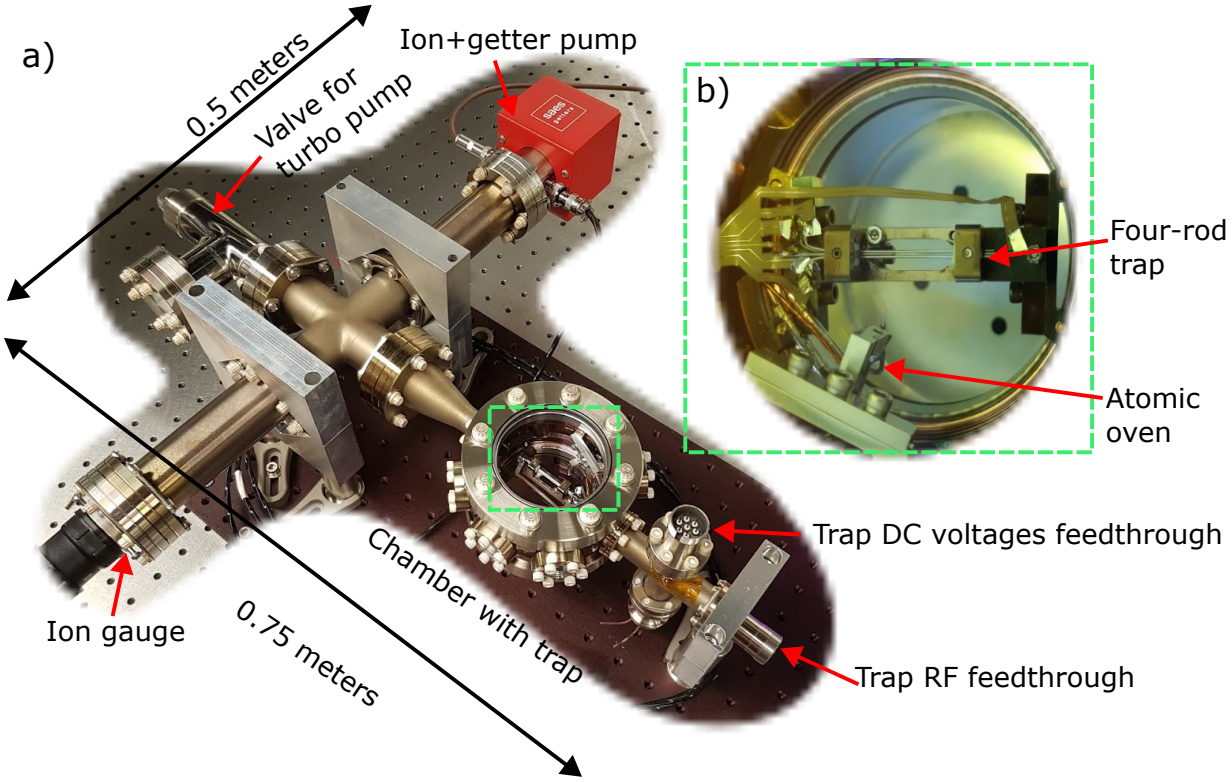

Figure 3.3: **Four-rod trap UHV assembly:** (a) Ultra-high vacuum chamber with flanges and pumps for maintaining pressures below 2×10^{-11} mbar. (b) Atomic oven inside the chamber for generating neutral Yb atoms, positioned towards the trap center.

3.3 Four-rod trap UHV assembly

The four-rod trap is housed inside an ultra-high vacuum chamber (Figure 3.3a), which is maintained at pressures below 2×10^{-11} mbar. Operating at such low pressures, we typically observe only 1-2 background collisions events every 10 minutes for a chain of 10 ions. The trap is mounted on a science chamber (Kimball Physics octagon) using groove grabbers. The chamber features eight 1.33-inch flanges and two 4.5-inch flanges. To maintain the vacuum level in the chamber, a combination of SAES ion pump and getter pump is employed. Pressure measurements are carried out using a Bayard-Alpert ion gauge, which has an X-ray limit of 2×10^{-11} mbar. More details of the vacuum assembly construction are described in Ref. [50].

An atomic oven, located inside the chamber and pointing towards the center of the trap

(Figure 3.3b), consists of a stainless steel tube containing a small Ytterbium metal chunk (about 20-30 mg). High currents, typically around 6.5A, are passed through the oven to heat it to temperatures ranging from 100°C to 150°C, generating a plume of neutral Yb atoms that are subsequently ionized in the trapping region.

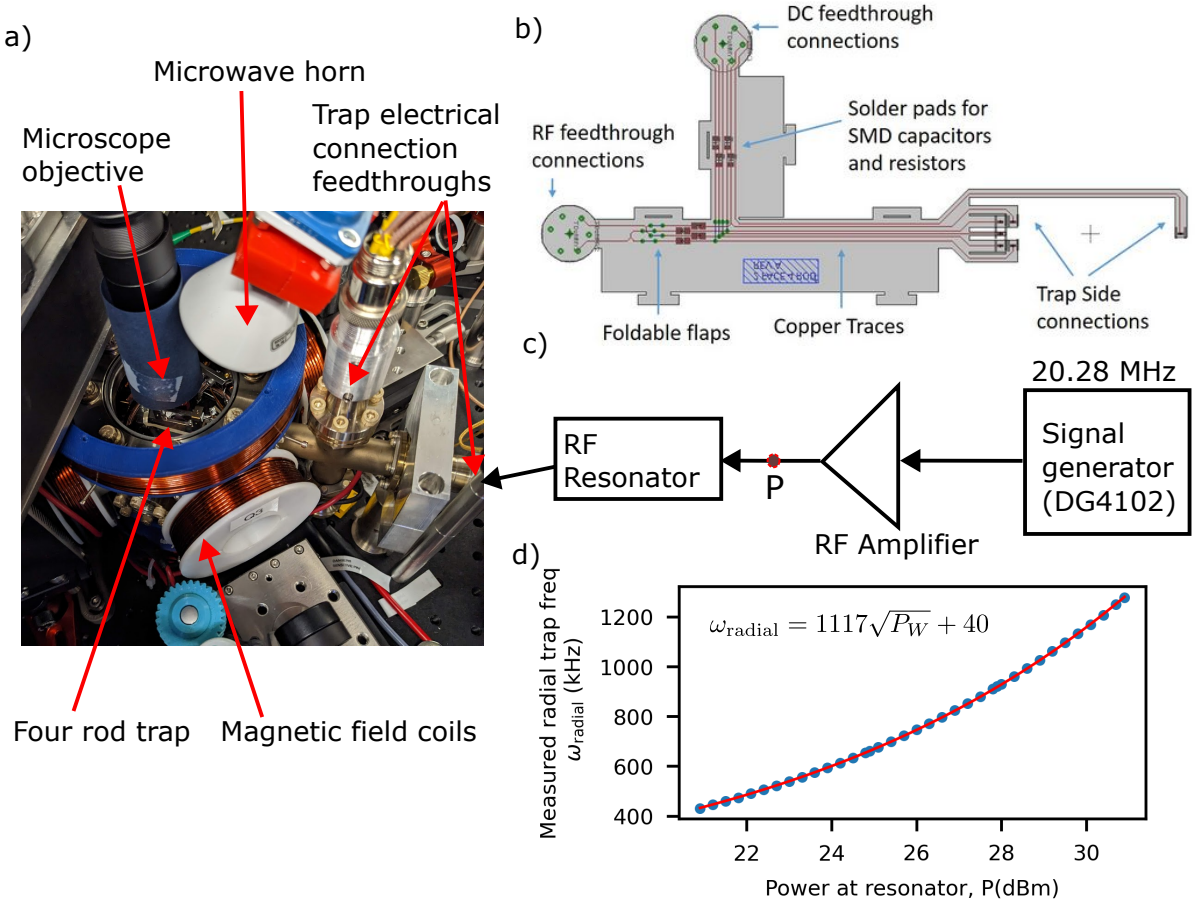

Figure 3.4: **Four-rod trap external attachments:** (a) UHV assembly with brackets, coils, and microwave horn. (b) Flexible printed circuit board (FPCB) connecting feedthroughs to trap electrodes. (c) Signal generator (DG4102), RF amplifier (MPA40-40), and RF resonator [88] (d) Calibration curve for input power to the resonator (P in dBm) and radial trap frequency. Here $P_W = 10^{P/10-3}$ is power at the input of the resonator in Watts.

The other side of the chamber is connected to the feedthrough assembly, which provides

the necessary electrical connections for the trap electrodes and the atomic oven. The RF voltages applied to the trap electrodes are generated from a signal generator (DG4102) and amplified using an RF amplifier (Fig. 3.4c). The amplified signal is then fed into a home-built RF resonator [88](Fig. 3.4c). Here, the RF resonator serves multiple purposes, such as impedance matching of the trap circuit with the signal generator for efficient power transfer, voltage amplification needed to generate high voltages (100-400V amplitude), and frequency selectivity, which helps in rejecting unwanted signals at other frequencies. The circuit, consisting of the RF resonator, the electrical connections, and the trap, forms an effective RLC resonant circuit. The resonant frequency of this circuit is about $\Omega/(2\pi) = 20.28$ MHz. The signal generator is programmed to generate this frequency by minimizing the reflections from the RLC circuit. The voltage output from the resonator is connected to a UHV feedthrough, which is in turn connected to a flexible printed circuit board (Fig. 3.4b) [50], placed inside the vacuum chamber. This flexible printed circuit board (FPCB), which is also connected to another feedthrough carrying the DC voltages for rods and needles, carries the signals from the feedthroughs to the trap electrodes. The FPCB also contains various capacitors and resistors required for biasing the RF voltages of the rods with a bias voltage V_{bias}. The relationship between the power supplied to the input of the RF resonator and the voltage at the electrodes depends on the properties of the resonator, such as the quality factor Q, resistance R, inductance L, and capacitance C of the circuit. The voltage at the electrodes for an input power P (W) to the resonator is given by [97]:

$$V_0 = \sqrt{2PQ\sqrt{\frac{L}{C}}}$$

The relationship between the radial trap frequency of the pseudopotential is given by [97]:

$$\omega_{\text{radial}} = \frac{\sqrt{2}eV_0\eta}{mR_0^2\Omega}$$

where e is the charge of an electron, m is the mass of the $^{171}\text{Yb}^+$ ion, and η is a geometric factor. The relationship between the input power P and ω_{radial} is calibrated using experiments and shown in Fig. 3.4d.

The entire UHV assembly is securely mounted using aluminum brackets that are fastened to the optics table. Additionally, six coils (shown in Fig. 3.4a) are affixed to the chamber to generate a magnetic field of approximately 2 G in a desired direction for the experiment. A microwave horn (Fig. 3.4a) is also positioned near the chamber to apply a

microwave with a frequency of 12.6 GHz to the ions, inducing transitions from the states $|\uparrow_z\rangle$ and $|\downarrow_z\rangle$.

3.4 Optical layout

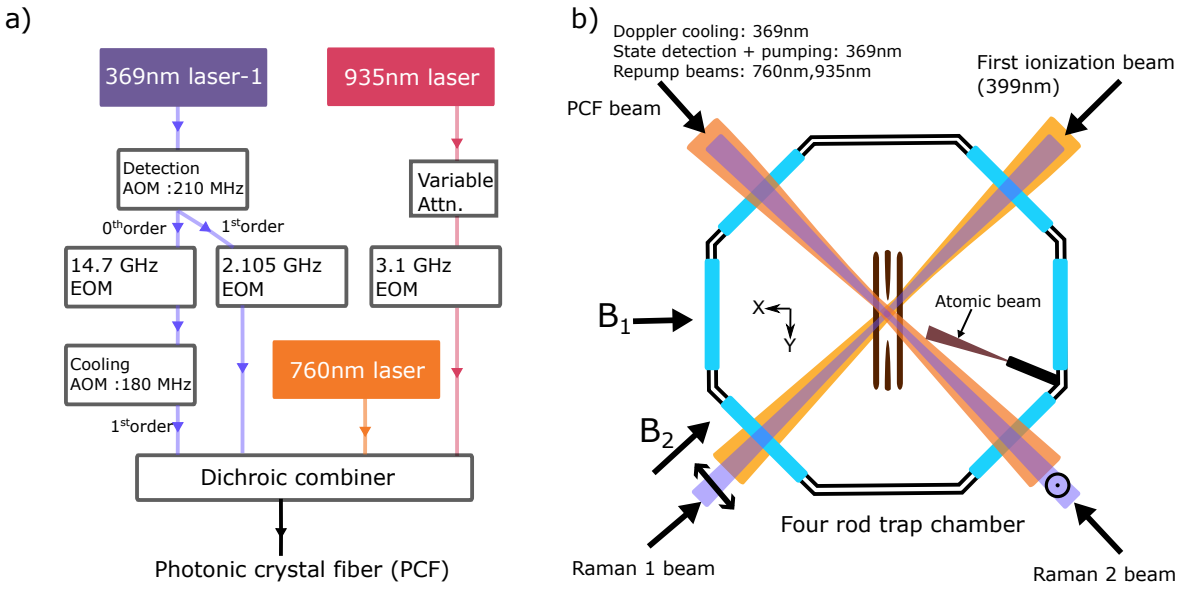

Figure 3.5: **Four-rod trap beam delivery layout:** (a) Frequency modulation layout for various lasers (369 nm, 760 nm, and 935 nm) using AOMs and EOMs. Beam combining is achieved through beam splitters and dichroic mirrors to a single Photonic crystal fiber(PCF) fiber. (b) Schematic of beam delivery to ions in the XY cross-section of the science chamber. Magnetic field orientations (B_1 and B_2) for different experiments are shown. Light from PCF is focused on ions using a parabolic reflector. Raman beams (Raman 1 and Raman 2) are directed diagonally opposite to PCF and ionization beams, forming a 90-degree angle between them.

With the internal and external components assembled in the UHV chamber, the remaining apparatus (Fig. 3.1) primarily focuses on delivering various lasers for processes such as ionization, cooling, optical pumping, repump, state detection, and coherent operations with Raman beams. Figure 3.5a presents the layout for frequency modulation of the 369 nm, 760 nm, and 935 nm lasers. A 369 nm ECDL (369 nm laser-1) is frequency modulated

using a 210 MHz Acousto-optic modulator (AOM). The first-order sideband generated by the AOM is used for state detection, and the 369 nm laser-1 is parked at a frequency 210 MHz away from the transition frequency. The detection light is further modulated by a 2.1 GHz Electro-optic modulator (EOM) to generate light for optical pumping. Both modulators are selectively turned on and off as required for the experiment. The zeroth-order light of the detection AOM is modulated using a 14.7 GHz EOM and an AOM at 180 MHz to generate the light necessary for Doppler cooling. The Doppler cooling light, generated through these modulators, is detuned by 30 MHz from the detection transition. Simultaneously, a 935 nm laser is modulated using a 3.1 GHz EOM to produce light for the repump process. Additionally, a voltage variable attenuator is included in the path to control the intensity of light on-demand, crucial for micromotion compensation. The 369 nm light for state detection, optical pumping, and cooling, along with the 935 nm light for repump and 760 nm light for F-state repump, are combined using beam splitters and dichroic mirrors. These combined beams are then guided into a single polarization-maintaining photonic crystal fiber, operating in single mode, capable of accommodating a wide wavelength range from 369 nm to 935 nm. Additionally, light sampled from all these lasers is also directed through a wavemeter and/or a Fabry-Perot cavity for the purpose of stabilizing laser frequencies [70].

Figure 3.5b depicts the schematic of how various beams are delivered to the ion in the XY cross-section of the science chamber, with the trap located at the center. Six 1.33-inch viewports are utilized to deliver the different laser beams. The figure also illustrates the orientation of the magnetic field, which defines the quantization axis and induces Zeeman splitting. The magnetic field's orientation can be adjusted by modifying the current in the respective coils. In the experiments described in Chapter 4, the magnetic field is aligned along the x-axis (represented by B_1), while in the experiments detailed in Chapter 5, the magnetic field is oriented at a 45-degree angle from the x-axis (represented by B_2), as shown in Figure 3.5b. This disparity in orientation is primarily due to modifications made to the experimental apparatus between the times when the experiments were conducted. The light emitted from the photonic crystal fiber (PCF)[1] is directed towards the ions using a parabolic reflector, which passes through a 1.33-inch viewport located on the top left side. The beam waist for all PCF beams incident on the ions is approximately 50 µm ($1/e^2$ radius). However, it is important to note that there is a minor variation of around 5% among different wavelengths. To control the polarization of the light, a polarizer[2] is employed, followed by a $\lambda/2$ waveplate [3], which allows for the rotation of the polarization.

[1] NKT photonics single mode, polarization maintaining fiber LMA-PM-10. MFD≈8.6 μm

[2] Ultra Broadband (250 nm - 4 µm) Wire Grid Polarizer: Thorlabs WP25M-UB

[3] The waveplate is designed for 369nm

For first ionization, the light (399nm) is delivered through another viewport using a single-mode fiber, positioned at an angle of approximately 70-80 degrees relative to the atomic beam flux generated from the oven.

The Raman lasers, denoted as "Raman 1 beam" and "Raman 2 beam", are directed towards the ions from diagonally opposite viewports compared to the PCF and ionization beams. The pair of Raman beams form an approximate 90-degree angle with each other. The polarization of the Raman 1 beam is perpendicular to the magnetic field B_2 along the XY plane, while the polarization of the Raman 2 beam is perpendicular to the magnetic field B_2 along the Z-axis. Both Raman beams have an elliptical shape, with the minor axis aligned along the Z-axis. They are focused onto the ions with beam waists($1/e^2$ radius) of around $65\mu\text{m} \times 3\mu\text{m}$. Further details regarding the layout of the Raman beams will be presented later in the chapter.

3.4.1 Ion imaging and individual addressing

In addition to the above optical layout, our apparatus has the ability to perform individual addressing by using state-detection or optical pumping beams along the Z-axis. The ions are also imaged in the same direction onto a detector using the same optical layout. Figure 3.6 illustrates the optical layout employed for individual addressing and ion imaging [71]. This optical layout is utilized for the experimental results presented in chapters 4 and 5. As described earlier, global Doppler cooling, state-detection, and optical pumping are all derived from a laser source (369 nm-laser-1), along with repump beams (935 nm, 760 nm), which are illuminated onto the ions in the XY plane. The fluorescence emitted by the ions is collected through a home-built objective and directed onto either a photomultiplier tube (PMT) [4] or a qCMOS camera using a pellicle beam splitter (45:55) [5]. A flip mirror is employed to switch between the PMT and qCMOS camera. The state-dependent fluorescence transmitted after the trap is also monitored using a CMOS camera C2 [6], as depicted in Figure 3.6.

For the experiments presented in chapter 4, a magnetic field (B_1) perpendicular to the ion chain is applied, while for the experiments in chapter 5, a magnetic field B_2 at a 45-degree angle to the X-axis in the XY plane is utilized. These magnetic fields provide the quantization axis and induce a Zeeman splitting of $\Delta_{zm} = 2\pi \times 3.25$ MHz between the $S_{1/2}\,|F = 1, m_F = 0\rangle$ and $S_{1/2}\,|F = 1, m_F = 1\rangle$ levels. A probe beam along the Z-axis is

[4] Hamamatsu: H10682-210
[5] Thorlabs: BP145B5
[6] FLIR: Blackfly S BFS-PGE-04S2M

directed onto the ions through an addressing system with an effective numerical aperture (NA) of 0.16(1). This probe beam is resonant with either the $D_1^{(10)}$ or $D_1^{(11)}$ transitions, allowing for site-selective state reset or measurement. We employ another 369 nm laser source (369 nm-laser-2) for the probe beams, whose frequency can be independently tuned without affecting the global detection and cooling beams. An acoustic-optic modulator (AOM1), configured in a double pass, is placed after the 369 nm-laser-2 source. It serves as a switch with precise timing and power control for the probe light.

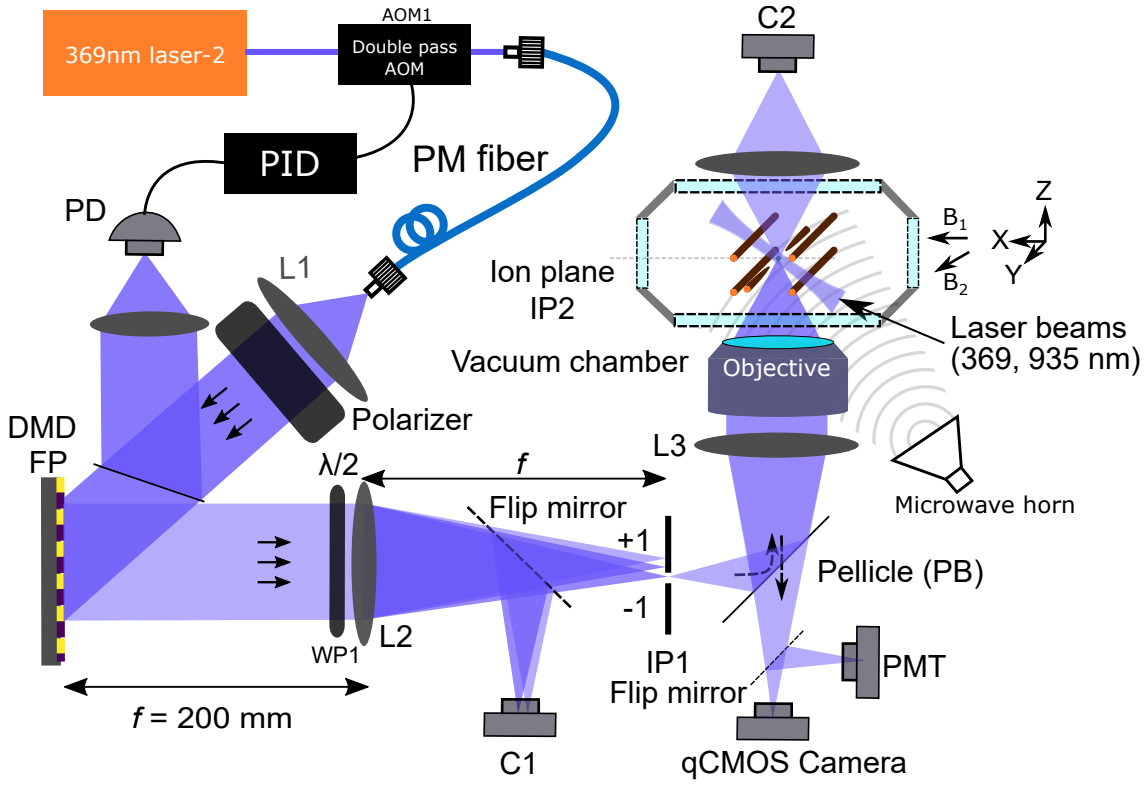

Figure 3.6: **Four-Rod Trap Imaging and Addressing Schematic:** The ions located in the center of the vacuum chamber are imaged onto a qCMOS camera through an objective. The same objective is used to illuminate the ions with 369 nm light, which is spatially modulated using a Digital Micromirror Device (DMD).

The light is coupled to a polarization-maintaining (PM) fiber, which is then expanded to approximately 5mm (beam waist) using a single lens (L1) and polarization-cleaned using a polarizer. The light is sampled by a photodiode (PD) that stabilizes the intensity fluctua-

tions using PID feedback to the AOM. The polarization-cleaned and power-stabilized light from the PM fiber illuminates a Digital Micromirror Device (DMD) (Visitech Luxbeam 4600 DLP) placed in the Fourier plane of the focusing lens L2 (f=200mm). The diffracted first-order beam from the hologram on the DMD is then relayed to the ions through the reflection of the pellicle. A flip mirror placed before the intermediate image plane IP1 is used to image IP1 onto camera C1 for initial characterization. Additionally, a motorized $\lambda/2$ waveplate (WP1) is positioned after the DMD to control the final polarization of the light.

3.4.2 Holographic beam addressing

The DMD placed in the Fourier plane consists of a grid of 1920 x 1080 tiny mirrors, with each mirror measuring 10.8 μm. These mirrors can be individually controlled to switch on and off as required, allowing us to have precise control over the spatial amplitude profile of the reflected light. Thus, the DMD serves as a spatial light modulator, enabling us to manipulate both the amplitude and phase of the light incident on the ion.

Since the DMD is positioned in the Fourier plane of lens L2 (Figure 3.6), the light in the image plane IP1 corresponds to the Fourier transform of the profile displayed on the DMD. By selectively activating or deactivating the mirrors, we can control the amplitude profile on the DMD, consequently achieving amplitude control in the image plane. This approach is particularly advantageous when generating an intensity profile with features of approximately 1 μm in size. By utilizing the DMD in the Fourier plane, we can generate these features even though the individual mirrors on the DMD are relatively large (10 μm), which is in contrast to using the DMD directly in the image plane.

However, using the DMD in the Fourier plane only provides amplitude control and not phase control of the incident light on the ion. To achieve phase control, we program the DMD with a grating and then relay the first diffracted order of light from the grating to the ion [93]. By manipulating the phase of the grating, we can change the phase of the light incident on the ion, thus gaining control over the phase component as well.

If the goal is to generate a beam profile with a complex electric field described by the function $f(\mathbf{x}')$ on the ion plane, along with its Fourier conjugate $F(\mathbf{k}') = \mathcal{F}[f(\mathbf{x}')]$, we can program an amplitude hologram using the expression [93]:

$$G(\mathbf{k}') = \eta \left| \frac{F(\mathbf{k}')}{E_{\text{in}}(\mathbf{k}')} \right| \frac{1}{2}(\cos(\mathbf{k}' \cdot \mathbf{x_0}' + \Phi(\mathbf{k}') - \Phi_{\text{in}}(\mathbf{k}')) + 1), \tag{3.1}$$

In Equation (3.1), $|E_{\text{in}}(\mathbf{k}')|$ and Φ_{in} represent the amplitude and phase of the input beam profile incident on the DMD. The expression calculates the amplitude hologram $G(\mathbf{k}')$ for

programming on the DMD to achieve the desired beam profile on the ion plane. The parameter η adjusts the overall intensity of the hologram. The beam profile generated by programming such a beam profile onto the DMD can be extracted by taking the Fourier transform to get

$$\begin{aligned} E_{\mathrm{IP}}(\mathbf{x}') &= \mathcal{F}^{-1}[(E_{\mathrm{in}}(\mathbf{k}')G(\mathbf{k}'))] \\ &= \eta \left(\frac{1}{4} f(\mathbf{x}' + \mathbf{x_0}') \right. \\ &\quad + \frac{1}{4} f^*(-(\mathbf{x}' - \mathbf{x_0}')) * \mathcal{F}^{-1}[\mathrm{e}^{\mathrm{i}(2\Phi_{\mathrm{in}}(\mathbf{k}'))}] \\ &\quad \left. + \frac{1}{2} \mathcal{F}^{-1}[|F(\mathbf{k}')|\mathrm{e}^{\mathrm{i}\Phi_{\mathrm{in}}(\mathbf{k}')}] \right), \end{aligned} \tag{3.2}$$

The first term in the above expression represents the -1 diffraction order beam, which exhibits the desired beam profile but at a shifted position $\mathbf{x_0} = \frac{\lambda f}{a}$, where $\mathbf{a}$ is the grating periodicity. However, since the DMD only has binary amplitude control, an iterative Fourier transform algorithm (IFTA) from Ref. [93] is employed to create a binary hologram that accurately generates the required beam profile with minimal error. A binary amplitude hologram with a periodicity of $a = 4 \times 10.8$ is programmed onto the DMD to modulate both the phase and amplitude of the incident light's electric field. Additionally, the DMD is programmed with an aberration-corrected binary amplitude hologram generated using the iterative Fourier transform algorithm (IFTA) described in Ref. [93]. This hologram enables the production of a Gaussian beam with a waist of $w = 1.50(5)\mu m$ in the ion plane (IP2). Further details regarding the addressing of the probe beam and aberration correction will be presented in Chapter 4.

3.4.3 Raman optical path layout

To implement coherent operations such as single-qubit operations and entangling operations (described in chapter 2), we employ a pair of Raman beams with a frequency difference close to the qubit transition frequency of 12.642 GHz. Generating Raman beams with such a large frequency difference is challenging using frequency modulators like acousto-optic modulators (AOMs) and electro-optic modulators (EOMs) due to their limited bandwidth and efficiencies. Therefore, instead, we utilize a pulsed laser at 355 nm [7] that produces 15ps pulses with a repetition rate of 80.343 MHz.

[7] Coherent Paladin Advanced 355-8000

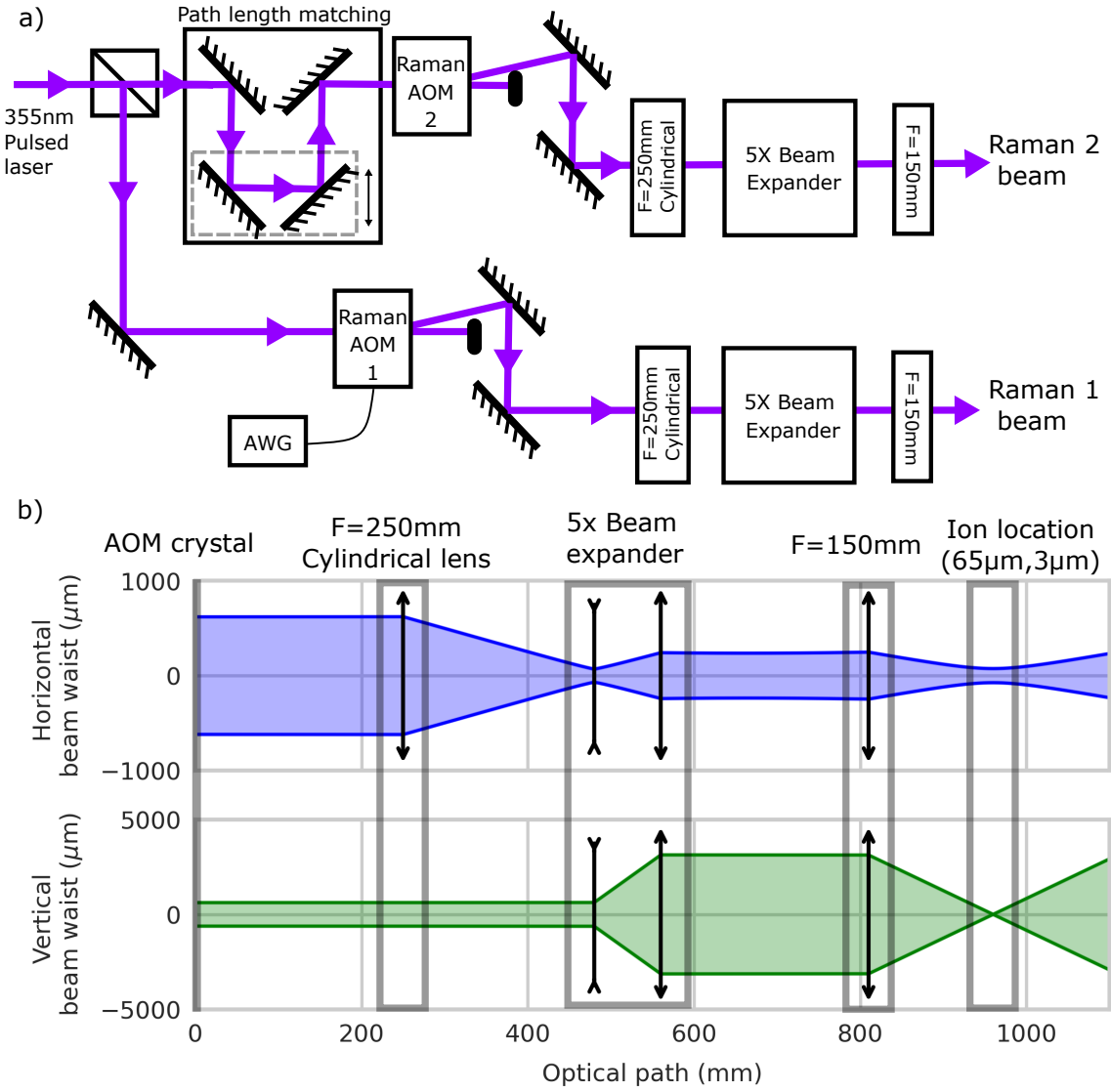

Figure 3.7: **Four-rod Raman schematic:** Schematic of the optical setup for driving Raman transitions using 355 nm light. (a) The 355 nm laser light is split into two paths, each frequency modulated using acousto-optic modulators (AOMs). The beams are shaped using optics and focused onto the ions. (b) Beam waist function along the horizontal (ion chain) and vertical (perpendicular to the ion chain) directions, optimized for maximum power utilization on the ions. The AOM crystal is directly imaged onto the ions in the horizontal direction to minimize frequency shift effects.

In the frequency domain, this corresponds to a frequency comb with peaks spaced by the repetition rate of 80.343 MHz. We select this repetition rate such that the frequency difference between the nth and (157+n)th peak is approximately 12.613 MHz. It is important to note that this value is approximately 30 MHz away from the qubit transition frequency of 12.642 GHz. By splitting the light from the 355 nm laser into two paths and frequency shifting one path by 30 MHz with respect to the other, we can drive the Raman transitions using this pair of beams.

Figure 3.7a illustrates the optical schematic for driving the Raman transitions using 355 nm light. The light from the 355 nm laser is divided into two paths using a beam splitter. Each path undergoes frequency modulation using two AOMs. These AOMs are driven at frequencies of approximately 211 MHz and 182 MHz, respectively, resulting in a frequency difference of about 30 MHz, which is sufficient to drive the Raman transitions with the ions. The light in each path is then shaped using optics consisting of a cylindrical lens with a focal length of 250mm, a 5x beam expander (Edmund optics, 5X, UV-VIS Vega), and a final lens with a focal length of 150mm. This optical setup generates an elliptical beam with beam waist dimensions of 65 μm x 3 μm, which is focused onto the ions.

Figure 3.7b demonstrates the beam waist function along the horizontal (aligned with the ion chain) and vertical (perpendicular to the ion chain) directions. Since the ions are arranged in a linear chain, we choose this beam shape to maximize the power usage on the ions, thereby reducing the beam waist perpendicular to the ion chain. Additionally, the optical setup is designed such that the AOM crystal is directly imaged onto the ions in the horizontal direction. This configuration ensures that the frequency shift in the AOM drive frequency does not affect the beam incident on the ions.

Chapter 4

Minimizing accidental quantum measurements (AQMs)

One of the main goals of my thesis is to demonstrate the capabilities of performing operations such as spin reset and spin measurements (mid-circuit measurements and reset) on ion qubits during quantum simulations. This chapter discusses the challenges involved in achieving these operations, how we mitigate these issues, and provides detailed characterization to demonstrate the capabilities of this process. Most of the work presented in this chapter has been published in Ref. [71]. I along with my colleagues, Chung-You(Gilbert) Shih, Anthony Vogliano, Lewis Hahn, and Jingwen Zhu performed the experiments following an initial feasibility study along with Roland Hablutzel, Chung-You(Gilbert) Shih and myself. I along with my colleagues Nikhil Kotibhaskar and Darian McLaren performed theory calculations, numerical simulations, and analyses. I wrote the majority of the manuscript with valuable assistance from Anthony Vogliano, and my supervisor Rajibul Islam. All the authors contributed to the scientific discussions. Rajibul Islam supervised the whole project.

4.1 Overview

The incoherent processes of state-reset and measurement (described in previous chapters) are performed on trapped ion quantum simulator by shining resonant laser beams and collecting the light scattered from the ions(for state measurement). Due to the close proximity of the ions, with a spacing of 4-6 μm, performing these operations on a subsystem

while maintaining coherence in the remaining system poses a significant challenge. As a result, most state-of-the-art experiments perform these processes globally.

However, the ability to perform measurements and resets on a subsystem in the middle of coherent dynamics, known as 'mid-circuit measurements and resets,' is a powerful tool for simulating new classes of quantum phenomena. These include measurement-driven quantum phase transitions [76, 19, 58, 98, 14, 89, 55], reservoir engineering with controlled dissipation [66] and executing quantum error correction protocols [52, 87, 94].

One of the main challenges in achieving mid-circuit measurements and resets is the occurrence of accidental quantum measurements (AQM) in the remaining system during the process. These AQMs introduce errors in quantum simulation that cannot be fixed by subsequent operations, unlike coherent errors that can be corrected by adding corrective gates. Even a single photon can cause a measurement on the remaining subsystem through accidental scattering, resulting in a finite probability of AQM (P_{AQM}). This probability can be prohibitively high since the typical inter-atomic separation is comparable to the optical resolution.

In this chapter, we demonstrate the preservation of the quantum state of an 'asset' ion qubit with high-fidelity while resetting or measuring a neighboring 'process' qubit at a distance of a few microns. We achieve $P_{\mathrm{AQM}} < 1 \times 10^{-3}$ for the asset qubit during the process qubit reset operation and $P_{\mathrm{AQM}} < 4 \times 10^{-3}$ while applying detection light to the process qubit with experimentally demonstrated [18] fast detection times. These low probabilities of AQM correspond to retaining the quantum state of the asset qubit with fidelities above 99.9% and 99.6% for the reset and measurement processes, respectively.

Our explorations, presented here, also provide a framework for optimizing multidimensional optical parameters to maximize in-situ operation fidelity. The in-situ incoherent operations are enabled by exquisite control over optical wavefronts from a holographic addressing system [93], which compensates for aberrations detected using a single ion's quantum state. This approach relies on robust optical engineering rather than special trapping architectures and can be adapted to other atomic quantum information processing systems.

The high-fidelity results we demonstrate immediately enable explorations of novel measurement-driven quantum simulation protocols [19] and open quantum systems, such as quantum simulations with local dissipation and measurements, and quantum reservoir engineering. Our results demonstrate errors smaller than the 0.5% threshold, which signifies the break-even point for various error correction schemes [63, 15]. While the surface code implementation discussed in Ref. [63] accounts for errors originating from the entire measurement process, the high-fidelity state detection of the target process qubit, estab-

lished with trapped ions, effectively restricts the total errors to those defined by the fidelity of the asset qubits

Further, the in-situ operations demonstrated provide scalable, simple, robust, and fast quantum information processing protocols compared to other error mitigation techniques, such as shuttling and the use of ancilla for mid-circuit measurements.

4.1.1 Chapter outline

The chapter begins with a formal statement of the problem, outlining the specific challenges related to the measurement of P_{AQM}. This is followed by a detailed analysis of the theoretical methods used to quantify, measure, and characterize the P_{AQM} in the experimental setup.

Next, I present our proposed scheme for reducing the P_{AQM}, outlining the strategies and techniques employed. This is followed by a discussion of high dynamic range measurements that enable us to accurately quantify the P_{AQM}.

The chapter then delves into the details of the calibration steps necessary to achieve precise quantification of the P_{AQM}. In the remaining chapter, a thorough exploration of different experimental parameters is conducted, aiming to minimize the P_{AQM} as much as possible. Various optimization techniques are employed to enhance the accuracy and reliability of the state reset and measurement processes.

By the end of the chapter, a comprehensive understanding of the challenges and strategies related to the reduction of P_{AQM} is provided, along with insights gained from the optimization of experimental parameters.

4.2 Problem statement

Consider a chain of ions in a trapped ion quantum simulator as shown in Figure 4.1. The task is to perform a state-reset or measurement only on the ion labeled as the "process ion" (ion2). However, during the addressing of the "process" qubit, the "asset" qubit located at a distance a away may be subject to accidental measurement due to photons scattered from ion2 or intensity crosstalk caused by imperfect optical addressing.

To assess the preservation of the asset qubit's state, we can quantify the damage inflicted by considering the probability of accidental measurement (P_{AQM}). This metric reflects the likelihood of the asset qubit being measured during the process. It is important to note

that we assume the asset qubit and the process ion are not entangled since entanglement would result in the collapse of the asset qubit's state upon measuring the process ion, which cannot be avoided.

Alternatively, we can use the fidelity metric [74] defined as

$$F = \mathrm{tr}\left(\sqrt{\rho^{1/2}\rho'\rho^{1/2}}\right), \tag{4.1}$$

to quantify the preservation of the quantum state of the asset qubit. Here ρ and ρ' denote density matrix operators of asset qubit before and after the operation on process qubit. In the case where P_{AQM} is significantly smaller than 1, P_{AQM} can be approximated as the infidelity $(1 - F)$.

Using these metrics, we can investigate the sources of accidental quantum measurements (AQMs) and explore methods to characterize and reduce them.

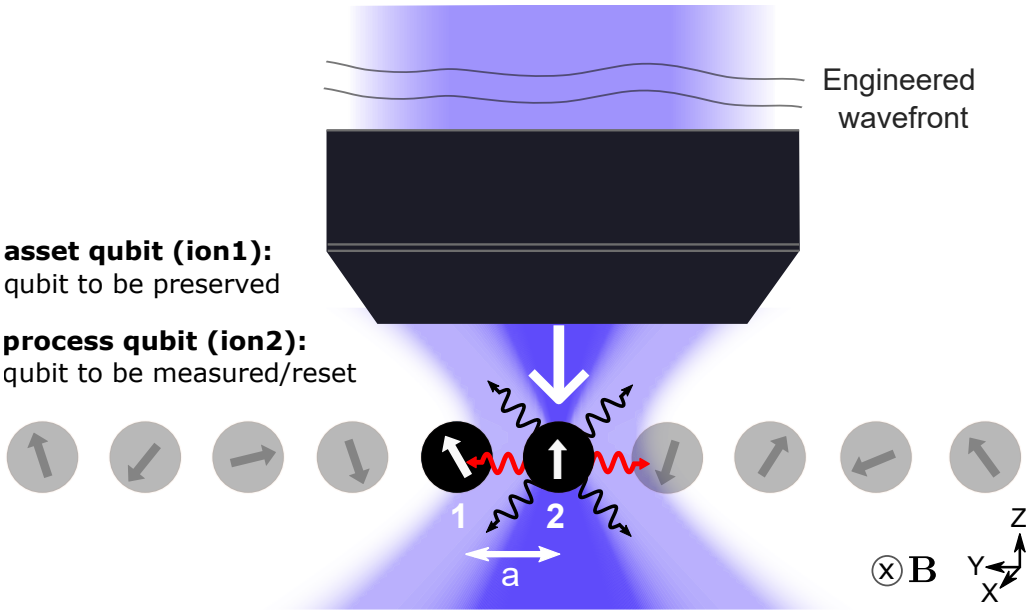

Figure 4.1: **Accidental Quantum Measurement (AQM) of Neighboring Qubits:** This figure illustrates two key factors that affect AQM of ion1 during measurement or reset of ion2: finite intensity crosstalk (lightly shaded violet) and inter-ion scattering (red wavy lines).

4.3 Sources of AQMs

Figure 4.1 describes the two mechanisms for AQM of the asset qubit (ion1) during a measurement or reset on the process qubit(ion2): finite intensity crosstalk (due to imperfect optical addressing) and inter-ion scattering (absorption of photons emitted by ion2). While both the state reset and detection generally constitute quantum measurements, in practice, detection involves at least an order of magnitude more scattered photons due to the inefficiency of the measurement apparatus. While in principle collecting a single photon scattered from the process ion could be sufficient to infer its state, even the state-of-the-artimaging systems do not exceed the photon collection efficiency of more than 5%. On top of this, there is additional background scattering and detector noise that needs to be considered. Thus state-detection needs the process ion to be probed for longer duration till the detector gains enough confidence of the process ion's state. Consequently, due to the increased number of scattered photons as well as finite intensity crosstalk from the laser beam, P_{AQM} will increase with detection time. However, advances in state measurement techniques and protocols have enabled high-fidelity detection in $\sim$ 10 µs [18]. This high-fidelity detection in a short duration by authors in [18] was possible by using a Superconducting nanowire single-photon detector (SNSPD) which has high (almost double) quantum efficiency of detecting the photons compared to commercial photo multiplier tube (PMTs). The fast detection times allow in-situ, site-selective measurement of the process qubit with $P_{\mathrm{AQM}} \sim 10^{-3}$ for the asset qubit as long as the intensity crosstalk can be contained below 10^{-4} level. Here, the intensity crosstalk ($I_X = I_1/I_2$) is defined as the ratio of the optical intensity of the addressing beam on the asset qubit (I_1) to that on the process qubit (I_2). Inter-ion scattering sets a fundamental limit to P_{AQM} of $P^*_{\mathrm{AQM}} \sim 1/a^2$ in the regime where inter-ion spacing a is much larger than the wavelength of radiation. In addition, the exact value of P^*_{AQM} will depend on the magnetic field (quantization axis) configuration.

4.4 Inter-ion scattering

Consider two ions (ion1 and ion2) (Fig. 4.2) separated by a distance a in an ion chain. For calculating the P^*_{AQM}, consider an ideal resonant laser beam illuminates ion2 without leaking any photons onto ion1. ion2 scatters photons at a rate Γ_{sc}(ion2), a portion of which are incident on ion1. The effective intensity of light on ion1 from these scattered photons

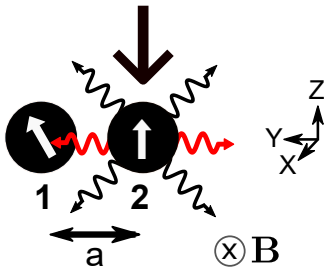

Figure 4.2: **AQM Due to Inter-Ion Light Scattering:** The red wavy lines represent the photons scattered by ion2 that are incident on ion1, causing the AQM.

is denoted by $I_{\mathrm{ab}}(\mathrm{ion1})$. The relation between $\Gamma_{\mathrm{sc}}(\mathrm{ion2})$ and $I_{\mathrm{ab}}(\mathrm{ion1})$ is given as

$$I_{\mathrm{ab}}(\mathrm{ion1}) = f_{\mathrm{pol}} f_{\mathrm{angle}} \frac{h\nu \Gamma_{\mathrm{sc}}(\mathrm{ion2})}{4\pi a^2}$$

Here, ν represents the frequency of the scattered light, f_{pol} denotes the fraction of light whose polarization affects ion1, and f_{angle} represents the angular dependence of the scattered light. When ion2 is illuminated with an ideal state-detection beam, it emits light of all polarizations. However, only the π polarization causes P^*_{AQM} in ion1. Therefore, we have $f_{\mathrm{pol}} = 1/3$. The angular dependence of light scattered in π polarization by ion2 in the direction of ion1 is given by [13]

$$f_{\mathrm{angle}} = \cos^2(\theta)$$

where θ is the angle between the magnetic field and the ion chain. In our setup, since the magnetic field is perpendicular to the ion chain((along x axis), $f_{\mathrm{angle}} = 1$. However, by choosing the magnetic field along the ion chain (along y axis), f_{angle} can be suppressed to zero. For a state-detection probe beam with an intensity of $I_2 = I_{\mathrm{sat}}$, we use the optimal scattering rate of ion2 [75] to estimate $\Gamma_{\mathrm{sc}}(\mathrm{ion2})$.

$$R_{\mathrm{o,opt}} = \left(\frac{1}{3}\right)\left(\frac{\Gamma}{2}\right)\left(\frac{s_{\mathrm{o}}}{1 + \frac{2}{3}s_{\mathrm{o}} + \left(\frac{2\Delta}{\Gamma}\right)^2}\right)$$

Here the $\Gamma = 2\pi \times 19.6$ MHz is the natural linewidth of $P_{3/2}$ manifold of $^{171}\mathrm{Yb}^+$ ion, Δ is the detuning of the probe light and $s_0 = I_2/I_{\mathrm{sat}}$ Assuming an inter ion spacing of 6 µm, we estimate that $I_{\mathrm{ab}}(\mathrm{ion1}) \approx 9.5 \times 10^{-6} I_{\mathrm{sat}}$. This results in a $P^*_{\mathrm{AQM}} = 2 \times 10^{-4}$ for 11 µs state-detection.

For a state reset operation on ion2, $f_{\text{pol}} = 2/3$ since light with both σ^+ and σ^- polarizations affect ion1. Additionally, for the case of a magnetic field perpendicular to the ion chain, we have $f_{\text{angle}} = 1/2$ [13]. We estimate that $I_{\text{ab}}(\text{ion1}) \approx 1.3 \times 10^{-6} I_{\text{sat}}$ for the state reset operation. This results in a $P^*_{\text{AQM}} = 1 \times 10^{-5}$ for state reset.

4.5 Numerical estimations of AQMs

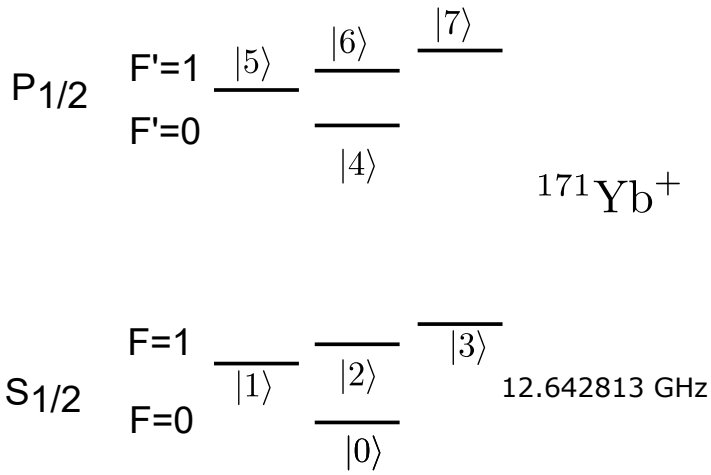

Figure 4.3: **Eight-Level Schematic for $^{171}\text{Yb}^+$ Ions:** This diagram illustrates the encoding we use for four levels in the $S_{1/2}$ and four levels in the $P_{1/2}$ manifolds.

Despite designating the ground state hyperfine levels of ytterbium ions ($S_{1/2}\,|F = 0, m_F = 0\rangle$ and $S_{1/2}\,|F = 1, m_F = 0\rangle$) with $|{\downarrow_z}\rangle$ and $|{\uparrow_z}\rangle$ of an effective spin-1/2 particle, the measurement and reset processes involve additional states. Consequently, the ions may ultimately occupy the states $S_{1/2}\,|F = 1, m_F = -1\rangle$ and $S_{1/2}\,|F = 1, m_F = 1\rangle$ outside the Hilbert space of the qubit.

To model the dynamics of the ion pertaining to this work, we account for eight levels in our Hilbert space: four for $S_{1/2}$ and four for $P_{1/2}$ (Fig. 4.3). The process of state detection mixes the ion in state $|2\rangle$ with states $|1\rangle$ and $|3\rangle$, and with $|0\rangle$ when off-resonant excitation to $P_{1/2}\,|F = 1\rangle$ states is included. The process of state reset mixes the ion in state $|2\rangle$ with

states $|0\rangle$, $|1\rangle$, and $|3\rangle$. The microwave field used in the Ramsey measurements (described later in the chapter) only couples the levels $|2\rangle$ and $|0\rangle$.

The Hamiltonian, describing the interaction with radiation, accounts for couplings due to optical pumping, state detection, and the microwave. For the purpose of efficient numerical simulations, it is useful to remove the time dependence through a rotating transform ($U(t)$) [25] such that $H_{\text{rot}} = UHU^\dagger - U\frac{d}{dt}U^\dagger$. We find that when the optical pumping, detection, and microwave couplings are monochromatic, the solution of U exists, and we use this to remove the time dependence from our total Hamiltonian. In the rotating frame, the Hamiltonian of the atom, denoted as H_{atom} (excluding any effects from detection or optical pumping light), is determined by the diagonal terms of the Hamiltonian H_{rot} as follows:

$$\begin{aligned} H_{\text{atom}} = -(\Delta_{uw} + \Delta_{szm})\,|1\rangle\langle 1| - \\ \Delta_{uw}\,|2\rangle\langle 2| - \\ (\Delta_{uw} - \Delta_{szm})\,|3\rangle\langle 3| - \\ \Delta_{uw}\,|4\rangle\langle 4| - \\ (\Delta_{uw} + \Delta_{pzm})\,|5\rangle\langle 5| - \\ \Delta_{uw}\,|6\rangle\langle 6| - \\ (\Delta_{uw} - \Delta_{pzm})\,|7\rangle\langle 7| \end{aligned} \tag{4.2}$$

Here, Δ_{uw} is the detuning of the applied microwave, Δ_{szm} is the Zeeman splitting in $S_{1/2}$, and Δ_{pzm} is the Zeeman splitting in the $P_{1/2}$ manifold, respectively. In addition to H_{atom}, the Hamiltonian H_{rot} includes time-independent off-diagonal coupling terms arising from either optical pumping or detection light. The magnitude of these coupling terms is the Rabi frequencies, which depend on the intensities and polarization of the incident resonant beams driving the respective transitions.

With the time dependence of the Hamiltonian accounted for, the time evolution of the density matrix can be determined by numerically solving the Lindblad master equation with appropriate coupling terms from the state detection or optical pumping light and collapse operators due to the spontaneous emission:

$$\begin{aligned} \dot{\rho}(t) = &-\frac{i}{\hbar}[H_{rot}, \rho(t)] \\ &+ \sum_n \frac{1}{2}\left[2C_n\rho(t)C_n^\dagger - \rho(t)C_n^\dagger C_n - C_n^\dagger C_n\rho(t)\right] \end{aligned} \tag{4.3}$$

We use the built-in master equation solver in the Python package QuTiP [47] to solve the above system. For a given intensity of resonant light on the asset qubit (I_1), the fidelity after the operation can be extracted from the above equation, and hence we can extract P_{AQM}. Now that we understood how to estimate the P_{AQM} numerically, let us understand how the intensity crosstalk I_X affects the P_{AQM}

4.6 Current techniques to minimize AQMs

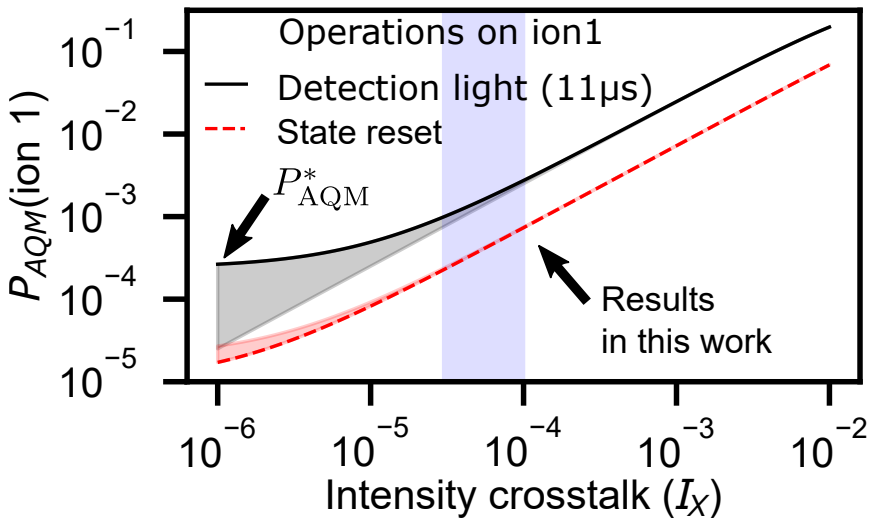

Figure 4.4: P_{AQM} **as a Function of** I_X**:** The accidental quantum measurement probability (P_{AQM}) is determined by assessing the infidelity of the asset qubit after conducting a state detection or reset operation on the process qubit. The black trace illustrates this dependency when state detection light is applied to the process qubit, while the red trace represents the scenario for state reset. The shaded regions denote potential variations arising from varying geometric properties of the system.

To investigate the impact of intensity crosstalk (I_X) on accidental quantum measurements, Figure 4.4 presents the calculated probability of AQM (P_{AQM}) for the asset qubit (ion1) as a function of intensity crosstalk (I_X). Here, P_{AQM} is estimated from the asset qubit's infidelity after a state detection or reset on the process qubit. The fidelity [74] is estimated with respect to $|\uparrow_z\rangle$ to represent the worst-case scenario. For this figure, we choose $a = 6$ μm, and $I_2 = I_{\mathrm{sat}}$ (the saturation intensity of the transition). For low crosstalk regime

($I_X < 1\times10^{-5}$), inter-ion scattering sets a fundamental limit, P^*_{AQM}, which can vary (shaded region) depending on the geometric properties of the system, such as the orientation of the magnetic field ($\vec{B}$) defining the quantization axis as discussed above. The figure clearly shows that even an intensity crosstalk of 1% can lead to high probabilities of AQMs. To achieve an error P_{AQM} below 0.5% [63], one needs to operate in the regime of intensity crosstalk I_X between 1×10^{-4} and 1×10^{-5}. Despite the capabilities of commercially available high numerical aperture optics to produce tightly focused beam spots with beam waists on the order of 1 μm for 369 nm light, this does not guarantee low light intensity in the locations of other ions in the chain. The occurrence of high AQM rates in existing implementations is attributed to the leaked light at those specific locations. This leakage is a consequence of optical imperfections in the optics, leading to optical aberrations. The optimization of optic performance often focuses on generating the desired profile, such as a beam with a Gaussian profile, rather than minimizing the background intensity.

To mitigate the high probability of AQM in current experiments, various strategies are implemented. One strategy is the physical separation of atoms through shuttling them away from each other [18, 82, 111, 107]. In this approach, ions are moved away from each other by changing the potential of the trap using a large number of electrodes, resulting in equilibrium positions of the ions being 100-200 μm apart. Once the ions are sufficiently separated, where the leaked light from the addressing probe beam is low, the target ion is measured or reset. Subsequently, the ions are brought back closer to each other to continue the quantum algorithm. However, this strategy requires complicated traps with hundreds of electrodes for the shuttling operation and introduces motional heating, which can limit the possibilities of the quantum algorithm being performed.

Another commonly used strategy is the usage of additional ancilla qubits of the same species [76] or different atomic species [72, 11, 40, 96]. Some experiments employ ancilla ions that are entangled with the target ions to perform mid-circuit measurements and resets. However, this approach wastes one ancilla qubit per measurement/reset, which is resource-intensive in platforms where the number of qubits is valuable. Additionally, if atoms of other species are used, the optical layout of the system becomes complex, requiring the management of laser beams for multiple qubits.

Another strategy is shelving or hiding qubits to states outside the computational Hilbert space [86, 62, 38, 90, 61]. However, this strategy also introduces complexities, such as the need for additional lasers, and requires performing shelving operations on all remaining subsystems every time a subsystem needs to be measured. Errors from multiple shelving operations accumulate faster and add decoherence to the system. Other indirect suppression techniques, such as micromotion hiding [28], face similar challenges of complexity and motional heating as the above techniques. In summary, these techniques waste resources

(circuit time, extra qubits) and introduce additional errors (e.g., errors due to motional heating or imperfect coherent operations).

4.7 Compensating the optical aberrations

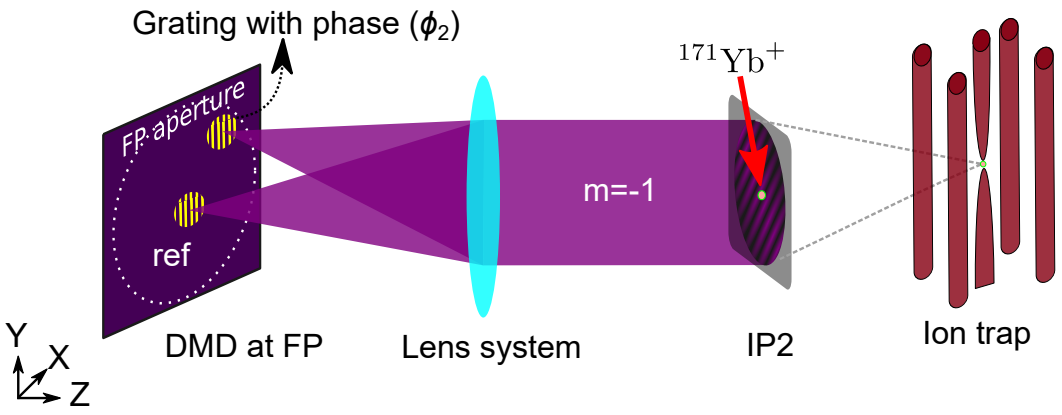

Figure 4.5: **Optical Schematic for Measuring Aberration Profile:** The optical setup illustrates the measurement of aberration profiles [93]. Light diffracted from two grating patches on the Digital Micromirror Device (DMD) illuminates a single $^{171}Yb^+$ ion trapped within the four-rod ion trap. The ion is used to detect and analyze the interference pattern produced by the light diffracted from the grating patches.

Instead of the indirect techniques presented above to mitigate the effects of intensity crosstalk, we decided to directly tackle the optical aberrations and compensate them. The optical aberrations in the entire optical system could be characterized by a single phase profile in the Fourier plane [93]. And if we could measure such phase profile and somehow compensate it, we can negate the effects of the optical aberrations. This is where the holographic beam shaping presented in the previous chapter comes handy. As we can see from the form of the profile, we program onto the DMD characterized by the grating equation (Eqn. 3.1), we can compensate for both the input phase profile and the intensity profile in the final beam profile on the ion. This is possible as long as we can characterize the phase profile and intensity profile with good accuracy.

We characterize the optical aberrations along the entire beam path in terms of a Fourier plane (FP) phase map. The optical aberrations from the input plane IP1 ($\Phi_{ab}^{(0)} + \Phi_{ab}^{(1)}$) are

characterized using camera C1 as a sensor, measuring the relative optical phase between two FP "patches" [93]. The optical aberrations from IP1 to IP2 ($\Phi_{ab}^{(0)}$) are measured using a single ion as a sensor. The relative optical phase between two FP "patches" is obtained by observing the interference of beams diffracted from these patches(Fig.4.5). To measure this interference signal, we utilize a single ion as a quantum sensor. The ion is subjected to an optical pumping beam, initially prepared in state $|\uparrow_z\rangle$, and the state-dependent fluorescence signal is observed as it is pumped into state $|\downarrow_z\rangle$. By varying the phase of one of the FP patches and monitoring the ion fluorescence for a fixed optical pumping time, we extract the interference profile and thereby determine the relative phase. This approach is highly sensitive, requiring only a few photons for optical pumping, enabling us to map out the phase diagram for the entire FP using very low optical power (around 200 µW of 369 nm light). By separating the probing and measurement processes, we achieve a higher signal-to-noise ratio compared to our previous method [93], where unwanted scattering of the probe beam from optics leaked onto the detector and acted as a limiting factor. The phase profile $\Phi_{ab}^{(0)} + \Phi_{ab}^{(1)} + \Phi_{ab}^{(2)}$ is then employed to compensate for the optical aberrations using an iterative Fourier transform algorithm (IFTA) [93], resulting in the creation of a diffraction-limited Gaussian beam spot in IP2.

The incident light on the DMD from L1 exhibits nonuniformity and follows a Gaussian intensity profile. Additionally, the pellicle beam splitter (PB) introduces angular dependence on reflection. To measure the effective intensity profile on the Fourier plane (FP), an ion in IP2 serves as a sensor.

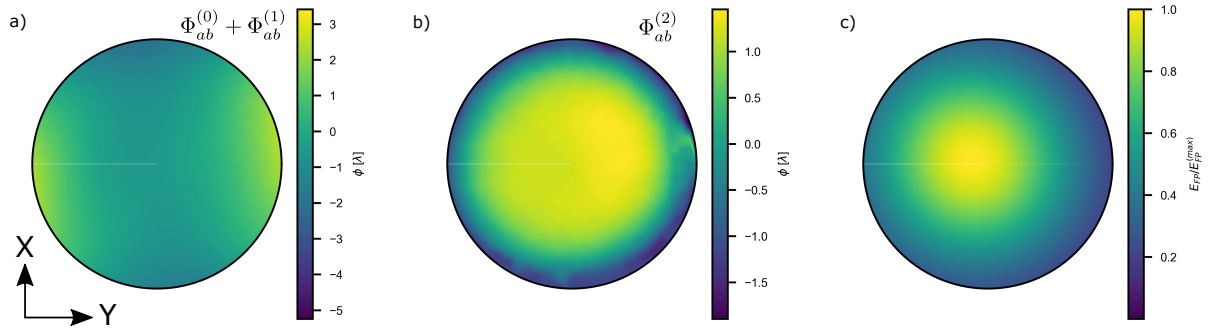

Figure 4.6: **FP phase and amplitude profile:** a)The aberration phase profile measured using camera C1. b) The aberration phase profile is measured using the ion at IP2. For a-b, the piston and tilt terms are removed from the measured phase profiles, and the profile is further smoothened and interpolated. c) The scaled amplitude profile measured at IP2. The measured amplitude profile is smoothened, interpolated, and fit to 2D Gaussian.

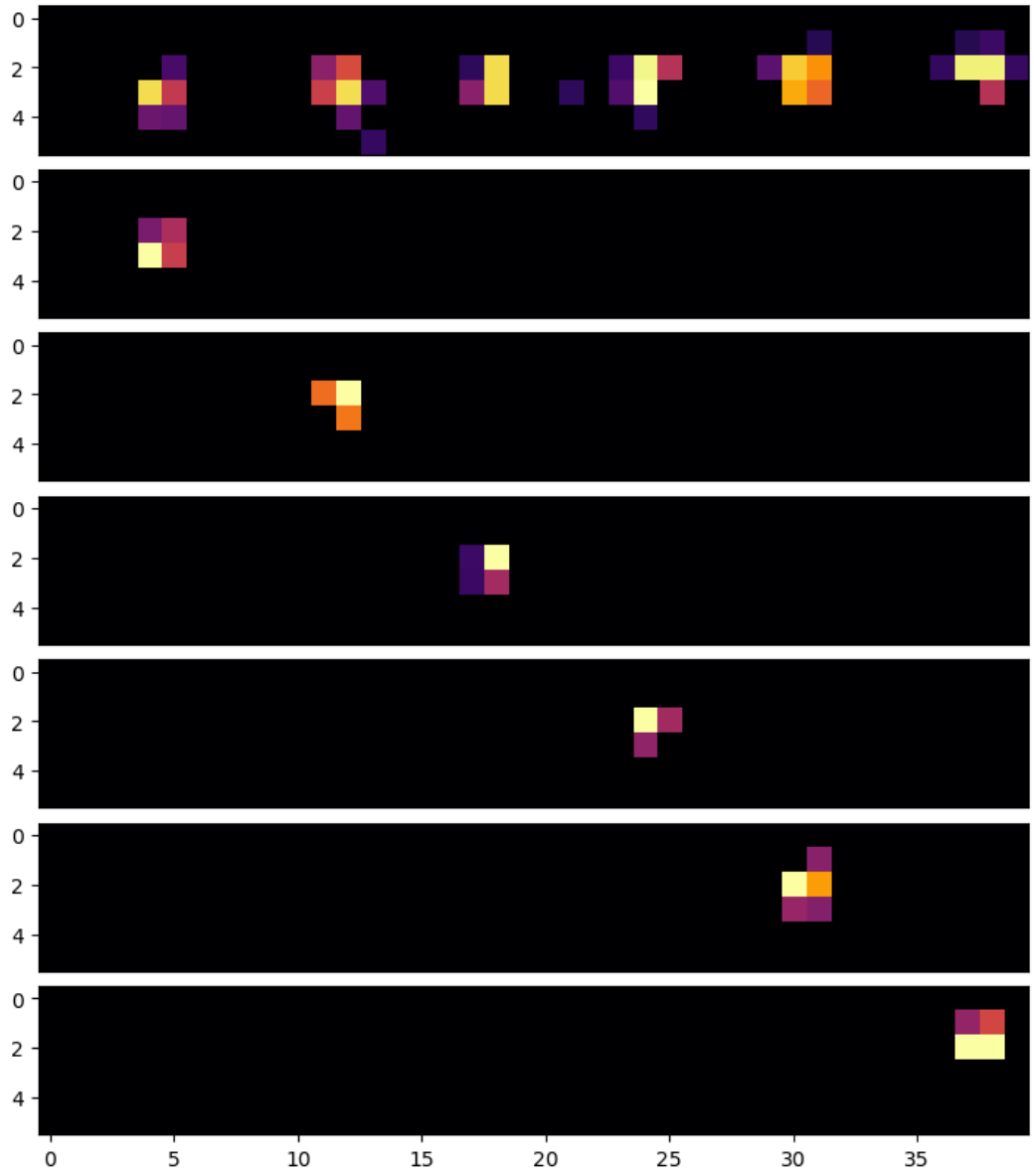

Figure 4.7: **Individual Addressing of 6-Ion Chain:** Sequence of images demonstrating individual addressing in a chain of 6 ions. The first image shows all ions in the $|\uparrow_z\rangle$ state, while the subsequent images showcase site-selective reset, with only one ion prepared in the $|\uparrow_z\rangle$ state while the others remain in the $|\downarrow_z\rangle$ state.

The ion is initially prepared in the $|2\rangle$ state, and the optical pumping light emitted by the DMD is used to pump it to the $|0\rangle$ state for a fixed duration. By observing the decrease in ion fluorescence, the intensity of the probe light reflected by a circular patch (with a diameter of 30 pixels) on the DMD can be inferred. This measurement is repeated for various phase-corrected patches on the DMD, allowing the construction of an effective intensity profile.

To obtain a smooth and interpolated intensity profile, the measured data is smoothened and interpolated. The square root of the intensity profile is then used as the amplitude profile for the incident electric field. This amplitude profile serves as input to the iterative Fourier transform algorithm (IFTA) hologram generation algorithm [93], facilitating the generation of holograms.

Once the aberration profile is measured and the input intensity profile is calibrated, we can generate a Gaussian beam with a beam waist of $1.5\mu m$ in the ion plane, focusing onto the desired ion. In Fig. 4.7, a sequence of images taken from a chain of 6 ions is presented. The first image corresponds to all ions being in the $|\uparrow_z\rangle$ state, while the subsequent images show individual ions prepared in the $|\uparrow_z\rangle$ state using site-selective reset, while the others remain in the $|\downarrow_z\rangle$ state. This sequence demonstrates the effectiveness of our scheme in achieving individual addressing of ions.

However, despite achieving individual addressing, it is necessary to characterize the AQMs that may occur on the other ions. The images shown above have limited dynamic range, making it challenging to measure low errors accurately. To characterize these errors to a level below 0.1%, we need to develop a measurement technique with a higher dynamic range. This technique would enable us to measure and quantify the errors with improved accuracy and precision. We also need to be able to connect the characterization technique to the fidelity metric so that we can extract the efficacy our technique in preserving the state of the asset qubit.

4.8 Ramsey interferometry

We use a set of Ramsey measurements to characterize the P_{AQM} caused by the probe beam parked at a distance d from ion-1 (Fig. 4.8b).

Each set of measurements is initialized by a sequence of Doppler cooling for 2.5 ms, followed by global optical pumping to prepare the ions in the $|\downarrow_z\rangle$ ($|0\rangle$) state for 20 μs. The

probe light is then illuminated for a time T between two microwave $\pi/2$ pulses, which are detuned from the transition $|\downarrow_z\rangle$ to $|\uparrow_z\rangle$ by $\Delta_{uw} = 2\pi \times 10$ kHz. The duration of each pulse is approximately 6 μs. A detection step follows, where the ions are illuminated by a global detection beam for 1.5 ms, during which the state-dependent fluorescence from the ions is collected using a photomultiplier tube (PMT). Each experiment is repeated 200 times, and the PMT counts are averaged over these repetitions. The averaged PMT counts are then normalized using the measured counts obtained from preparing the $|\downarrow_z\rangle$ and $|\uparrow_z\rangle$ states. The normalized fluorescence, denoted as $\approx P(|\uparrow\rangle)$, exhibits oscillations at a frequency of 10 kHz as the time T is varied. The contrast of these oscillations is represented by $R_c(T)$. To extract the characteristic decay time (T_2^*) of the Ramsey contrast $R_c(T)$ for a given configuration of d, Ramsey measurements are performed with varying T (Fig. 4.8b). A preliminary coarse estimate of T_2^* is obtained, and the time interval between 10 μs and $2T_2^*$ is divided into five intervals, each containing 21 data points over a span of 200 μs.

After conducting the Ramsey measurements for these five intervals, the PMT counts are analyzed using the following function to extract the value of T_2^*:

$$f(T)_{T_2^*,\alpha,\beta,\phi,C} = \sin^2(\omega T + \phi)(\alpha e^{-T/T_2^*}) + \beta(1 - e^{-T/T_2^*}) + C \tag{4.4}$$

As a baseline measurement, Ramsey measurements are also performed with no probe beam during the wait time (Fig. 4.8a), and it is estimated that T_2^* is much larger than 200 ms. The long quantum memory of the asset qubit (T_2^* without any probe light is at least two orders of magnitude longer) enables it to act as a sensitive, high-dynamic range sensor for intensity crosstalk. The data presented in Fig. 4.8b correspond to a single ion ($N = 1$) illuminated with the state-detection probe light ($I = 1.25(16)I_{\text{sat}}$, waist $w = 1.50(5)$ µm) at a distance of $d = 6.0(3)w = 9.0(4)$ µm, with a Ramsey detuning of 10 kHz. The error bars indicate the standard error from 200 experimental repetitions. The intensity crosstalk I_X is estimated using numerical simulations of the master equation based on the measured T_2^*. From these simulations (described above), we find that the intensity crosstalk is $I_X = 3.4(6) \times 10^{-5}$ for this data. In the following section, we utilize the Ramsey interferometric measurements to extract the fidelity of preserving the asset qubit.

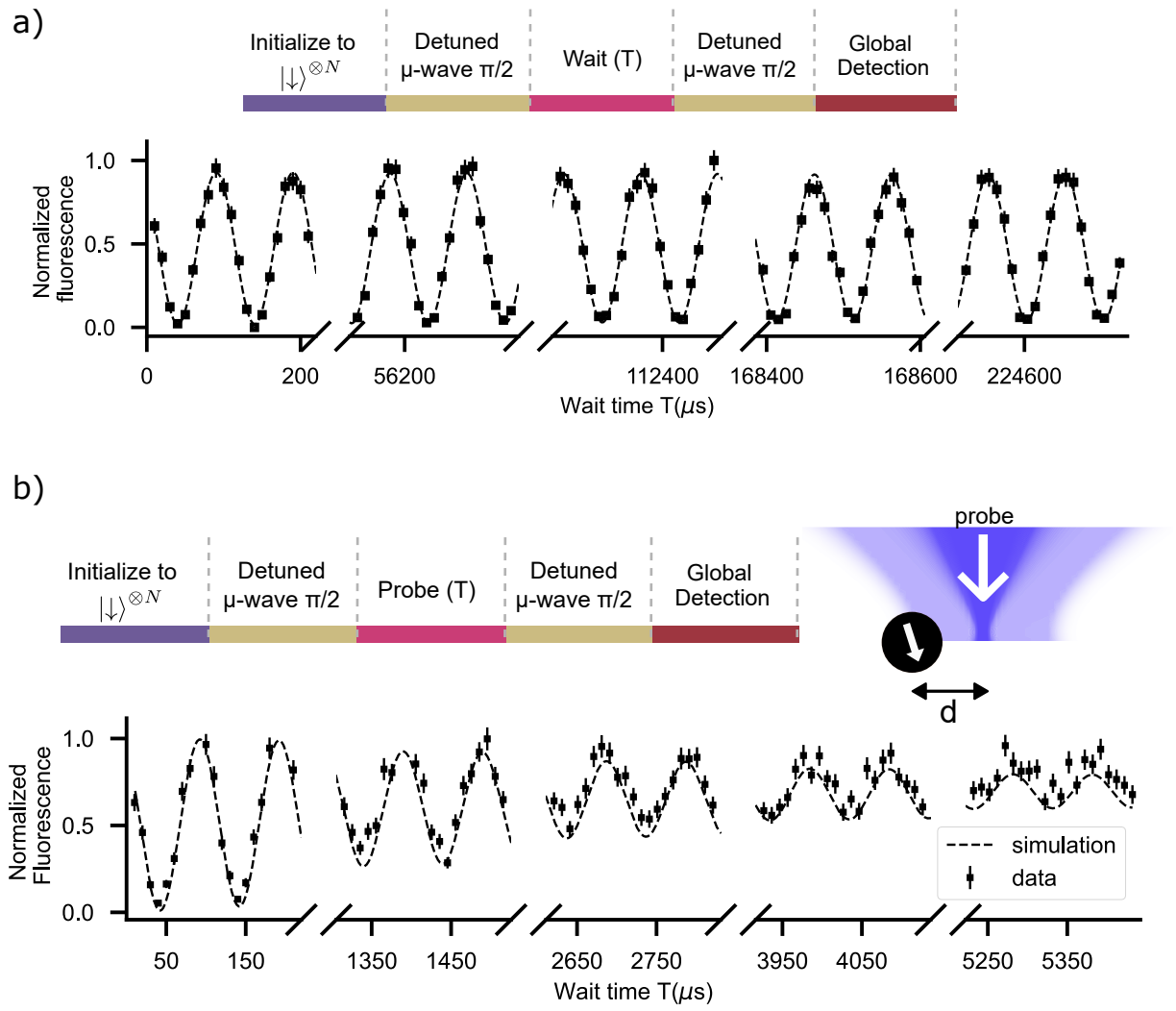

Figure 4.8: **Ramsey Measurements:** Oscillations in the normalized fluorescence during off-resonant Ramsey measurements with (b) and without (a) probe light during the wait time. Here, N denotes the number of ions; for these measurements, it is $N = 1$.

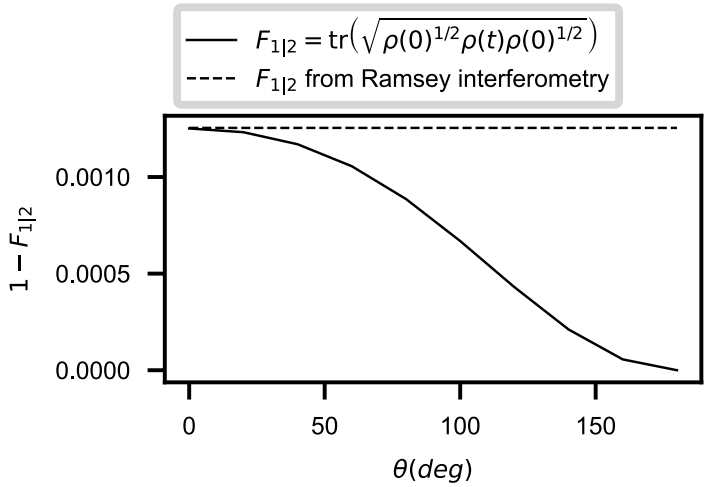

Figure 4.9: **Infidelity (1-$F_{1|2}$) as a Function of Bloch Angle θ:** Here the ion-1 is initialized in state $\rho(0) = |\psi\rangle\langle\psi|$ where $|\psi\rangle = \cos(\theta/2)|2\rangle + \sin(\theta/2)|0\rangle$. The $F_{1|2}$ (Eq. 4.5) is measured after a weak state-detection ($D_1^{(10)}$) light of intensity $I = 5 \times 10^{-5} I_{\mathrm{sat}}$ and polarization $I_\pi/I = \frac{1}{3}$ is applied on ion-1 for $11\mu s$. For comparison, the infidelity $(1 - F_{1|2})$is shown(dotted line) from Ramsey interferometry(Sec. 4.8) where a probe light of similar parameters as above is illuminated on ion-1 during the wait time.

4.9 Fidelity estimation

To quantify how well the quantum state of asset qubit is preserved after an operation on the process qubit, we use the fidelity metric ($F_{1|2}$) [74] defined as

$$F_{1|2}(t) = \mathrm{tr}\left(\sqrt{\rho(0)^{1/2}\rho(t)\rho(0)^{1/2}}\right) \tag{4.5}$$

where $\rho(0)$ and $\rho(t)$ denote density matrix operators of ion-1 (assuming unentangled with ion-2) before and after a state-reset or measurement operation (performed for time t) on ion-2, respectively. This metric yields a different value based on the initial state of ion-1, and using numerical simulations described above, we find that $\rho(0) = |2\rangle\langle 2|$ represents the worst case scenario (Fig. 4.9).

By analytically solving the master equation of the system we find that the Ramsey fringe contrast $R_c(T)$ could be used to estimate the worst-case fidelity of ion-1 after an

operation ion-2 for a time (T) using

$$F_{1|2}(T) = \frac{2}{3}R_c(T) + \frac{1}{3} \tag{4.6}$$

To derive the above expression analytically, we assume that the intensity of probe light decohering the ion-1 is very weak, that it causes a low probability of accidental measurement $P_{\text{AQM}} \ll 1$. In this limit, consider the density matrix of ion-1 in a reduced Hilbert space with only $(|0\rangle, |1\rangle, |2\rangle, |3\rangle)$ states. We model the action of probe light using the collapse operators $C_n = \sqrt{\gamma_n}\,|i\rangle\langle j|$ where $i, j \in \{0, 1, 2, 3\}$ where γ_n is the rate of collapse. The collapse operators and their rates depend on the transition the probe is driving and its polarization. For example, in state detection, only the probe with π polarization causes the AQM of ion-1. In the limit $P_{\text{AQM}} \ll 1$ with $\gamma \ll 1$ representing the rate of P_{AQM} we use the following collapse operators

Transition	Polarization	Collapse operators
$D_1^{(10)}$	π	$\sqrt{\frac{\gamma}{3}}\,\|2\rangle\langle 2\|$, $\sqrt{\frac{\gamma}{3}}\,\|1\rangle\langle 2\|$, $\sqrt{\frac{\gamma}{3}}\,\|3\rangle\langle 2\|$
$D_1^{(11)}$	σ^+	$\sqrt{\frac{\gamma}{3}}\,\|2\rangle\langle 2\|$, $\sqrt{\frac{\gamma}{3}}\,\|3\rangle\langle 2\|$, $\sqrt{\frac{\gamma}{3}}\,\|0\rangle\langle 2\|$
$D_1^{(11)}$	σ^-	$\sqrt{\frac{\gamma}{3}}\,\|2\rangle\langle 2\|$, $\sqrt{\frac{\gamma}{3}}\,\|1\rangle\langle 2\|$, $\sqrt{\frac{\gamma}{3}}\,\|0\rangle\langle 2\|$

For ion-1 initialized in $\rho(0) = |2\rangle\langle 2|$ state, the final state of the ion-1 after the AQM due to weak probe for a time t is calculated by analytically solving the Lindblad master equation

$$\begin{aligned}\dot{\rho}(t) = &-\frac{i}{\hbar}[H_{atom}, \rho(t)] \\ &+ \sum_n \frac{1}{2}\left[2C_n\rho(t)C_n^\dagger - \rho(t)C_n^\dagger C_n - C_n^\dagger C_n\rho(t)\right]\end{aligned} \tag{4.7}$$

Here, H_{atom} in interaction picture is given by

$$H_{atom} = -(\Delta_{uw} + \Delta_{zm})\,|1\rangle\langle 1| - \Delta_{uw}\,|2\rangle\langle 2| - (\Delta_{uw} - \Delta_{zm})\,|3\rangle\langle 3|$$

Here Δ_{uw}, Δ_{zm} denote the detuning of the microwave field and Zeeman splitting, respectively. From the solution, we find the fidelity $F_{1|2}$ to be

$$F_{1|2}(t) = \sqrt{\rho_{22}(t)} = e^{-\frac{1}{3}\gamma t} \approx 1 - \frac{1}{3}\gamma t \tag{4.8}$$

Similarly, after the Ramsey experiment (Sec. 4.8), the normalized is given as

$$\rho_{22}(t) = \frac{1}{4} + \frac{1}{4}e^{-1/2\gamma t - i\Delta_{uw}t} + \frac{1}{4}e^{-1/2\gamma t + i\Delta_{uw}t} + \frac{1}{4}e^{-2/3\gamma t} \tag{4.9}$$

The Ramsey fringe contrast is then given by $R_c(T) = \rho_{22}\left(\frac{(2m+1)\pi}{\Delta_{uw}}\right) - \rho_{22}\left(\frac{2m\pi}{\Delta_{uw}}\right)$ for a positive integer m and assuming $\gamma \ll \Delta_{uw}$ we get

$$R_c(T) \approx e^{-\frac{1}{2}\gamma t} \approx 1 - \frac{1}{2}\gamma t \tag{4.10}$$

Combining Eq. 4.8 and 4.10 we get 4.6. Further, the Ramsey fringe decays exponentially with a characteristic time T_2^* which leads to

$$F_{1|2}(T) = \frac{2}{3}e^{-(T/T_2^*)} + \frac{1}{3} \tag{4.11}$$

In the regime where the probability of the asset qubit accidentally scattering a photon, $P_{\mathrm{AQM}} \ll 1$, we find numerically that the infidelity of the asset qubit is a good estimate of P_{AQM}. Thus, the fidelity [74] of preserving the state of asset qubit is estimated from fringe contrast in a Ramsey interferometry experiment. We measure the fringe decay (decoherence) time T_2^* of the asset qubit(ion1) and estimate the fidelity of preserving its state after measurement or reset on the process qubit (ion2) from,

$$F_{1|2} = \frac{2}{3}\exp\left[-\frac{\tau(\mathrm{ion2})}{T_2^*(\mathrm{ion1})}\right] + \frac{1}{3}. \tag{4.12}$$

Here, τ(ion2) is the time for which the resonant probe beam illuminates the process qubit. From the measured T_2^*, we estimate the intensity of probe light sampled by the asset qubit.

4.10 Calibrations

Before characterizing and quantifying the AQMs in our addressing scheme, it is essential to calibrate and quantify the entire system. This calibration process involves determining the delivered intensity to the ion relative to the saturation intensity and understanding the polarization of the probe beam in relation to the quantization axis established by the magnetic field. To achieve this, we conduct a comprehensive set of calibrations and fit the calibration data using atomic physics calculations presented in the previous sections. By employing these calculations, we can extract the absolute intensity and polarization of the probe beam accurately. Performing these calibrations and obtaining precise measurements of the intensity and polarization is crucial in accurately quantifying the AQMs in our addressing scheme. These calibrations provide us with the necessary information to establish a baseline for understanding the system's behavior and correctly assessing the effects of AQMs on the ion's state.

4.10.1 Relative intensity calibration

The intensity of the probe light illuminating the ion through DMD is controlled by adjusting the RF power of the AOM1(Fig. 3.6). The RF power vs. intensity of the light is calibrated using camera C1(Fig. 3.6). To ensure accurate reporting, the linearity of C1's exposure time is confirmed over four orders of magnitude from 100 μs to 5 s (Fig. 4.10). The linearity of the RF source power setting and the RF power output is calibrated using a spectrum analyzer. The pellicle placed after the IP1 has a polarization-dependent transmission profile that is calibrated using camera C2 and compensated using the AOM. This calibration also gives a relative measurement connecting the attenuated and unattenuated probe beam intensity through the camera's exposure time and pixel intensity (at a fixed gain).

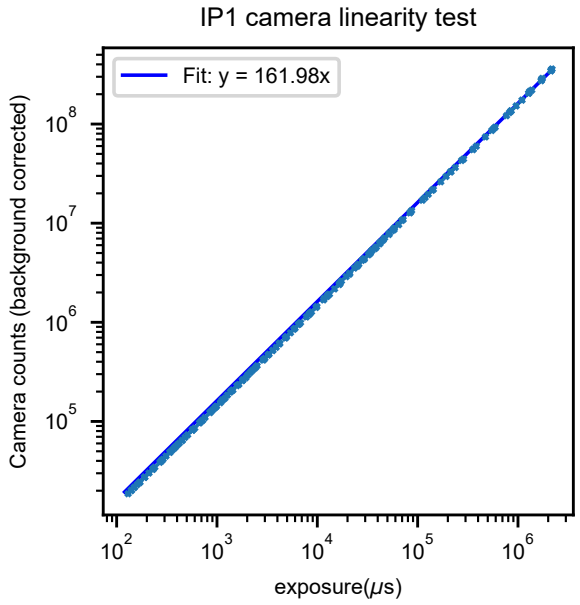

Figure 4.10: **C1 Camera Linearity Calibration:** Camera counts, corrected for background, are measured as the camera's exposure is increased. Since the camera does not have a large dynamic range, the incident light used varies, with measurements taken within the dynamic range of the camera. All the data is then stitched together to obtain the plot above.

4.10.2 Absolute intensity and polarization calibration

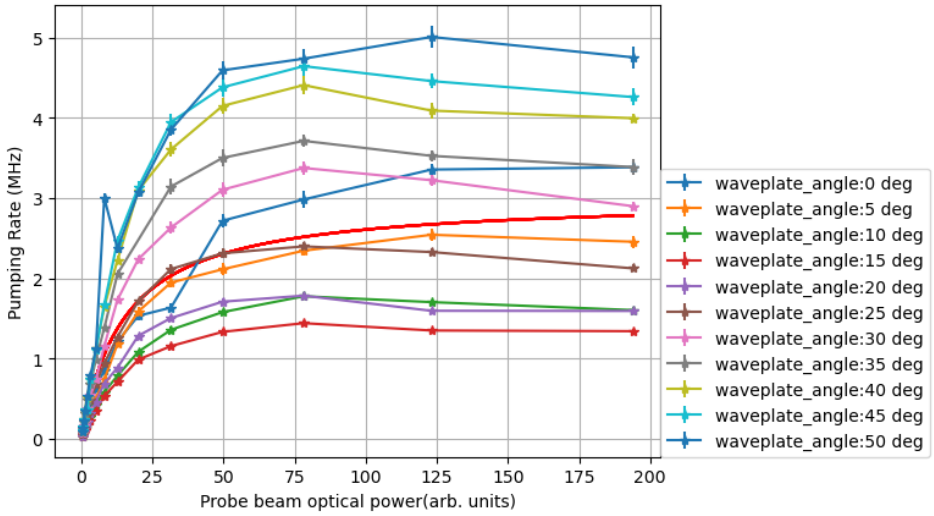

Figure 4.11: **Optical Pumping Rate as a Function of Probe Beam Power and Polarization:** Series of optical pumping experiments were conducted using a single $^{171}Yb^{+}$ ion while varying the optical pumping beam power and the angle of the $\lambda/2$ waveplate to adjust polarization. The pumping rate is defined with respect to the pumping time, which is the duration at which the fluorescence of the ion decreases to 1/e relative to the maximum fluorescence.

The intensity of the probe beam, which is calibrated using camera C1, is further calibrated with respect to the saturation intensity (I_{sat}) of the ion. This calibration process involves conducting a series of optical pumping experiments using the probe beam, while varying both the calibrated power and the input polarization by adjusting the angle of the $\lambda/2$ waveplate (WP).

In each optical pumping experiment, the pumping rates are extracted by fitting the experimental data with an appropriate exponential curve. These pumping rates, obtained as a function of the waveplate angle and the optical power (calibrated using the camera), are shown in Fig. 4.11.

To accurately determine the absolute intensity and polarization of the light illuminating the ion, the experimental data is fit using numerical simulations. By comparing the

experimental results with the simulated data, we can extract the precise values for the absolute intensity and polarization of the light incident on the ion.

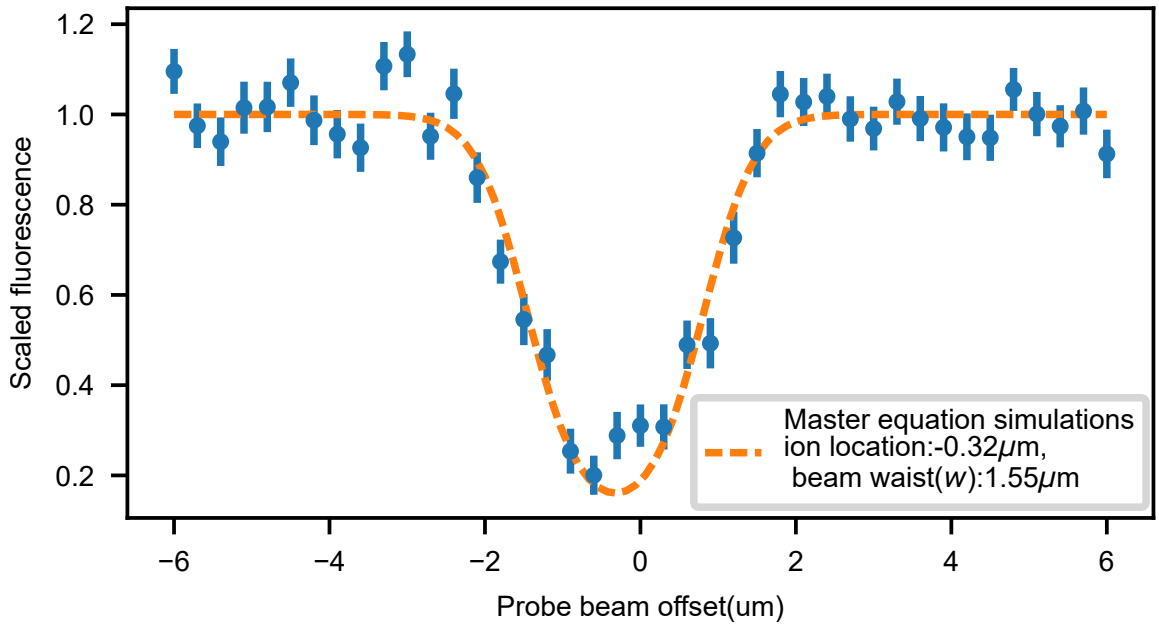

Figure 4.12: **Probe Beam Position and Size Calibration:** This experiment involves measuring the scaled fluorescence emitted by a single $^{171}Yb^{+}$ ion while steering the probe beam within the ion plane. The fluorescence is measured after applying the optical pumping probe beam for a fixed duration of time. Subsequently, the acquired signal is fitted using fluorescence data obtained from full master equation simulations with a Gaussian probe beam to determine the beam waist and the ion's position.

4.10.3 Probe beam position and size calibration

The calibration of the probe beam's position and beam waist involves using a single ion as an intensity sensor. The ion is initially prepared in state $|2\rangle$, and a probe beam, designed to reset the ion's state, illuminates it for a duration shorter than the optical pumping time. Subsequently, a state measurement is performed. The fluorescence of the ion is studied as a function of the beam position, enabling the determination of the relative beam position and the beam waist (Fig. 4.12). To change the position of the probe beam, a shifted Gaus-

sian beam is generated by programming the hologram on the Digital Micromirror Device (DMD). This calibration procedure is conducted regularly before each set of experiments to compensate for the gradual drift in the relative position of the beam with respect to the ion. Our measurements indicate that the probe beam drifts by approximately 0.20(15) µm over a 15-minute period, which corresponds to a single Ramsey measurement.

4.10.4 Length scale calibration

The effective focal length of the imaging system, which is approximately 24mm, allows for the translation of the known length scale in the Fourier plane (FP) to the corresponding length scale in the imaging plane (IP2). To determine the relative positions of two ions in a trap, we employ a similar experimental approach as described in Section 4.10.3. By comparing the estimated relative beam positions of the two ions, we can calculate the inter-ion spacing. This calculated inter-ion spacing can then be compared to the equilibrium positions estimated from the measured trap frequencies, enabling further calibration of the imaging system's effective focal length. Through this method, we can achieve a calibration of the length scale in IP2 with an accuracy of up to 5%.

4.10.5 Frequency calibration

The relative shift of the laser frequency is calibrated by tuning the laser to the optical pumping transition and maximizing its pumping efficiency onto the ion.

Having established the methods for measuring and quantifying AQMs, as well as understanding their impact on the fidelity of preserving the asset qubit and the calibration of the system, our attention can now be directed towards optimizing various experimental parameters to minimize the impact of P_{AQM} on the asset qubits.

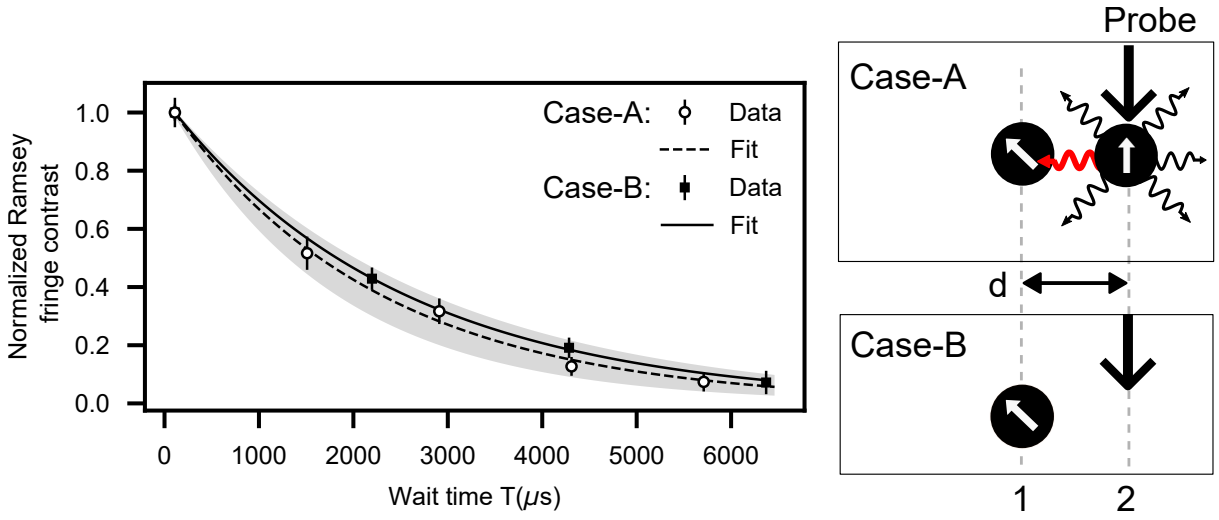

Figure 4.13: **Ramsey Fringe Contrast Decay:** This figure presents a comparison of Ramsey fringe contrast in two distinct cases, denoted as A and B. The goal is to differentiate between decoherence resulting from inter-ion scattering and imperfect optical addressing.

4.11 Measuring AQM due to inter-ion scattering

To distinguish between the decoherence caused by inter-ion scattering and imperfect optical addressing, we conducted Ramsey measurements for two different cases (Fig. 4.13). In case-A, two ions were separated by a distance d, with a probe beam parked on ion2. In case-B, only one ion was used with a probe beam parked at the same distance d from the ion. The data points in Fig. 4.13 represent the measured Ramsey fringe contrast over two fringes, and exponential decay fits were applied with T_2^* as a fitting parameter. The Ramsey fringe contrast was normalized with the contrast measured at $T \approx 0$. Error bars denote the standard deviation in estimating the Ramsey fringe contrast, obtained through 20 bootstrapping repetitions from 200 measurements. In case-A, the shaded region indicates fluctuations in the experimental settings due to periodic calibration of the probe beam location with respect to ion2. Notably, the measured T_2^* values for both case-A and case-B fall within the error bounds, indicating that decoherence is primarily limited by intensity crosstalk rather than inter-ion scattering.

Furthermore, for a distance $d = 6w$ (9 µm), we observed that the Ramsey fringe decay time (T_2^*) was indistinguishable between both experiments, considering the experimental

fluctuations. This observation provides verification that inter-ion scattering is not the major source of decoherence in our experiment. Consequently, we can simplify the measurement scheme by utilizing a single-ion configuration (case-B) to quantify the fidelity ($F_{1|2}$) in our addressing scheme.

4.11.1 Error Analysis

In the analysis performed in the plot and the subsequent analysis, the bootstrapping method was used for error analysis of the fitted parameters related to population transfer or decoherence time. This method involved randomly resampling the dataset, with replacement, for the same experimental setting. The resampled dataset was then used to extract the fitted parameters. By repeating this resampling and fitting process, an empirical distribution of the fitting parameters was obtained. In the data presented in this chapter, the dataset was resampled 20 times, and the standard deviation of the 20 fitting parameters from the resampled datasets was used as the error estimation. With the error values obtained for τ(ion2) and T_2^*(ion1) through bootstrapping, the error of estimating fidelity can be calculated using error propagation methods.

4.12 Parameter optimization for improving fidelities

The process duration τ and the decoherence time T_2^* in Eq.4.12 may have different dependence or optima over optical parameters (such as polarizations, spectral purity, etc.). In the following experiments, we maximize $F_{1|2}$ by maximizing the fraction of light contributing to the process (state reset or measurement) while minimizing (where possible) the fraction of light that accidentally measures the asset qubit.

4.12.1 Site-selective state reset

The process of state reset through optical pumping is done by using a probe that drives the transition $D_1^{(11)}$ from $S_{1/2}\,|F=1\rangle$ to $P_{1/2}\,|F'=1\rangle$ [77] (Chapter 2). We choose the process time τ_{op}(ion2) $= 7T_1$, where T_1 indicates the time at which the normalized ion fluorescence of ion2 drops to $1/e$ compared to its initial value. This will ideally reset the quantum state of the process qubit to $|\downarrow_z\rangle$ with the fidelity of $1 - e^{-7} = 0.999$. Note that spectral components of light apart from $D_1^{(11)}$ may decohere the asset qubit while not contributing to the reset on the process qubit (ion2). For example, optical pumping

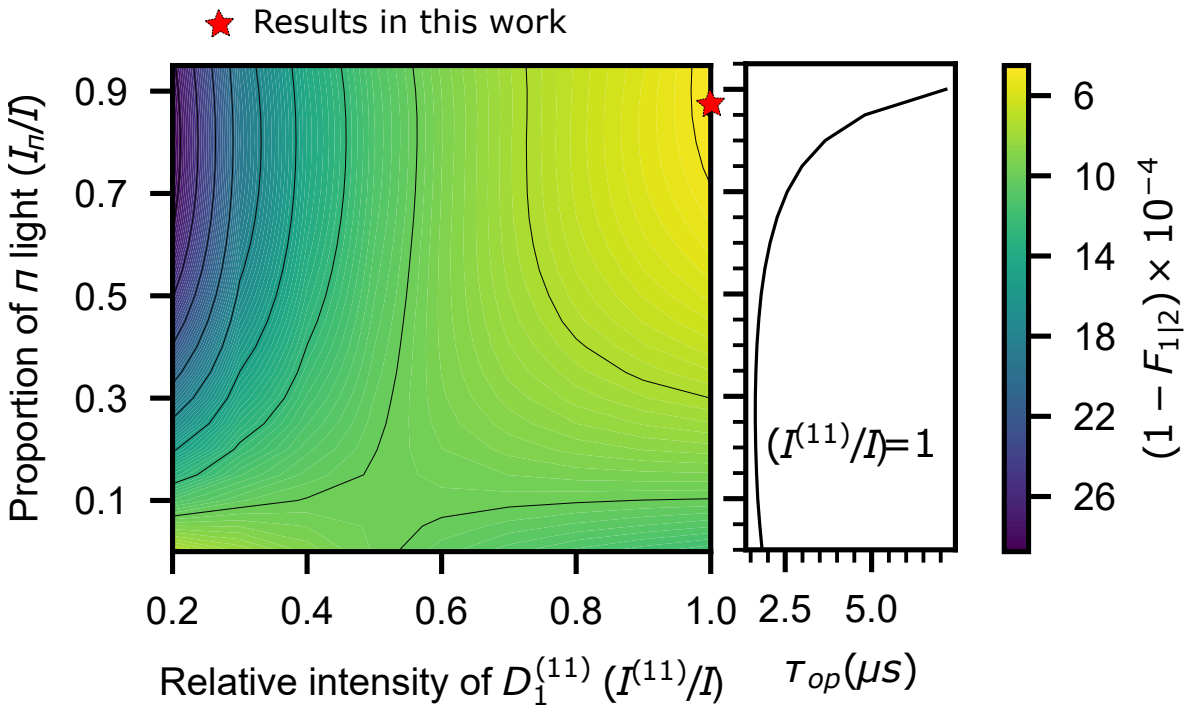

Figure 4.14: **Spectral and Polarization Dependence of $F_{1|2}$ for State Reset:** This graph displays the calculated $F_{1|2}$ as a function of the ratio of the $D_1^{(11)}$ component intensity ($I^{(11)}$) to the total intensity (I) and the ratio of π polarization intensity (I_π) to the total intensity. For comparison, the dependence of optical pumping time (τ_{op}) on polarization is illustrated on the right.

light derived by frequency modulation (electro-optic modulation) employed in typical ion trap experiments [77] contains residual $D_1^{(10)}$ component (the spectral component used for detection). This $D_1^{(10)}$ component will increase P_{AQM} and hence reduce $F_{1|2}$, as shown by numerical simulation data in Fig. 4.14 where $F_{1|2}$ is maximized for a probe with relatively higher intensity in $D_1^{(11)}$ component ($I^{(11)}$). Figure 4.14 shows the calculated $F_{1|2}$ for the state reset process as a function of the ratio of the intensity of $D_1^{(11)}$ component $I^{(11)}$ to the total intensity I (where $I = I^{(11)} + I^{(10)}$ with $I^{(10)}$ indicating $D_1^{(10)}$ component) and ratio of the intensity of π polarization I_π to the total intensity I (where $I = I_\pi + I_{\sigma^+} + I_{\sigma^-}$ with equal intensities in σ^+ and σ^- polarizations). Here, $F_{1|2}$ is calculated using numerical simulations of the master equation under the conditions of $I_2 = 1.25 I_{\text{sat}}$ and $I_X = 5 \times 10^{-5}$. The red

star marker indicates the parameters used to measure $F_{1|2}$ in Fig.4.15. Additionally, the plot on the right shows an estimation of state reset times τ_{op}(ion2) as a function of I_π/I for $I^{(11)}/I = 1$.

Probe light of different polarizations has unequal contributions to the asset qubit's fidelity $F_{1|2}$ for the case of state reset. For $D_1^{(11)}$ transition, since the $|\uparrow\rangle = S_{1/2}\,|F = 1, m_F = 0\rangle$ to $P_{1/2}\,|F' = 1, m'_F = 0\rangle$ is dipole forbidden, the component with π polarization with intensity I_π does not contribute to the AQM of the asset qubit. So, for the case of probe with $I^{(11)}/I = 1$, $F_{1|2}$ increases with I_π/I (Fig. 4.14). This increase in $F_{1|2}$ comes at the cost of increasing the state reset τ_{op} of ion2. For the case of $I^{(11)}/I \neq 1$, the π polarizations of the $D_1^{(10)}$ transition component of the probe still contribute to the AQM of the asset qubit. Hence, an increase in I_π/I decreases $F_{1|2}$ as the light with π polarization only contributes to AQMs of the asset qubit but not to the reset of the process qubit.

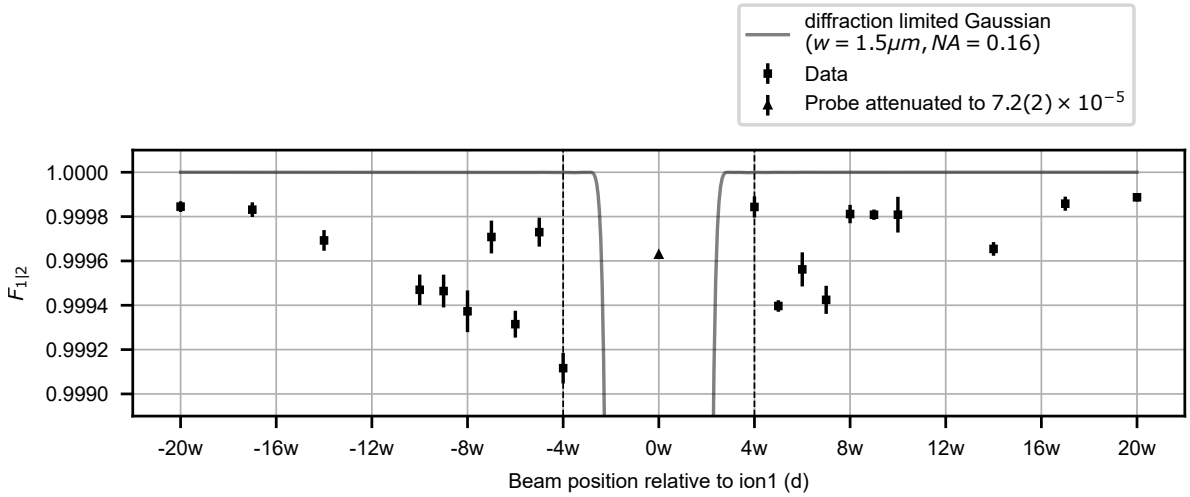

Figure 4.15: **Characterization of Fidelity ($F_{1|2}$) for State-Reset in Case-B Configuration:** The figure depicts the characterization of fidelity ($F_{1|2}$) in the Case-B configuration for state-reset as a function of the beam position relative to the ion (d) in units of the Gaussian beam waist (w).

After optimizing the polarization of the state reset beam, we proceeded to characterize the fidelity ($F_{1|2}$) in the case-B configuration as a function of the beam position relative to the ion (d). We observed $F_{2|1} > 99.90\%$ for $d \geq 4w$, where w represents the Gaussian beam waist of the addressing beam. The plot in Figure 4.15 shows $F_{1|2}$ plotted against d,

expressed in multiples of the beam waist w. The Gaussian beam waist was measured as $w = 1.50(5)$ µm. The error bars in the plot represent the standard deviation in estimating $F_{1|2}$, obtained from 20 bootstrapping repetitions performed on 200 measurements.

To calibrate the crosstalk intensity I_X, we measured $F_{1|2}$ for a probe beam with relative intensity attenuated to $7.2(2) \times 10^{-5}$ when addressing ion1. The measured $F_{1|2}$ with the attenuated light confirmed that our intensity crosstalk is within the regime of $\lesssim 8 \times 10^{-5}$. This estimation of the crosstalk intensity is further supported by our atomic physics simulations.

For comparison, the calculated $F_{1|2}$ (solid gray line) was obtained for a diffraction-limited Gaussian beam (with NA = 0.16) and a beam waist of $w = 1.50$ µm. In these measurements, we used $I_2 = 1.25(16)I_{\text{sat}}$, $I_\pi/I = 0.86$, $I^{(11)}/I = 1$, and $\tau_{\text{op}} = 9.73(7)$ µs.

4.12.2 Site-selective state measurement

State measurement of the ion qubits is achieved by detection of the state-dependent fluorescence [77]. The ions are excited by light resonant to the $D_1^{(10)}$ (Chapter 2) cycling transition and the light they scatter is detected with finite efficiency by a measurement apparatus. The duration of this measurement (detection time τ_{d}) is chosen such that the state of the ion can be inferred with high fidelity(see chapter 2). Detection time is highly dependent on the efficiency of the measurement apparatus, and a detection time of as low as 11 µs with state-detection fidelities as high as 99.931(6)% has been recently demonstrated for $^{171}\text{Yb}^+$ trapped ions [18]. Hence, we report $F_{1|2}$ when a detection beam was applied on ion2 location for a time of 11 µs. Note that the detection beam parameters used in Ref. [18] are compatible with our detection beam.

It is important to note that σ^+ and σ^--polarized $D_1^{(10)}$ light do not cause AQMs to the asset qubit in the $S_{1/2}\,|F = 1, m_F = 0\rangle$ state, as long as we ignore the low probability of off-resonant excitation (Chapter 2). Therefore, to maximize the fidelity of the asset qubit, it is ideal to minimize the proportion of π light. However, the optimal polarization [26] for the highest scattering rate and, consequently, the highest detection fidelity for ion2 is given by $I_\pi = I_{(\sigma^+)} = I_{(\sigma^-)}$.

Figure 4.16 displays the relationship between $F_{1|2}$ and the polarization of the detection probe light, revealing that the highest fidelity is achieved when the probe light has no π-polarization. The dashed line in the figure represents the optimal polarization for state detection of the process qubit (ion2). The dotted line, on the other hand, indicates the polarization used to measure $F_{1|2}$ in subsequent parts of the experiment. The measured

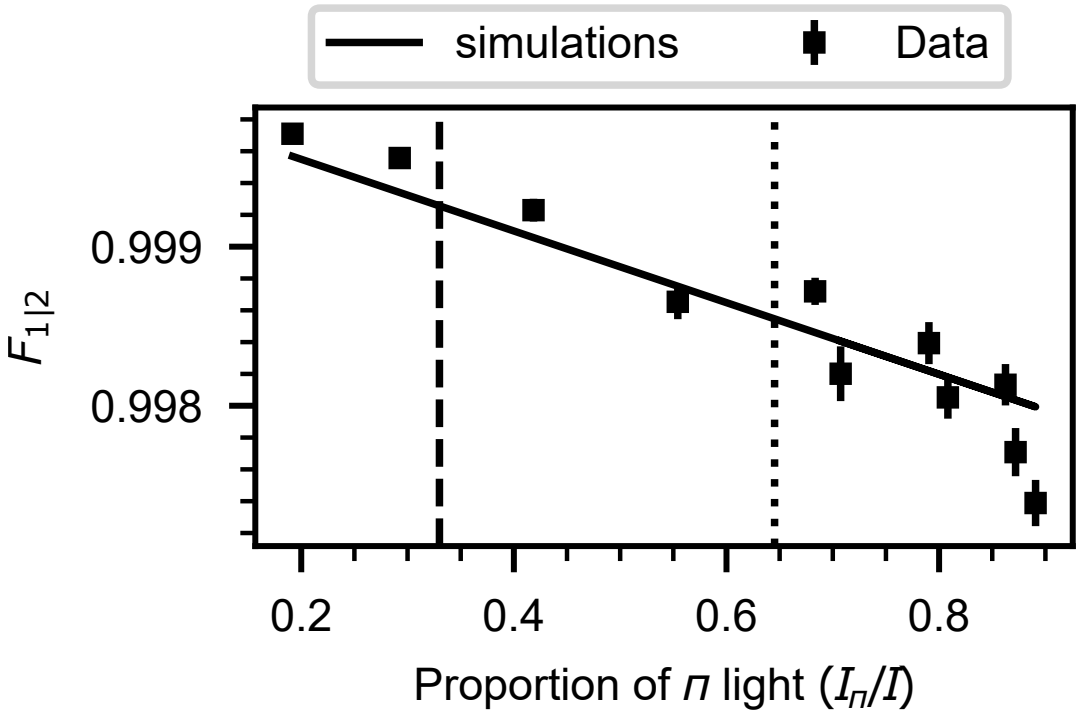

Figure 4.16: **Polarization Dependence of $F_{1|2}$ for State Measurement:** Relationship between fidelity ($F_{1|2}$) and the polarization of the detection probe light. The dashed line represents the optimal polarization for the process qubit (ion2) state detection, while the dotted line represents the polarization used to measure $F_{1|2}$ in subsequent measurements.

values of $F_{1|2}$ at $d = 4w$ correspond to a detection probe light with an intensity of $I = 1.25(16)I_{\text{sat}}$, applied for a duration of $\tau_{\text{d}} = 11$ µs. The error bars in the plot represent the standard deviation in estimating $F_{1|2}$, obtained from 20 bootstrapping repetitions performed on 200 measurements.

We then examine $F_{1|2}$ as a function of beam position relative to the ion (d) (Fig. 4.17) using a detection beam in a case-B configuration. Figure 4.17 shows $F_{1|2}$ vs the distance d (case-B). For comparing the crosstalk I_X, we measure $F_{1|2}$ for a probe beam with relative intensity attenuated to $7.2(2) \times 10^{-5}$ addressing ion1 (triangle marker at $d = 0$). For comparison, $F_{1|2}$ is calculated(solid gray line) for a diffraction-limited (NA=0.16) Gaussian beam of beam waist w. We find that the long coherence times (T_2^*) result in fidelities $F_{1|2} > 99.5\%$ for $d \geq 4w$ and $F_{1|2} > 99.9\%$ for $d \geq 20w$. Note that the polarization of the

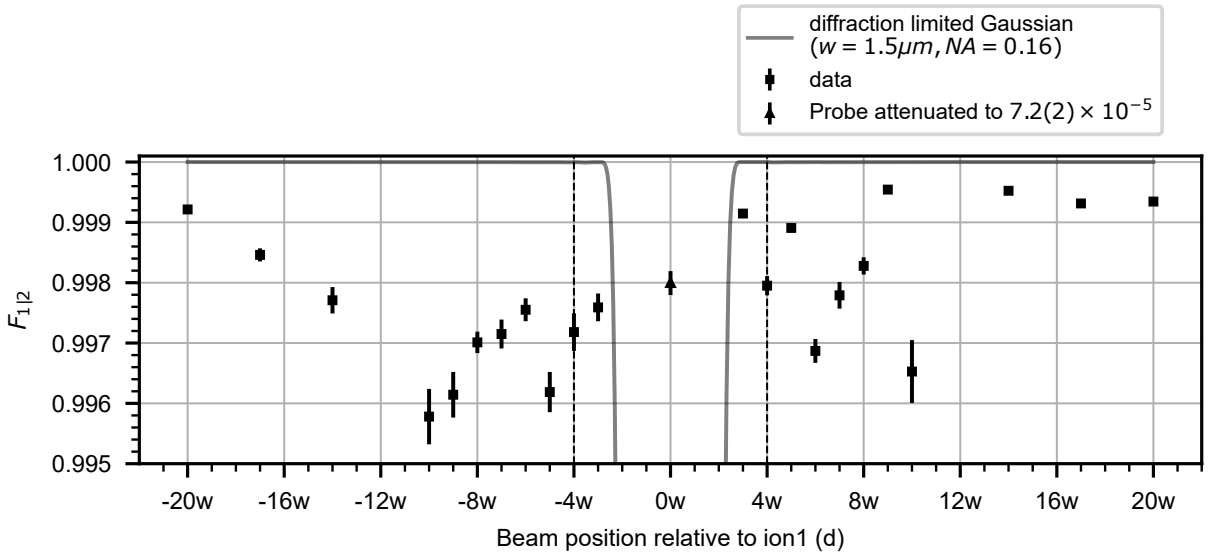

Figure 4.17: **Characterization of Fidelity ($F_{1|2}$) for State-Measurement in Case-B Configuration:** The figure depicts the characterization of fidelity ($F_{1|2}$) in the Case-B configuration for state-measurement as a function of the beam position relative to the ion (d) in units of the Gaussian beam waist (w).

probe beam for these measurements is $I_\pi \approx 0.6$ and even higher fidelities could be achieved for the optimal detection polarization (Fig. 4.16).

Figure 4.18 illustrates the measured $F_{1|2}$ for various shifted locations of the ion from the center of the field of view (FOV). In this context, the center of the FOV refers to the location where the aberrations have been characterized and compensated. The results demonstrate that $F_{1|2}$ is preserved over a large FOV of 460 µm. This high-fidelity is maintained even when the ion is shifted approximately 100 µm and 200 µm away from the center of the FOV, indicating the feasibility of in-situ measurements in a long chain of ions. It is worth noting that in all the aforementioned measurements, aberrations were compensated using the phase profile measured at $b = 0$. Furthermore, by compensating aberrations using a phase profile measured at a different point located away from the center of the FOV, it is possible to achieve even higher fidelities at that specific point.

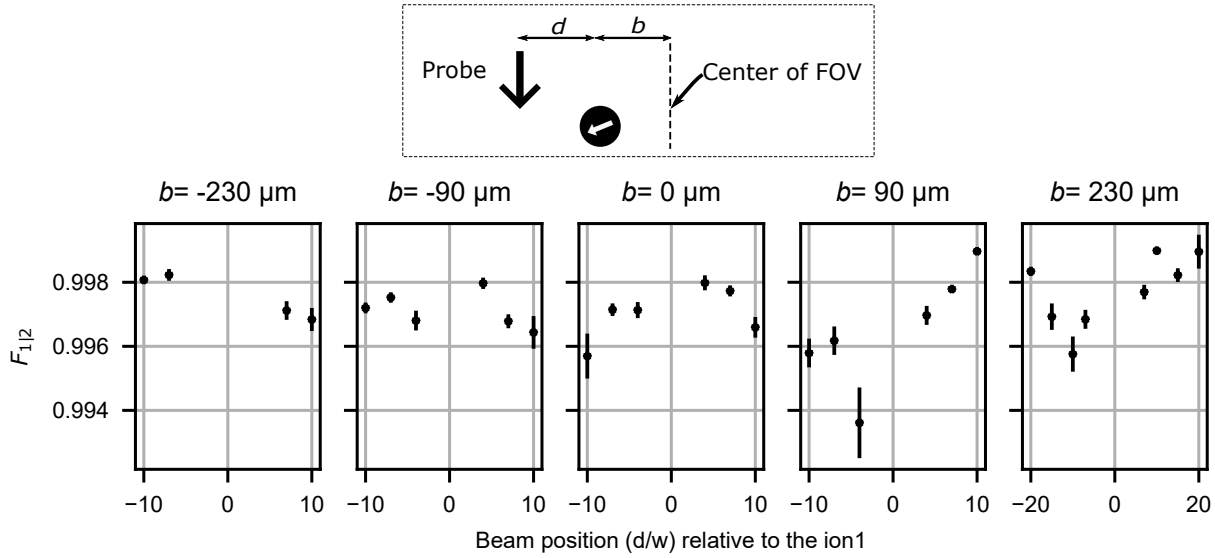

Figure 4.18: $F_{1|2}$ **Dependence Across the Field of View (FOV):** This figure presents the measured $F_{1|2}$ for various shifted locations of the ion from the center of the field of view (FOV).

Process qubit detection efficiency

Consider a probe beam resonant to $D_1^{(10)}$ transition illuminates the process qubit for a time t. The scattered light from the process qubit is collected using a detector of efficiency ε_{sys}. The state of the qubit is inferred to be $|\uparrow_z\rangle$ if the detector registers a single count.

We use the approach presented in Ref. [75, 1, 18] to estimate the detection fidelity. The error in detecting the $|\uparrow_z\rangle$ is given by the probability of detecting no photons when the qubit is initialized in $|\uparrow_z\rangle$ state [18].

$$\begin{aligned} P_{t,|\uparrow\rangle}(n=0) =& \frac{R_{\text{d}}}{\varepsilon_{\text{sys}}R_{\text{o}}+R_{\text{d}}} e^{-R_{\text{bg}}t}\left[1-e^{-(\varepsilon_{\text{sys}}R_{\text{o}}+R_{\text{d}})t}\right] \\ &+ e^{-R_{\text{d}}t}e^{-((\varepsilon_{\text{sys}}R_{\text{o}}+R_{\text{bg}})t} \end{aligned} \tag{4.13}$$

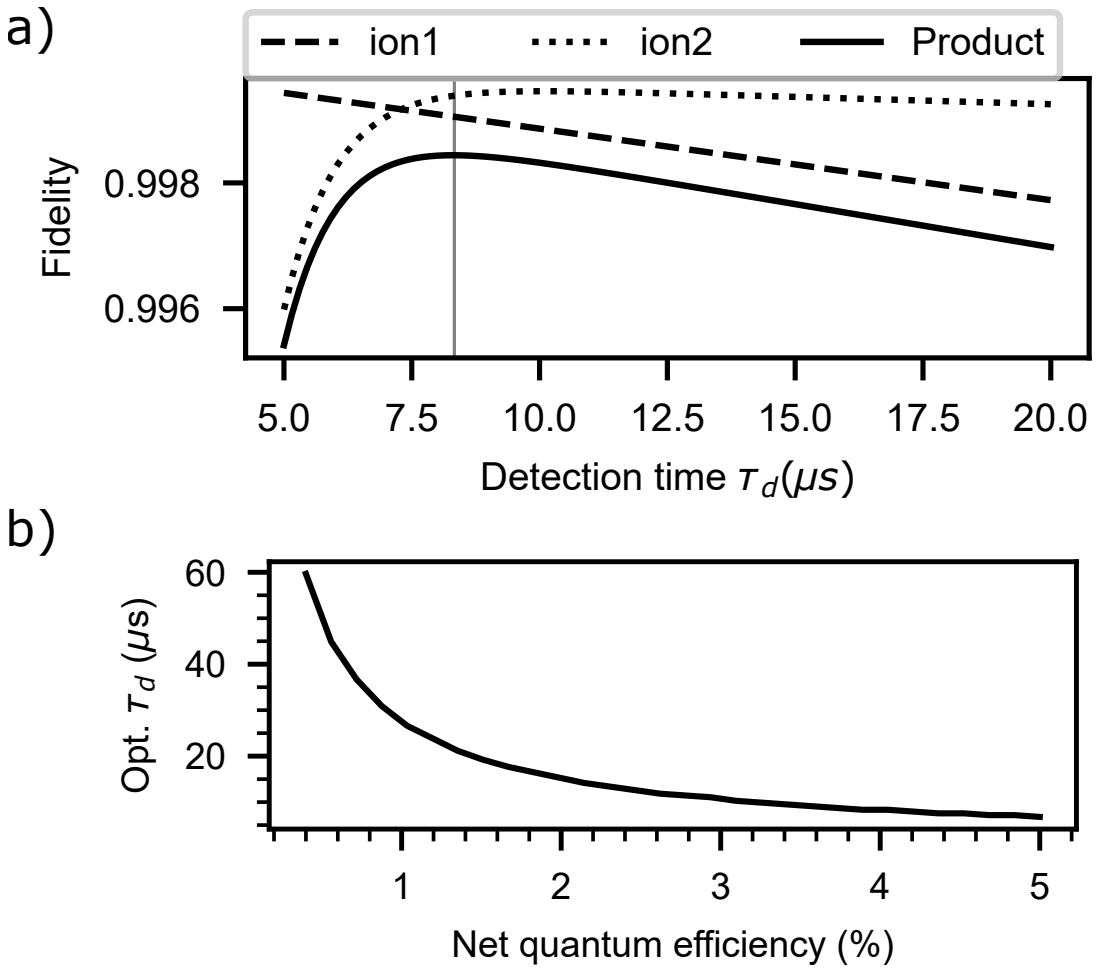

Figure 4.19: **Total Fidelity Estimation:** (a) Displays the calculated detection fidelity of the process qubit (ion2) and the preservation fidelity of the asset qubit ($F_{1|2}$) as functions of the detection time (τ_{d}). (b) Shows the optimal detection time (optimal τ_{d}) as a function of net detection efficiency.

Here R_o denotes the scattering rate of state $|\uparrow_z\rangle$, R_b denotes the bright pumping rate, and R_d denotes the dark pumping rate [75]. We note a plausible typo in the above expression in Ref. [18] with a prefactor $\varepsilon_{\mathrm{sys}}$ missing in the exponential of the second term.

Similarly, the probability of detecting no photons when the qubit is initialized in state $|\downarrow_z\rangle$ [18]

$$P_{t,|\downarrow\rangle}(n=0) = \frac{R_{\mathrm{b}}}{\varepsilon_{\mathrm{sys}} R_{\mathrm{o}} - R_{\mathrm{b}}} e^{-R_{\mathrm{bg}} t} \left[e^{-R_{\mathrm{b}} t} - e^{-\varepsilon_{\mathrm{sys}} R_{\mathrm{o}} t} \right] + e^{-R_{\mathrm{b}} t} e^{-R_{\mathrm{bg}} t} \tag{4.14}$$

The average fidelity of state-detection of the process qubit is given by

$$F = \frac{\left(1 - P_{t,|\uparrow\rangle}(n=0)\right) + P_{t,|\downarrow\rangle}(n=0)}{2}$$

The detection fidelity of the process qubit, considering a given detection efficiency (limited by the numerical aperture and photon collection loss), increases with longer detection times (τ_{d}) while $F_{1|2}$ decreases. However, the optimal detection time depends on the relative importance of these fidelities in a specific quantum algorithm. One possible metric for finding the optimal detection time is to maximize the product of these two fidelities.

Figure 4.19a presents the calculated detection fidelity of the process qubit (ion2) [1, 18] and the preservation fidelity of the asset qubit ($F_{1|2}$) as a function of the detection time (τ_{d}). In estimating the detection fidelity of the process qubit, we assume that it is illuminated with a detection beam of $I_2 = I_{\mathrm{sat}}$ with optimal polarization, and the measurement apparatus has a net detection efficiency of 4%, which is compatible with state-of-the-art experiments. We employ a photon count thresholding method to differentiate between the states $|\uparrow_z\rangle$ and $|\downarrow_z\rangle$. Additionally, we utilize an algorithm that completes the detection process upon measuring the first photon, effectively reducing the detection time by a factor of 2 [18, 42, 53].

For estimating $F_{1|2}$, we assume an intensity crosstalk of $I_X = 5 \times 10^{-5}$, $I_2 = I_{\mathrm{sat}}$, and optimal polarization for the process qubit state-detection. The vertical line at $\tau_{\mathrm{d}} \approx 8.5$ µs indicates the optimal detection time that maximizes the product of these two fidelities.

This optimal detection time is highly dependent on the net efficiency of the detection apparatus. Figure 4.19b shows the optimal detection time (opt. τ_{d}) as a function of the net detection efficiency of the measurement apparatus.

4.13 Summary and Discussion

In summary, we have demonstrated high-fidelity in preserving an ion qubit while the neighboring qubit is reset or measured at a few microns distance. Our results are comparable to the state-of-the-art QIP experiments [16, 28, 18] that employ shuttling of qubits to be preserved away from reset or measurement laser beams by hundreds of microns distance.

Our crosstalk measurement scheme employs temporal separation of probe light illumination and detection of an ion qubit and hence overcomes sensitivity limitations due to unwanted background scattering of resonant light from optics leaking onto photon detectors in previous experiments [93]. This in turn allows measurement of crosstalk over a large dynamic range.

Ions are localized to < 100 nm at typical laser-cooling temperatures and trap frequencies, making it possible to characterize aberrations with the ion sensor for larger numerical aperture (NA) systems. With large NA, the beam waist w decreases, thus the ion separations can be decreased without increasing P_{AQM} to achieve higher qubit-qubit interaction strengths [68].

Our demonstrated high-fidelity over a field of view (FOV) of 450 µm corresponds to $\sim$ 50 ions in a linear chain for typical harmonic trapping parameters (radial trap frequency of approx. $2\pi \times 5$ MHz and axial trap frequency of approx. $2\pi \times 30$ kHz). The slight decay of fidelity away from the center of FOV can be compensated by recalibrating aberrations away from the center. However, even without extra calibrations, the fidelity $F_{1|2}$ can be maintained over the entire chain, as inter-ion separation away from the center of an ion chain also increases in a harmonic trap (from $4w = 6$ µm at the center becoming $\approx 10w = 15$ µm near the edge for parameters above [102]).

For typical radiofrequency ion traps (e.g., surface traps [64], 'blade' electrode traps [36]), NA > 0.5 is accessible for photon collection simultaneously with NA ~ 0.3 (in a perpendicular direction) for optical addressing, allowing for independent optimization for photon collection and addressing. While high quantum efficiency and negligible dark counts make ~ 10 µs detection time possible [18], less-expensive photomultiplier tubes (PMT) can also allow ~ 20 µs detection time (Fig. 4.19b) [1, 18] under otherwise identical conditions for maintaining high asset qubit preservation fidelities of $> 99.2\%$.

While the asset qubit coherence in our measurements is limited by intensity crosstalk, the P^{*}_{AQM} from inter-ion scattering for state detection may be suppressed even further with the proper choice of the local magnetic field. For $^{171}\mathrm{Yb}^{+}$, it is possible to suppress the intensity of π light scattered from the process qubit in the direction of the asset qubit by aligning the magnetic field along the ion chain [13], thereby maximizing $F_{1|2}$. In contrast,

the optimal orientation of the magnetic field for state reset is perpendicular to the ion chain.

Comparing with the inter-ion scattering calculations in Ref. [11], we find that the insensitivity to $\sigma^{\pm}$ photons (for state-detection through $D_1^{(10)}$ transition) for $^{171}\mathrm{Yb}^{+}$ gives a reduction of about factor of 2 approximately in P_{AQM} compared to some other species, such as $^{40}\mathrm{Ca}^{+}$ that is affected by all polarizations. Our scheme of obtaining low P_{AQM} can be easily adapted to other ion species or different QIP platforms that benefit from high-quality individual optical addressing.

Chapter 5

Dissipative Many body cooling

This chapter focuses on an analog quantum simulation protocol that takes advantage of the mid-circuit resets discussed in the previous chapter. The project was initiated in collaboration with Dr. Azadeh Mazloom and Dr. James Freericks, who theoretically proposed this protocol and provided valuable insights. The chapter presents both the theoretical calculations and the experimental results, all of which were conducted by me with the support and assistance of my group members.

5.1 Overview

As described in the introduction (chapter 1), one of the problems that analog quantum simulators have the potential to address is the computation of highly correlated states, such as the ground state of a Hamiltonian, with the aim of achieving a quantum advantage. Typically, in analog quantum simulators, this task is accomplished through adiabatic evolution [49, 85, 45, 46]. In this approach, the system is initially prepared in the ground state of a simple Hamiltonian that can be easily prepared (Figure 5.1). Subsequently, the system is gradually transitioned or ramped to the target system's Hamiltonian. By ensuring that this process is conducted slowly enough (according to the adiabatic theorem) [68], the final state of the system will correspond to the ground state of the target system.

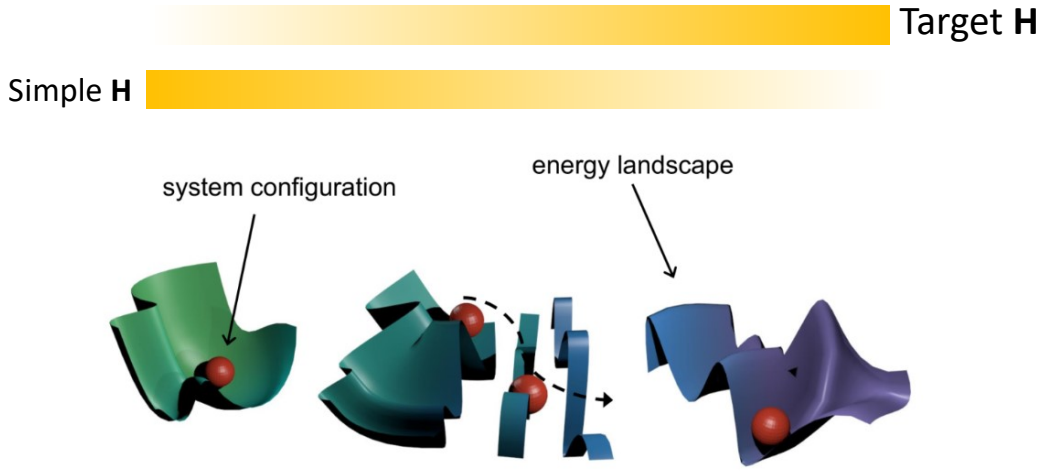

Figure 5.1: **Adiabatic quantum simulation illustration:** Illustration of the adiabatic evolution process in analog quantum simulation, transitioning from a simple initial Hamiltonian to the target system's Hamiltonian. By ensuring a slow enough transition, the final state corresponds to the ground state of the target system. Illustration taken from Ref. [17]

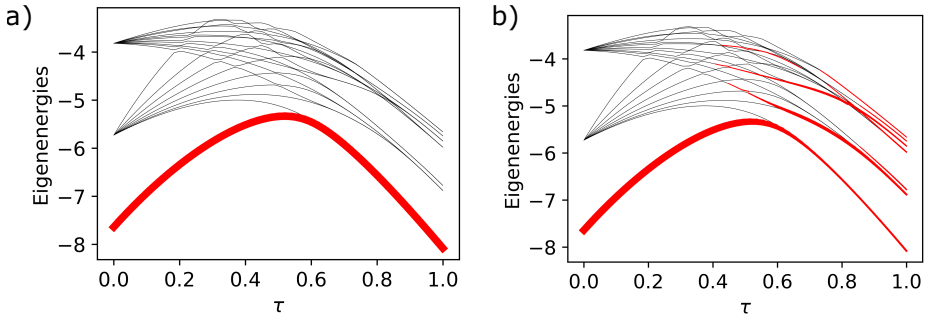

Figure 5.2: **Adiabatic quantum simulation energy spectrum:** (a) Energy spectrum (gray lines) and occupation probability (thickness of the red line) for an 8-spin 1/2 particle system undergoing adiabatic quantum simulation. Slow ramp from a simple Hamiltonian H_0 to a fully connected Hamiltonian H_1. (b) Energy spectrum (gray lines) and occupation probability (thickness of the red line) for the same simulation as (a), but with a ramp 10 times faster. Ramping speed significantly affects the probability of reaching the ground state at the end of the quantum simulation.

However, adiabatic quantum simulation does have its limitations when it comes to effectively solving certain types of Hamiltonians. The time it takes to ramp down the initial simple Hamiltonian to the final complex version determines the probability of preparing the system in the ground state. For example, figure 5.2 shows an adiabatic quantum simulation protocol for 8 spin-1/2 particles. The simulation starts with the system in the ground state of a simple Hamiltonian, $H_0 = \sum_i h_0 \sigma_i^z$, and gradually ramps to a fully connected Hamiltonian of the form $H_1 = \sum_{i>j} J_{i,j} \sigma_i^x \sigma_j^x$. The plot displays the eigen energies(scaled units) spectrum of the Hamiltonian as a function of time (represented by gray lines), and thickness of the red line represents the occupation probability. Figure 5.2a illustrates a slow ramp, while Figure 5.2b demonstrates a ramp that is 10 times faster than the first one. These figures highlight the importance of ramping speed in achieving the ground state with a high probability. Moreover, as a system approaches a phase transition, adiabatic quantum simulations become increasingly infeasible. The task becomes more challenging primarily because of the decreasing energy gaps between many-body states [21, 69].

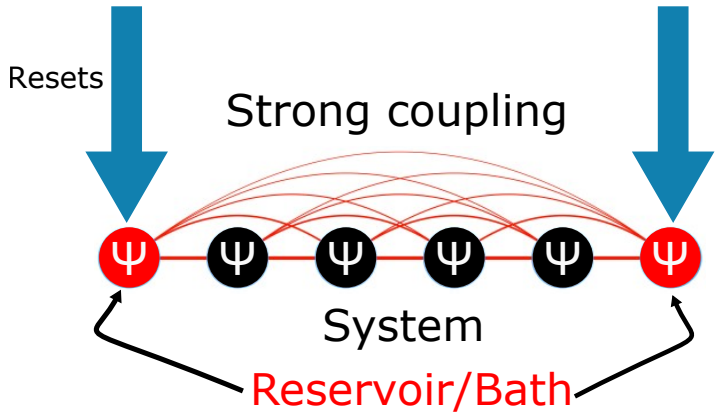

Figure 5.3: **Dissipative Many Body Cooling concept:** A chain of 6 ions is divided into two parts, with the central 4 ions (black) representing the system, and the edge two ions (red) assigned as the reservoir/bath. All the ions are coupled through all-all long-range interactions (red lines). Periodic resets (blue arrows) are performed on the reservoir ions.

In digital quantum simulators the ground state preparation is done with variational quantum algorithms approach which can have limitations on number of gates that can be applied or could be limited by optimization landscape being flat [65].

One promising alternative approach is reservoir engineering for many-body cooling and ground state preparation [66, 33]. The concept involves coupling a system with a controllably engineered dissipative reservoir, allowing us to steer the quantum state of the system towards the desired state of interest. Through repeated entanglement of the quantum system with the dissipative reservoir, followed by projection of the reservoir spins to a chosen state, spin excitations are effectively transferred from the system to the reservoir. Controlled dissipation or reset operations are then used to remove excitations from the reservoir. In this chapter, I aim to present an implementation of this simulation on our trapped ion quantum simulator, with the goal of preparing a subsystem closer to the ground state.

Consider a chain of ions that we divide into two parts: the system and the bath. Figure 5.3 illustrates a chain of 6 ions that are all-to-all coupled. The central 4 ions are designated as the "system", while the 2 edge ions on both sides of the chain are labeled as the "bath". The coupling between the ions is achieved by simulating an effective Ising-type interaction Hamiltonian using the Molmer Sorensen scheme [67], as described in Chapter 2. This scheme enables the interaction between all the ions in the chain. The edge bath/reservoir ions undergo periodic resets utilizing the capabilities of high fidelity mid-circuit resets [71], which were discussed in detail in the previous chapter. By strategically timing the resets, we can steer the "system" to eventually converge to the ground state of the simulated Hamiltonian(Eqn.5.1). It is interesting to note that the bath is strongly coupled to the entire system, as indicated by the red lines in Figure 5.3, rather than being exclusively coupled to the boundary; it extends throughout the entire bulk.

In this chapter, I first present the implementation of an effective Transverse Field Ising model on a chain of ions. I provide a detailed description of the protocol and present numerical results demonstrating promising cooling results close to the ground state. The optimization of various parameters, such as the reset interval time, is showcased using experimentally achievable parameters. Next, I calibrate the parameters of the simulator and execute the Dissipative Many Body Cooling protocol, successfully demonstrating its efficacy in reducing the system's energy. However, the system's energy does not reach the ground state as closely as expected based on the numerical results. I explore a plausible explanation for this discrepancy in terms of additional error terms present in the Hamiltonian.

5.2 Interaction Hamiltonian

Before delving into the details of the dissipative many-body cooling(DMBC) protocol, let us discuss the Hamiltonian for which we aim to prepare the ground state. As explained in Chapter 2, one of the native Hamiltonians that can be generated in our system is the long-range Ising model. By incorporating an effective magnetic field generated through Raman beams driving the carrier transition, we can construct the Transverse Field Ising model.

The chosen form of the Hamiltonian is given by:

$$H = \sum_{i,j} J_{i,j}\sigma_i^x\sigma_j^x + B_0\sum_i \sigma_i^y \tag{5.1}$$

Here, $J_{i,j}$ represents the coupling strength between spins i and j, while B_0 corresponds to the transverse magnetic field strength. The requirement for the magnetic field (the second term in the equation) is that it needs to be orthogonal to the x basis, making it either aligned with the y or z bases. As discussed in Chapter 2, it is relatively straightforward to controllably introduce a transverse field in the x and y bases for trapped ions. For this set of results, I have chosen the field to be in the y basis. However, it is also possible to add a transverse field in the z basis by inducing additional Stark shifts on the ions using various implementable protocols. One protocol we implemented in our system involves detuning the clock of the external oscillator relative to the frequency difference between the qubit states. By introducing this additional detuning, we can effectively create a magnetic field along the z-axis with a field strength equal to the detuning.

The value of the coupling strength in the equation above is dependent on various parameters of the trap and the Raman beams. It is given by:

$$J_{i,j} = \Omega_i\Omega_j\left(\frac{\hbar\Delta k^2}{2m}\right)\sum_k \frac{b_i^k b_j^k}{\mu^2-\omega_k^2} \tag{5.2}$$

Here, Ω_i represents the carrier Rabi frequency, which is determined by the intensity of the Raman beams. μ refers to the detuning of the beams from the carrier transition. The terms b_i^k and ω_k depend on the trap parameters. Further details about the other terms are presented in Chapter 2.

In order to accurately estimate the generated Hamiltonian, a comprehensive set of calibrations is required. The following section outlines the calibration procedures we use to determine the parameters mentioned above.

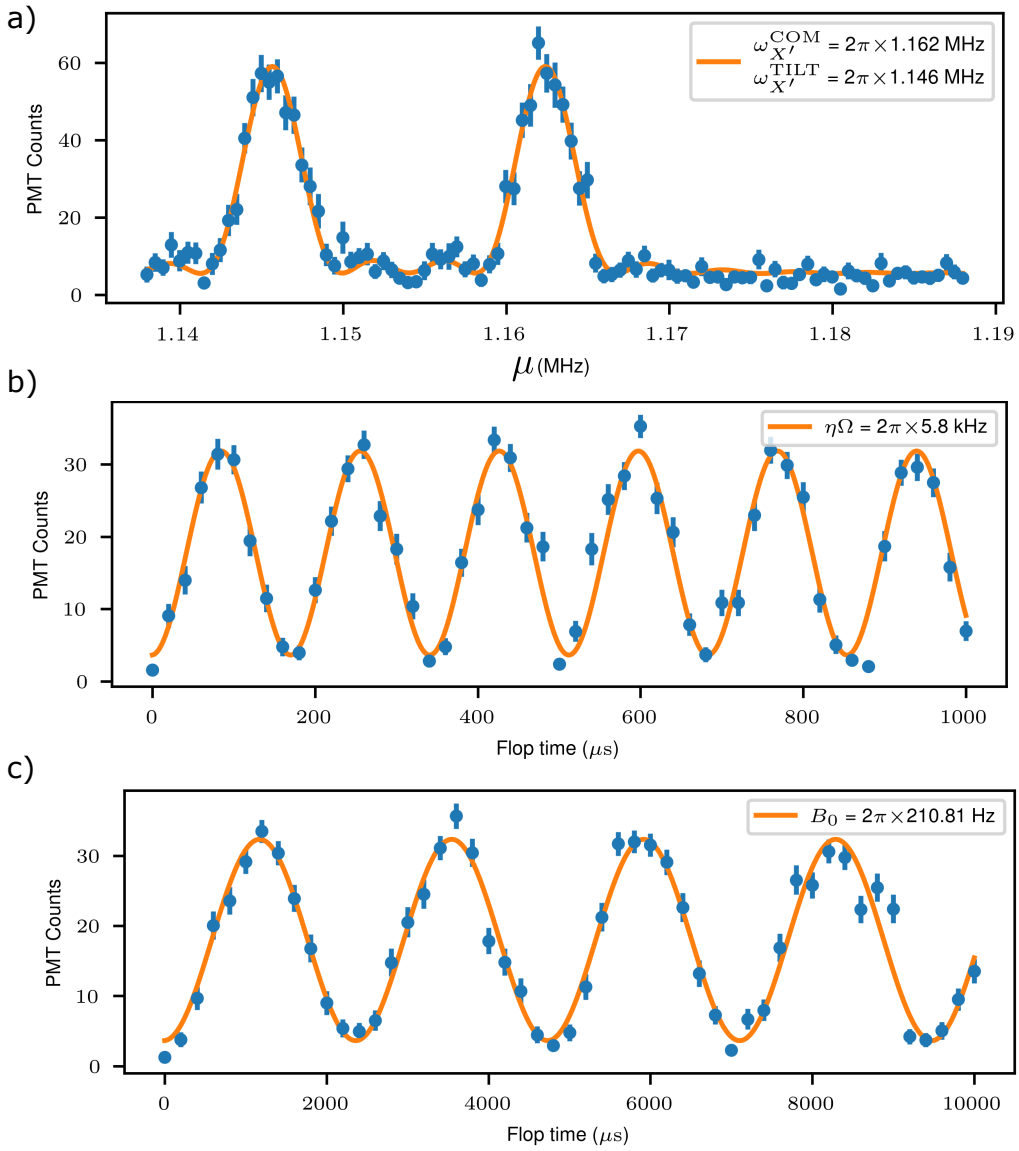

Figure 5.4: **Parameter Calibration using a single ion:** (a) PMT counts as a function of the detuning (μ) employed for extracting $\omega_{X'}^{\mathrm{COM}}$ and $\omega_{X'}^{\mathrm{TILT}}$. In this context, μ represents the detuning of the Raman beatnote frequency from the carrier transition (as described in Chapter 2). (b) Rabi flop of a single ion driven at the blue-sideband transition. (c) Rabi flop of a single ion driven at the carrier transition with reduced amplitude. Error bars represent the standard error for 200 repetitions

5.2.1 Calibrations

The accurate estimation of the Hamiltonian requires a set of parameters, including the Rabi frequency Ω_i, the radial trap frequency $\omega_{\mathrm{X}'}$, the axial trap frequency ω_{Y}, the transverse field strength B_0, and the detuning μ.

Figure 5.4 illustrates some of the experimental scans conducted for parameter calibration. Figure 5.4a shows a scan of the frequency of one of the Raman beams relative to the other, centered around the carrier transition frequency. This scan enables the determination of the center of mass normal mode $\omega_{X'}^{\mathrm{COM}}$ and the tilt normal mode $\omega_{X'}^{\mathrm{TILT}}$. The radial trap frequency $\omega_{\mathrm{X}'}$ is equal to $\omega_{X'}^{\mathrm{COM}}$, and the axial trap frequency ω_{Y} can be calculated using the relation [44]

$$\omega_{\mathrm{Y}} = \sqrt{(\omega_{X'}^{\mathrm{COM}})^2 - (\omega_{X'}^{\mathrm{TILT}})^2}$$

Figure 5.4b demonstrates the Rabi flop of a single ion driven at the blue-sideband transition. This scan allows estimation of the sideband Rabi frequency $\eta\Omega$, where η is the Lamb-Dicke parameter. Consequently, the carrier Rabi frequency Ω can be estimated for the given parameter regime. Figure 5.4c shows the Rabi flop of a single ion driven at the carrier transition but with reduced amplitude. This calibration measurement facilitates the estimation of the transverse field strength B_0. Note the difference in inferring these frequencies from the plots above: $\eta\Omega$ corresponds to the 2π time in the blue-sideband flop, whereas B_0 corresponds to the 4π time. This is because the y-axis of the plot is proportional to the probability rather than the amplitude. Also note that the parameters for which the above experiments were performed are shown for illustration purposes only. Parameters like $\eta\Omega$ and B_0 are adjusted by varying laser intensities as needed for the subsequent experiments.

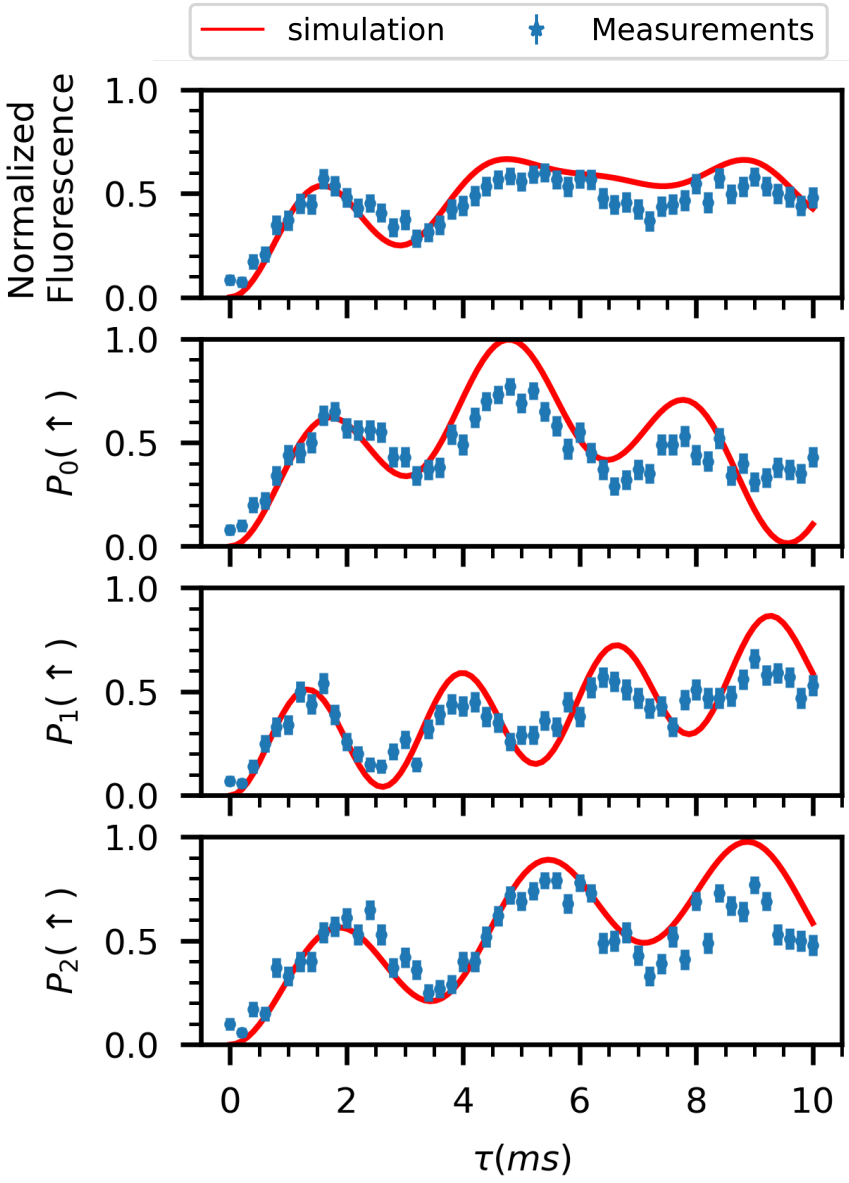

Figure 5.5: **Time evolution of three ions under interaction Hamiltonian:** The plot shows the probabilities of ions 0, 1, and 2 being in the $|\uparrow_z\rangle$ state as a function of time when subject to the Hamiltonian H in Eqn.5.1. Each datapoint represents a mean for 100 experimental repetitions, with error bars representing the standard error. The simulated probabilities, obtained using calibrated parameters, agree with the measured probabilities.

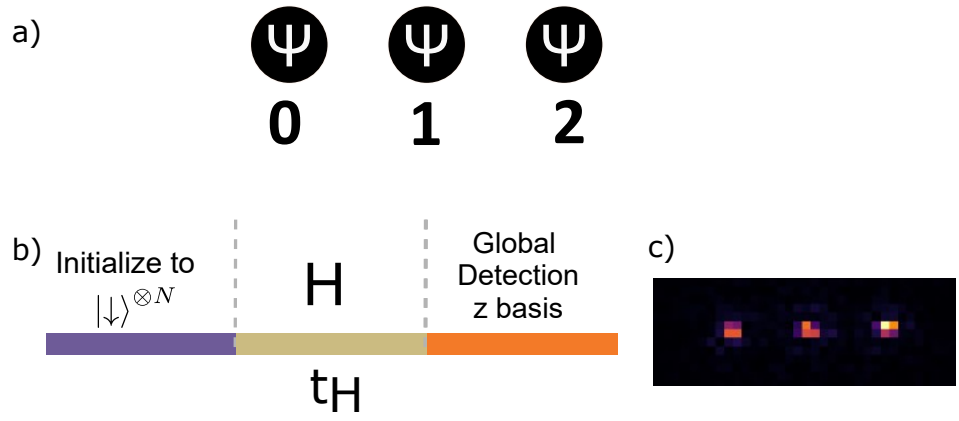

Figure 5.6: **Setup for three ion analog quantum simulation of Ising model:** (a) Three ions in an ion chain labeled as 0, 1, and 2. (b) The ions initialized to the $|\downarrow_z\rangle$ state. The ions are subjected to the Hamiltonian H for a duration of t_H. (c) An image captured by a qCMOS camera showing the three ions

5.2.2 Analog simulation of transverse field Ising model

With the calibrated parameters obtained earlier, the analog quantum simulation is performed using the Hamiltonian described in Eq. 5.1. Figure 5.6b presents a simple schematic of the time sequence. Three ions (labeled as 0, 1, and 2 in Figure 5.6a) undergo Doppler cooling for 3 ms, followed by Raman sideband cooling for 8 ms [106]. Subsequently, a global state reset stage initializes all ions to the state $|\downarrow_z\rangle$. Once the ions are prepared in the $|\downarrow_z\rangle$ state, they are subjected to the Hamiltonian(Eqn.5.1) using the calibrated Raman beams and a detuning value of $\mu = 2\pi \times 15$ kHz. With these parameters. For these experiments, I have chosen the side Rabi frequency $\eta\Omega$ to be approximately $2\pi \times 3.5$ kHz, with η for our geometry being 0.12. The maximum coupling strength resulting from the above parameters is $J_0 = \max(J_{i,j}) = 2\pi \times 105$ Hz. Note that here I chose the transverse field strength $B_0 = 0$.

After applying the Hamiltonian H to the ions for a duration of t_H, the ions' states are measured using a qCMOS camera (Figure 5.6c). Since the PMT lacks site-selective measurement capabilities, the camera is utilized to detect the state of each ion. The camera

captures an image with a detection time of 1.5 ms, which projects the ions into the z basis. It is important to note that the state detection process introduces a camera processing overhead of approximately 6 ms. For a given t_H, these experiments are repeated 200 times to obtain statistics. During each measurement, the state of each ion is classified as either $|\uparrow_z\rangle$ or $|\downarrow_z\rangle$ using a machine learning algorithm[1]. The classifier helps us estimate the ion's state from the camera image (3x3 pixels for each ion). This classifier is trained using labeled datasets of 5000 images when the ions are initialized in $|\downarrow_z\rangle$ and 5000 images when the ions are initialized in $|\uparrow_z\rangle$. Note that I trained a separate classifier for each ion, so this does not account for the crosstalk from other ions. This classifications leads to fidelities of greater than 92% in accurately classifying the ion states (when tested on another test data set). This fidelities are mostly limited by the light collection efficiencies of our imaging system. The classified measurements are then used to measure expectations of various operators or probabilities.

With the above parameters and classification strategy, the ions are subjected to the interaction Hamiltonian and Figure 5.5 illustrates the probabilities of ions 0, 1, and 2 being in the $|\uparrow_z\rangle$ state as a function of time, where the simulations using the calibrated parameters exhibit agreement with the measured probabilities. These calculations provide an estimate of the accuracy of our simulator calibration. The discrepancy in the measurements from the experiments at times greater than 6 ms in Figure 5.5 is mostly attributed to the decoherence caused in our system due to intensity fluctuations of the Raman beams. These sources of intensity fluctuations in the Raman beams could be reduced through active stabilization of the laser beams in future experiments.

5.3 Dissipative Many Body Cooling (DMBC) protocol

With the interaction Hamiltonian setup, let us examine the reservoir engineering protocol in greater detail. The chain of ions is divided into two parts: one ion located at the edge of the chain is chosen as the bath/reservoir, while the remaining chain constitutes the system. Figure 5.7 illustrates the time sequence of the DMBC protocol. In addition to the analog simulation presented in the previous section using the Hamiltonian H for the entire chain, periodic resets are performed on the bath after time t_H. Since we have chosen the transverse field to be in the y basis, the reset operations should reset the state of the bath to the ground state of the transverse field. Therefore, the reset pulses are sandwiched

[1]Random Forrest Classification [81]

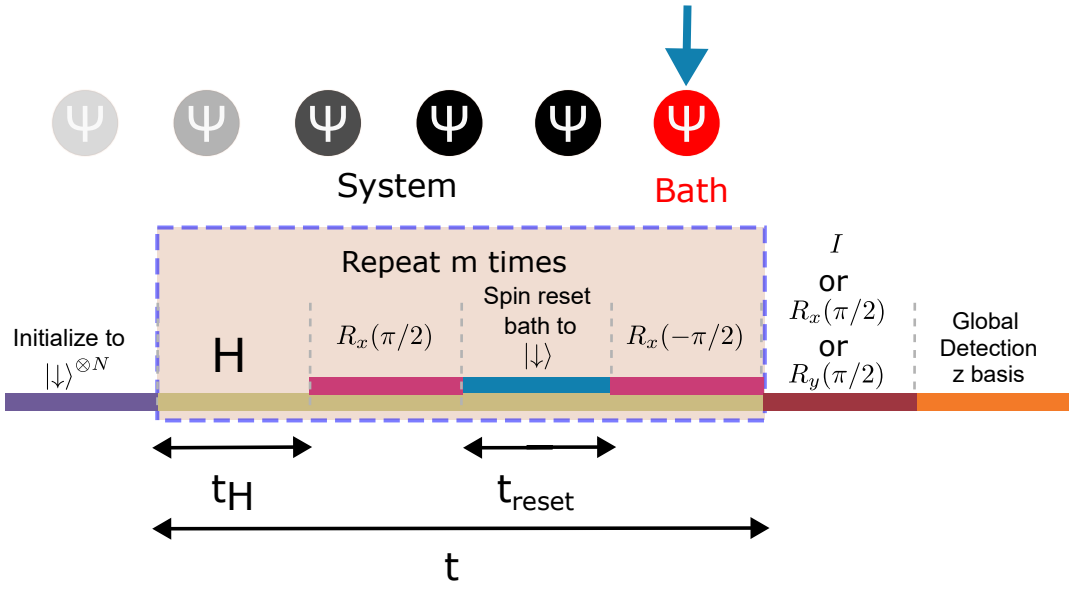

Figure 5.7: **Time sequence illustrating the DMBC (Dissipative Many-Body Control) protocol:** The figure shows the sequence of operations performed during the protocol, including reset pulses, rotation pulses, and measurements.

between $\pi/2$ rotation pulses along the x basis on the Bloch sphere. This pulse sequence effectively emulates the reset in the y basis. The entire sequence is then repeated m times before the state detection. The cumulative duration of the entire sequence is denoted as t. In the end of every sequence, an additional $\pi/2$ rotation pulse is appended, either along the x or y basis, enabling projective measurements along the y or x bases, respectively. And no pulse is added for making projective measurements in z basis. Note that during the experimental implementation, the Hamiltonian H is kept on even when rotations and resets are being performed. Since the timescales of the resets and rotation operations (approximately 10s of μs) are much smaller than the interaction timescales, this should not affect the interactions. However, this strategy of keeping the Hamiltonian on is chosen to avoid diabatic effects that may result from abruptly switching the Hamiltonian.

Following this sequence, the final energy state of the entire ion chain is measured by calculating the expectation value of the Hamiltonian, given by:

$$E(t) = \langle H \rangle = \sum_{i,j} J_{i,j} \langle \sigma_i^x \sigma_j^x \rangle + B_0 \sum_i \langle \sigma_i^y \rangle \tag{5.3}$$

Since projective measurements have been made in the x and y bases, we can calculate the expectations of the correlation operators $\langle \sigma_i^x \sigma_j^x \rangle$ and $\langle \sigma_i^y \rangle$ to estimate the energy of the entire ion chain. However, since the main goal of the protocol is in minimizing the energy of the system, the energy of the system is measured using

$$E_{\text{sys}}(t) = \langle H_{\text{sys}} \rangle = \sum_{i,j \in \text{sys}} J_{i,j} \langle \sigma_i^x \sigma_j^x \rangle + B_0 \sum_{i \in \text{sys}} \langle \sigma_i^y \rangle \tag{5.4}$$

5.4 Numerical simulations

To determine the success of the mentioned protocol in cooling the many-body state of the system to its ground state, it is necessary to establish the required parameters, including the reset interval, strength, and basis, for effectively preparing the ground state. Additionally, it is crucial to investigate whether this protocol is applicable to a large number of ions. Answering these questions directly using a quantum simulator in the initial stages may pose challenges, particularly due to the presence of drifting parameters. To address this, I conducted numerical simulations by solving the Lindblad master equation, considering the additional dissipation.

These numerical simulations were conducted using the Python package QuTiP [47]. Solving the master equation with a time-dependent Hamiltonian can be time-consuming, especially when different parts of the system operate on time scales that differ by an orders of magnitude. In this case, the reset time scales are on the order of 10μs, while the time scales for the Hamiltonian coupling are on the order of 1ms. To overcome this issue, I solve the master equation in parts.

Initially, the ion chain is prepared in the state $|\downarrow_z\rangle$ (in the z basis) and is subjected to a time-independent Hamiltonian H for a duration of t_H. Subsequently, in the density matrix of the final state $\rho(t_H)$, the bath qubit is manually reset to the ground state $|g\rangle$ corresponding to the transverse field used. The density matrix ρ' after this reset operation is given by the expression:

$$\rho' = \mathrm{Tr_B}(\rho(\mathrm{t_H})) \otimes |\mathrm{g}\rangle\langle\mathrm{g}|$$

Here, $\mathrm{Tr_B}$ denotes the partial trace operation, which traces out the bath qubits. The density matrix ρ' is then subjected to the time-independent Hamiltonian H, and this process is repeated m times.

At every time step the energy of the whole ion chain and the system is calculated using the expressions Eq. 5.3 and Eq. 5.4 respectively.

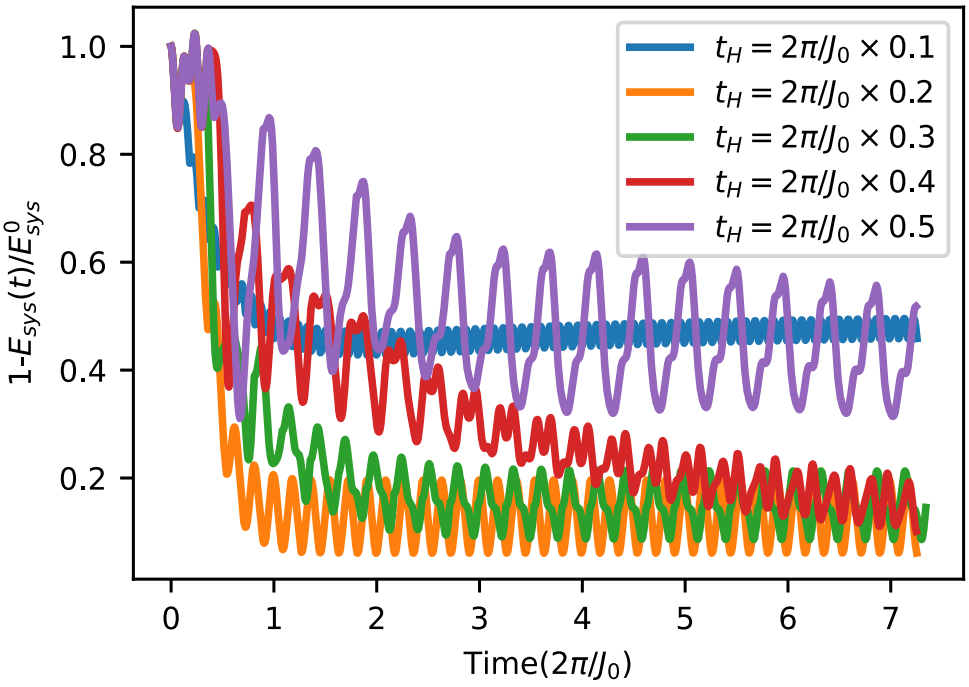

Figure 5.8: **Numerical simulation results of the DMBC protocol for a 3-ion system:** showcasing the impact of varying reset intervals. Energy values are scaled relative to E^0_{sys}, the ground state energy of the Hamiltonian H_{sys}. The quantity $1 - E_{\text{sys}}/E^0_{\text{sys}}$ decreases with zero representing the relative energy of the ground state. Time (total duration of simulation) axis is scaled as a fraction of $2\pi/J_0$.

Figure 5.8 displays the results of a numerical simulation of the DMBC protocol for a chain consisting of three ions, utilizing the parameters specified in Section 5.2.2. In this simulation, the first two ions are designated as the system, while the last ion serves as the bath. The energy values in the figure are scaled relative to the ground state energy E^0_{sys} of the Hamiltonian H_{sys} (as defined by Eq. 5.1), while the time axis is scaled as a fraction of $2\pi/J_0$, where $J_0 = max(J_{i,j})$ corresponds to the maximum coupling strength $J_{i,j}$ within the Hamiltonian. For these simulations, the transverse field is chosen to be along the y basis and the field strength B_0 is chosen to be $1.5J_0$. The figure presented showcases a series of simulations with varying reset intervals, where the reset interval (the time between consecutive resets on the bath) is approximately equal to t_H and chosen as

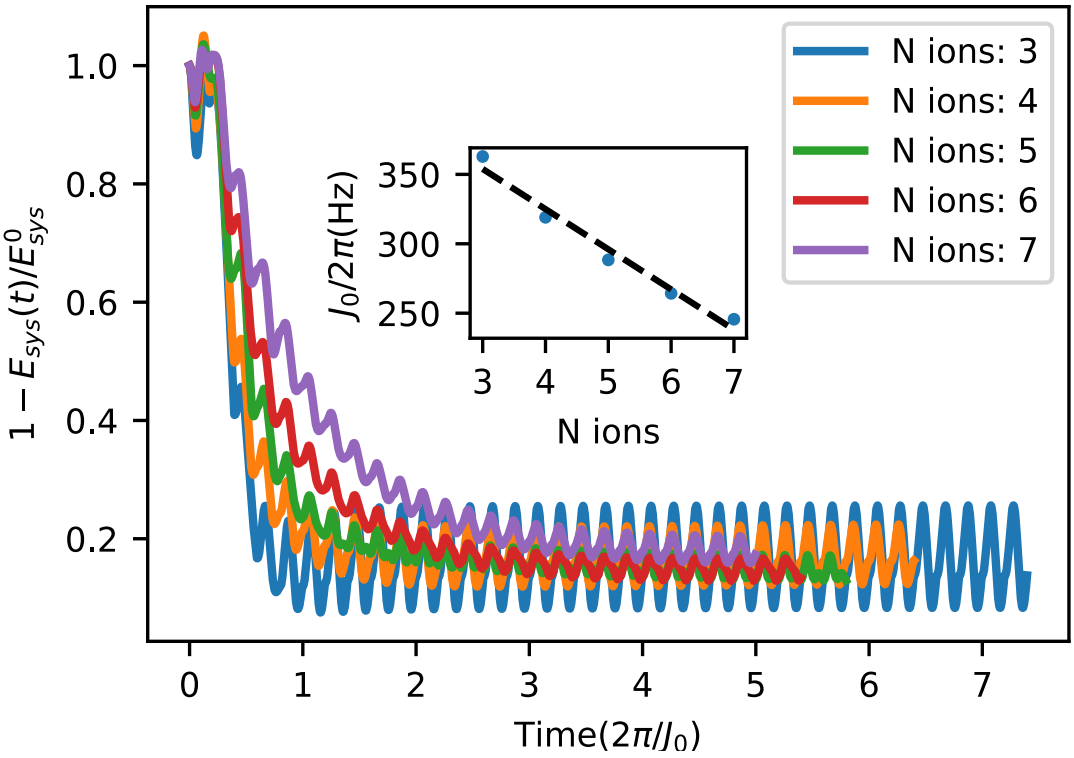

Figure 5.9: **Simulations of the DMBC protocol for varying numbers of ions:** Here the last ion in a chain serves as the bath. The reset interval is set to $0.2 \times 2\pi/J_0$. The quantity $1 - E_{\text{sys}}/E^0_{\text{sys}}$ decreases with zero representing the relative energy of the ground state. The inset illustrates the decreasing coupling strength as a function of ions, while experimental parameters such as the carrier Rabi frequency (Ω_i) are kept constant.

a fraction of $2\pi/J_0$. In our simulation Hamiltonian, the parameter J_0 signifies the rate at which correlations travel along the ion chain. Therefore, it is crucial to understand the necessary frequency of resets in relation to the speed at which entanglement builds up in the ion chain. Starting from a long reset interval, as we decrease the interval, both the cooling rate and the final state relative to the ground state improve. However, once the reset interval reaches a time of $0.2 \times 2\pi/J_0$, the performance experiences a drastic decline due to the associated heating caused by the resets. At the sweet spot, approximately around $0.2 \times 2\pi/J_0$, we observe that the protocol efficiently cools the system, bringing it very close to the ground state within a time scale of just $2\pi/J_0$. This outcome shows great promise for the effectiveness of the protocol.

Further, Figure 5.9 illustrates the simulations of the DMBC protocol for a larger number of ions, where the last ion is designated as the bath in each setting. The reset interval chosen for these simulations is $0.2 \times 2\pi/J_0$. Notably, the cooling performance remains consistent for higher ion numbers, up to 7, with rapid cooling observed within time scales of 2-3$\times 2\pi/J_0$. It is important to note that in these simulations, experimental parameters such as the carrier Rabi frequency (Ω_i) are kept constant. Consequently, the coupling strength (depicted in the inset of Figure 5.9) decreases as a function of ions.

These results demonstrate the promise of the DMBC protocol for the current experimental parameters, suggesting that it is feasible to proceed with the experiment using these settings.

5.5 3-ion DMBC quantum simulation

The simplest way to implement the protocol and benchmark the technical capabilities of our experimental apparatus, as well as to identify potential technical challenges, is to conduct a straightforward experiment using three ions. With the ions subjected to an interaction Hamiltonian similar to the one described in Section 5.2.2, Figure 5.10 illustrates the experimental analog quantum results of the DMBC protocol conducted on the three ions. Here I chose the experimental parameters such that $J_0 = 2\pi \times 110$ Hz and $B_0 = 2\pi \times 200$ Hz, with the transverse field chosen in y basis. The resets are performed using 369nm light resonant with the $D_1^{(11)}$ transition (see Chapter 2) and a reset time of 10 μs was chosen which would reset the bath with a fidelity >99.9%. Since the transverse field was chosen in y basis, the resets were accompanied by $\pi/2$ carrier rotations in x basis which are about 1 μs each.

Initially, the entire experiment was carried out using the DMBC sequence without any resets(red trace in Figure 5.10), serving as a baseline energy calibration. As anticipated, the energy of the system remains constant over time. With the optimal parameters determined from numerical simulations, the DMBC protocol was implemented on a chain of three ions. The mid-circuit reset capabilities, discussed in the chapter 4, were utilized for performing the resets. As expected, when resets were introduced at times corresponding to $0.15\times 2\pi/J_0$ (depicted as vertical dashed lines in Figure 5.10), a clear signature emerges, indicating a decrease in the system's energy and approaching closer to the ground state energy. This demonstrates the effectiveness of the protocol in reducing the system's energy through dissipation in the reservoir. The decrease in energy could also be observed in the total energy of the ion-chain (system+reservoir).

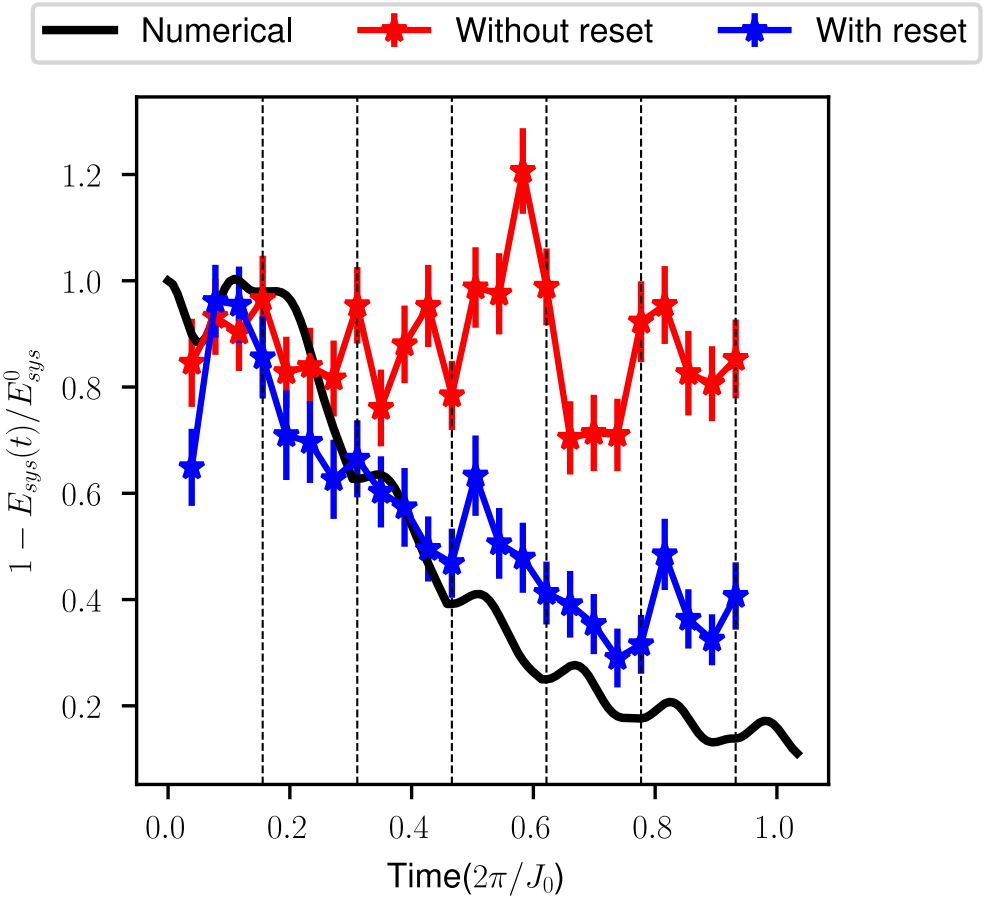

Figure 5.10: **Evolution of the Energy of the System During a DMBC Quantum Simulation:** Y-axis represents the system's energy scaled with the ground state energy of the system Hamiltonian. Black trace represents numerical simulations, blue trace shows experimental results. Vertical dashed lines indicate reset points. Red trace represents experimental results without resets. The quantity E/E_0 increases since the energies are negative. Each experiment is repeated 200 times, and the data displays the mean with error bars representing the standard error.

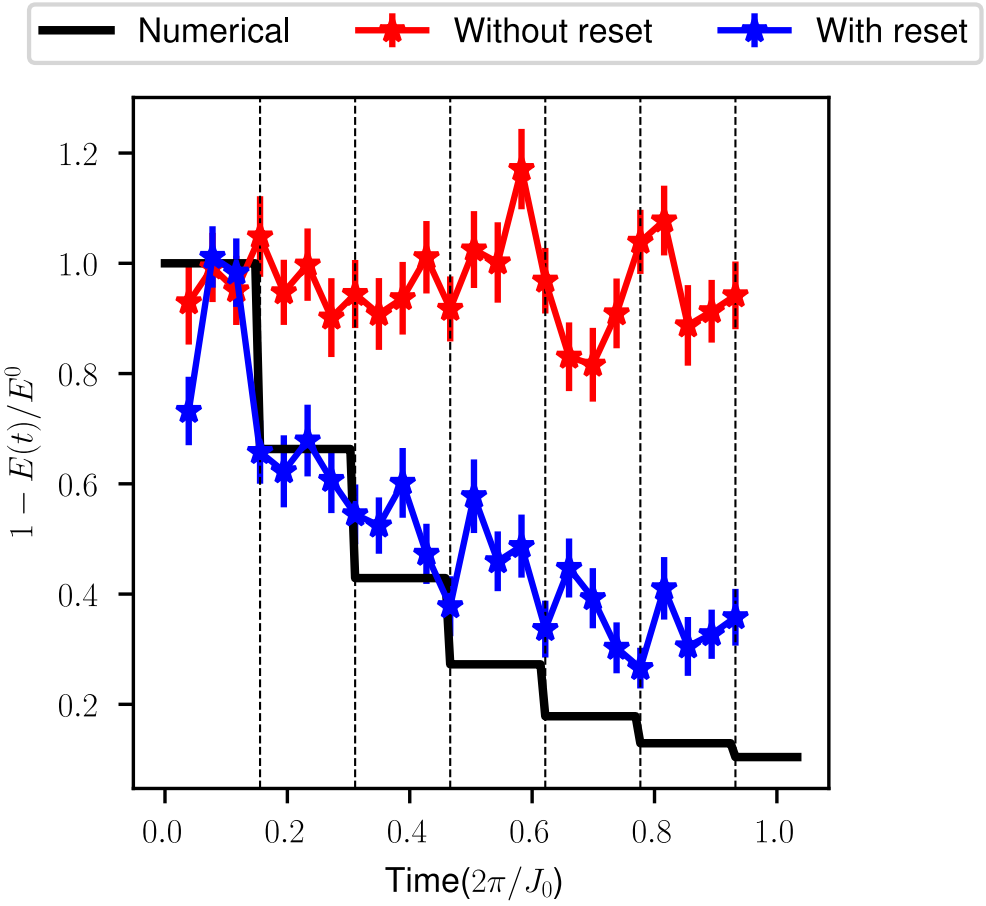

Figure 5.11: **Evolution of the Energy of the System+Bath During a DMBC Quantum Simulation:** Y-axis represents the total energy scaled with the ground state energy of the total Hamiltonian. Black trace represents numerical simulations, blue trace shows experimental results. Vertical dashed lines indicate reset points. Red trace represents experimental results without resets. Each experiment is repeated 200 times, and the data displays the mean with error bars representing the standard error.

5.6 Discussion

The previously mentioned implementation demonstrates the cooling of the system when the spin excitation is removed from the reservoir. This cooling phenomenon is primarily attributed to the strong many-body coupling between the reservoir and the system. How-

ever, it is important to consider the possibility that some of the cooling, even if partial, may be caused by the leakage of reset light into the system from the bath qubits. In Chapter 4, I presented evidence that the crosstalk from the reset operations to other ions in our system is quite low [71]. To validate or disprove this suspicion, we conducted another experiment where the same protocol was executed without the interaction Hamiltonian. In this experiment, we observed that the energy of the system remained constant. This confirmation provides further support for the many-body nature of this protocol.

The set of experiments and simulations mentioned above were conducted with the transverse field aligned along the y basis. However, I have numerically verified that it also functions effectively when the transverse field aligns with the z basis. To achieve this, resets should be executed along the z basis instead of the y basis. Consequently, the additional $\pi/2$ pulses before and after the resets become unnecessary. There are several experimental methods to generate the transverse field along the z basis. One approach involves employing an additional laser beam to induce an AC Stark shift [56], thereby altering the energy levels of the qubits and introducing an effective σ_z term into the Hamiltonian. However, this approach requires additional laser beams with precise intensity control, and precautions must be taken to ensure they are sufficiently detuned to avoid causing additional stimulated emissions that could disrupt the qubit states. Another technique we have utilized to address this issue is detuning the clock of the external oscillator. By shifting the clock oscillator away from the carrier transition frequency, we can create an effective σ_z field. This detuning in the clock oscillator causes the ion qubits to accumulate a time-dependent phase relative to one another, resulting in the emergence of the effective σ_z term in the Hamiltonian. To implement this technique in the experiment, it is crucial to track the accumulation of relative phase and ensure that all subsequent pulses after the Hamiltonian account for this accumulated phase.

The experiments and numerical simulations conducted so far have been focused on a Hamiltonian with positive coupling strengths, denoted as J_{ij}, which leads to an antiferromagnetic order within the system. On the contrary, if one intends to generate effective ferromagnetic coupling with J_{ij} being negative, they can achieve this by introducing a negative value for the detuning parameter μ. However, opting for such a strategy comes with its own disadvantages. Specifically, if the detuning is significantly large, the system no longer exhibits pure ferromagnetic behavior, as a few coupling terms become positive due to contributions from modes other than the center-of-mass (COM) mode. Another intriguing strategy for implementing many-body cooling within a ferromagnetic Hamiltonian involves utilizing the antiferromagnetic Hamiltonian itself. Considering that the highest excited state of the antiferromagnetic Hamiltonian corresponds to the ground state of the ferromagnetic Hamiltonian, one can prepare the system in the highest excited state of the

antiferromagnetic Hamiltonian. I have conducted numerical simulations that confirm that by resetting the spin states of the bath qubits to the excited state of the transverse field (instead of the ground state), one can employ the same protocol to guide the system toward its highest excited state.

In the above-mentioned set of experiments, it is noted that the system's energy does not quite reach the ground state as expected based on numerical simulations. There are several potential reasons for this deviation: Firstly, the presence of decoherence in the system could be a significant factor. Decoherence can disrupt the desired correlations, and it appears to stem from fluctuations in the intensity of the Raman beams. To address this issue, future experiments could focus on actively stabilizing the intensity of these Raman beams. Additionally, there might be unaccounted-for error terms in the Hamiltonian, such as a Stark shift term, which were not considered in the analysis. These unaccounted errors could introduce unexpected variations in the system's energy. Furthermore, it is worth considering the sensitivity of the system to its initial state. This sensitivity could contribute to the observed discrepancies in the comparison. To mitigate these errors, more precise calibrations of the system could be conducted in future experiments. Careful calibration should help minimize such discrepancies and enhance the performance of the protocol in approaching the ground state energy as expected.

While the protocol described above successfully brings the system close to the ground state, it is intriguing to explore the nature of this ground state further. The many-body order of the ground state is primarily determined by the relative strengths of two factors: the external magnetic field strength, denoted as B_0, and the coupling strengths between qubits, represented by J_{ij}. When $|B_0/J_0|$ is significantly large, the ground state of the system becomes trivial and aligns with the transverse field, lacking many-body order. However, as the ratio $|B_0/J_0|$ decreases, the ground state transitions into a state with either ferromagnetic or antiferromagnetic order, depending on the sign of J_0. In the simulations and experiments mentioned previously, where $|B_0/J_0|$ falls within the range of 1.5 to 2, the ground state closely resembles a product state, which is not particularly intriguing. It is worth emphasizing that as $|B_0/J_0|$ falls below 1, the ground state begins to deviate from this product state. This deviation signifies the emergence of more complex and interesting behavior in the ground state, making it an exciting area of exploration for future experiments. While it is feasible to conduct numerical simulations for lower values of $|B_0/J_0|$, realizing the ground state experimentally under such conditions demands even more meticulous calibration due to the heightened sensitivity of the protocol to experimental parameters. In my quantum simulation experiments where $|B_0/J_0| = 1$, I encountered partial success and was unable to reach the ground state as achieved in the previously mentioned experiments. In this parameter regime, the reset interval becomes particularly sensitive to the values of B_0 and

J_0. I attribute the failure to observe cooling in this regime experimentally to the inherent drift in the system and the challenges in maintaining precise calibrations throughout the experiments. Reaching the ground state for lower values of $|B_0/J_0|$ is intriguing because it allows us to explore more complex physics. Therefore, in future experiments, we should focus on improving our calibration to create more entangled ground states. This will open up opportunities to study a wider range of physical phenomena.

While the above protocol shows promising results, a significant advantage in solving the ground state would come with a large number of ions/qubits. I have demonstrated that this protocol works in numerical simulations with upto 7-8 ions. However, conducting numerical simulations beyond 10-20 ions becomes highly challenging using classical computers. This is where analog quantum simulations have the potential to excel in solving problems that are difficult for classical computers. In the above experiments, when resets needed to be performed, they were optimized within classical quantum simulations. However, this defeats the purpose if such classical optimization is required before the actual quantum simulation. Multiple strategies can be employed in such situations. One approach is to attempt simulations with small systems to identify patterns in optimal reset times and which ions to reset. Once these patterns are discerned in small systems, they can be extrapolated to a larger number of ions. If identifying such patterns proves difficult, another solution would be to analyze the problem analytically to determine optimal simulation strategies. While neither of these solutions guarantees results and may be as challenging as finding the ground state itself, they offer potential avenues for exploration. Another strategy involves performing local operations on the bath qubits to determine when the qubits need to be reset. Since the intuitive understanding is that resets should occur when the spin excitation is localized in the bath, conducting local measurements as the simulation progresses and executing reset operations when the spin excitation on the bath qubits reaches a certain threshold could be one of the strategies to implement with a large number of ions. As of now, I have not found a reasonable solution for any of the above-mentioned strategies through classical simulations. Further exploratory studies in the future will be necessary. The experiments and explorations mark the beginning of an exciting journey, filled with intriguing questions. One of these questions is about the different classes of simulations that can benefit from this approach; this aspect still holds much potential for exploration.

5.7 Summary

In summary, I have successfully established a dissipative many-body cooling protocol by manipulating dissipation in the bath/reservoir to reduce spin energy in a coupled system. Through quantum simulations supported by numerical results with calibrated experimental parameters, I have demonstrated the protocol's effectiveness in cooling the system towards its ground state. Additionally, preliminary quantum simulation experiments on a chain of three ions have shown a successful reduction in energy towards the ground state.

While our protocol brought the system close to the ground state, factors such as decoherence, unaccounted-for error terms, and sensitivity to initial states may have affected reaching the ground state. Calibration and error mitigation are essential for future experiments. Exploring the ground state at lower values of $|B_0/J_0|$ holds promise for studying complex physics, but this requires precise calibration and addressing experimental challenges. Scaling up the protocol for a larger number of ions or qubits remains a challenge. Potential solutions include pattern extrapolation, analytical analysis, and local measurements. Further research is necessary to fully realize these strategies and their potential advantages. Despite being a proof-of-principle experiment, this study highlights our system's capabilities in investigating various protocols involving engineered dissipation.

Chapter 6

The Blade trap

As mentioned in the introduction, our focus has been on parallelizing the construction of quantum simulators to attain a practical quantum advantage. In the previous chapters, I have elaborated on our utilization of the four-rod trap system to address various aspects, such as expanding the capabilities of quantum simulators and advancing towards error correction. This chapter delves into the meticulous process of designing and constructing a large-scale quantum simulator: blade-trap. Our primary objectives in this endeavor are to mitigate decoherence and enhance stability, thereby enabling more efficient and accurate calibrations.

The process of designing and building such an apparatus is highly challenging for a single person and requires collaboration. In this regard, I worked closely with my colleague PhD student Nikhil Kotibhaskar throughout the design and building process. Together, we tackled various challenges and contributed to different aspects of the project. Furthermore, as the project progressed, additional colleagues, Lewis Hahn, and Anthony Vogliano, joined in the efforts during the final stages of assembly and testing. Their contributions were invaluable in ensuring the successful construction of the building blocks of the apparatus and conducting thorough testing to validate their performance.

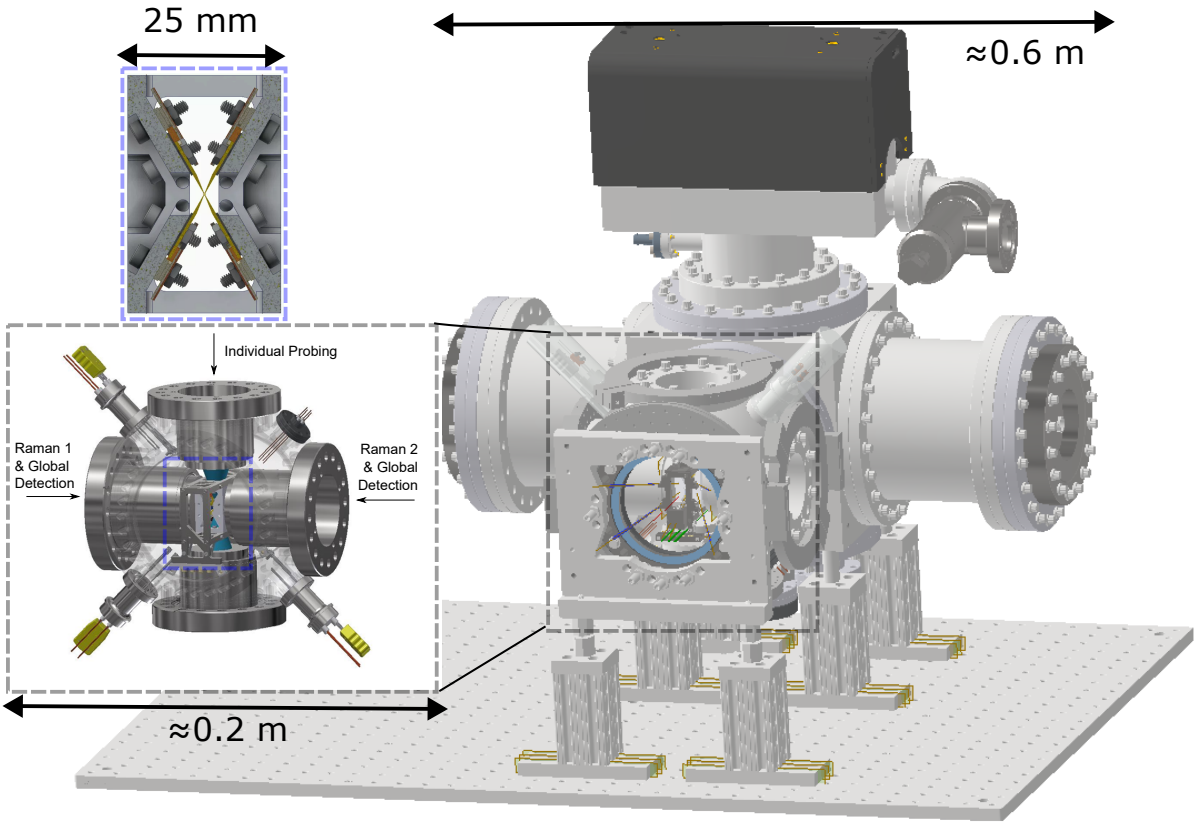

Figure 6.1: **Overview of Blade Trap Apparatus:** The CAD design of the entire blade trap vacuum chamber, positioned on an optical breadboard, is depicted on the right. The inset on the left provides a closer view of the science chamber, highlighting its internal components. At the core of the science chamber is the trap holder, where the ions are confined.

6.1 Overview

To build a futuristic trapped ion system capable of large-scale simulations with quantum advantage, several features and improvements need to be implemented:

- **Large number of ions:** The system should be designed to accommodate approximately 50 ions, enabling the simulation of complex quantum phenomena. By surpassing the limitations of classical computers in problems where full analysis becomes

intractable due to exponentially growing resource requirement (beyond 30 qubits), a quantum simulator with around 50 qubits has the potential to demonstrate quantum advantage through analog simulation.

- **Enhanced lifetimes and coherence times:** The trapped ions must exhibit extended lifetimes and coherence times. These characteristics are essential for enabling robust and accurate quantum operations, as they contribute to minimizing errors and maintaining the integrity of quantum states.

- **Independent control of spins and spin-spin interactions:** The system should allow for precise control of individual ion spins as well as interactions between them. This capability is vital for expanding the scope of quantum simulations, enabling the study of diverse quantum phenomena and the exploration of various simulation topologies.

- **High-efficiency detection and optical access:** Efficient and reliable detection methods are necessary for inferring the quantum state of the ion with high fidelity. Additionally, the system should provide optimal optical access, facilitating the addressing of individual ions and performing operations on them with high precision.

- **Capability for mid-circuit measurements and resets:** To support quantum error correction techniques, the system should be designed with the capability for mid-circuit measurements and resets. This functionality enables for error detection and correction within quantum circuits, improving the overall reliability and fidelity of the simulations conducted on the quantum simulator.

Figure 6.1 illustrates the CAD (computer-aided design) model of the blade trap apparatus. The assembly comprises the science chamber with all the attached vacuum peripherals. The science chamber (inset) is where the blade trap system, along with other internals, is housed. The cross-section of the blade trap geometry, including the holder, is depicted above the inset of the science chamber. In this chapter, I will present our approach to optimizing the design and fabrication process of the blade-trap system. The sections will follow a bottom-up approach, beginning with the trap itself, then moving on to the mechanical components that hold it, the internals of the system, and the optics that provide optical access. Finally, we will discuss the optimization of the ultra-high vacuum (UHV) system. One of the main challenges we encountered, which also consumed a significant amount of time, was the optimization of the ultra-high vacuum (UHV) assembly. The primary goal in designing the UHV assembly was to achieve the required pressure levels for conducting quantum simulation experiments with a large number of ions, specifically around 50 ions,

over extended durations. Maintaining low pressures in the chamber surrounding the trapping region is crucial to prevent collisions between the ion chain and background atoms. High-pressure conditions can lead to unwanted interactions, resulting in the melting of the ion crystal. Consequently, the entire ion chain would need to be re-trapped, adding additional overhead to the quantum simulation process.

In a setup like the four-rod trap, which typically operates at a pressure of 2×10^{-11} mbar, empirical estimates suggest that there may be one to two background collisions every 10 minutes for a chain of 10 ions. Extrapolating this estimate to a chain of 50 ions, the collision rate would increase by a factor of 5, resulting in a collision occurring every 1 to 2 minutes. Long-duration quantum simulation experiments, which include cooling, preparation, application of quantum gates, and high-fidelity measurements, can take up to 100 ms per iteration. To obtain meaningful statistical results, these experiments often require 100 to 200 repetitions, leading to an operation time of approximately 10-20 seconds. To study the dynamics of the target system, such measurements need to be conducted at various points during its evolution, which could add up to the complete experiment cycle lasting 20-30 minutes. During this time, it is crucial to prevent any background collisions. A background collision could melt the ion crystal and might require re-trapping the entire chain of ions.

While the process of trapping the ions itself may be relatively quick, on the order of up to 30 seconds, the system undergoes a cycle of changes where the trap potentials need to be relaxed before being ramped up again. This process takes additional time for the system to stabilize, and necessitates more calibrations, resulting in significant overhead in a quantum simulation. Therefore, to conduct experiments lasting up to 30 minutes, it is necessary to improve ambient pressures by approximately 15 to 30 times compared to 2×10^{-11} mbar. This sets a goal of achieving pressures in the range of 5×10^{-13} to 1×10^{-12} mbar at room temperature. Achieving such pressures in room temperature traps is indeed a challenging task. It requires meticulous optimization at the component level, where all chamber components must be made of materials with minimal outgassing. This additional requirement adds complexity to the selection of materials for various components, including electrodes, holders, electrical connections, and mounts for atomic sources.

Despite the well-developed field of vacuum science, finding the appropriate recipes and conducting necessary testing can be time-consuming. Each iteration and testing process demands a significant amount of time and attention to detail. While some research groups may not dedicate substantial time to optimizing vacuum performance, we have dedicated approximately 2 to 3 years to comprehending and preparing all the components of the ultra-high vacuum (UHV) assembly. These efforts were further complicated by the challenges imposed by COVID-19 restrictions. Additionally, we encountered challenges due

to malfunctions of various UHV components, such as ion pumps, which required multiple interventions (2-3 times) and resulted in extended lead times for repairs and replacements.

However, after enduring the tedious efforts, we have successfully achieved base pressures of less than 9×10^{-13} mbar in a chamber with all attachments and partially installed internals. It is important to note that this measurement represents an upper bound since we are limited by the X-ray limit of the gauge itself. In the subsequent sections, I will provide detailed descriptions of the design, fabrication, and assembly processes involved in constructing the blade-trap apparatus. These sections aim to offer a comprehensive account of the design choices made and also explore the simulations that guided the selection of critical dimensions. Furthermore, I will discuss the essential tests conducted to validate the effectiveness of the design. Throughout the development of each component, great care and attention were devoted to ensuring compliance with the specified requirements. As a result, I have gained valuable technical insights, which I will share at the conclusion of each section. It is my belief that these insights will prove valuable to future researchers engaged in the design of similar traps.

6.2 Trap geometry

The trap geometry is a crucial component in the design of an ion-trap quantum simulator as it determines the overall system's characteristics. For our simulator, we have chosen a macroscopic RF Paul trap geometry that fulfills the following key requirements:

- High optical access in all directions.
- Large trap frequencies ($\approx 2\pi \times 5$ MHz radial frequencies).
- Capability to trap a large chain of ions with near uniform spacing (50-100 ions).
- Multiple electrodes for precise trap control and minimal micromotion.
- Ease of fabrication.

Design details: To fulfill the above requirements, we designed a blade-style RF Paul trap, hence referred to as the "blade trap". This trap shares a similar geometry with the four-rod trap discussed in the previous chapter. However, instead of rods, segmented and tapered blade electrodes were employed to achieve a balance between high optical access and close proximity to the ions, thereby enabling high trap frequencies. This geometry allows for trapping a long linear chain of $^{171}Yb^{+}$ ions along the Z axis.

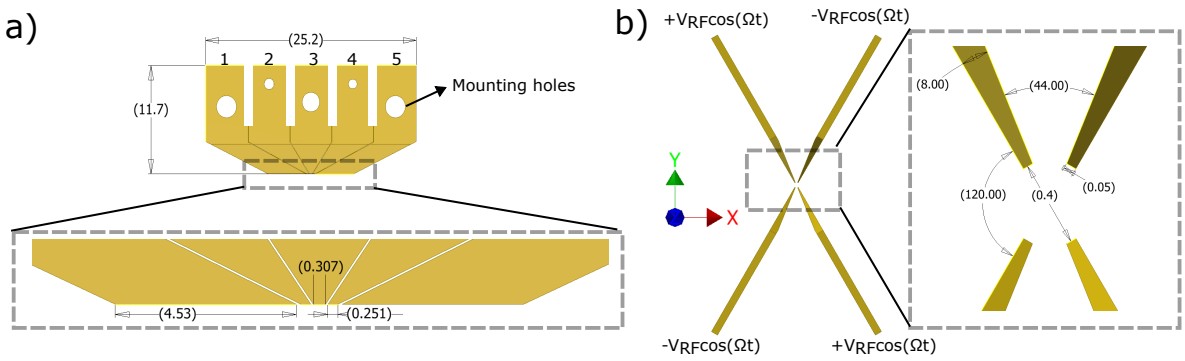

Figure 6.2: **Blade Trap Geometry:** (a) Top view of a single blade electrode that is segmented into 5 segments. The inset shows a close-up view of the electrode tip, highlighting the dimensions of the small segments. The ions are trapped below the central segment, facing the tip of the electrodes. (b) Cross-section view of the blade trap geometry, featuring 4 blade electrodes. The ions are trapped at the center of the cross formed by the blades. The inset displays the angle between the blades and the chosen tip dimensions. Length units are in mm, and angle units are in degrees.

Figure 6.2 illustrates the geometry of the trap. The four blades are arranged in a cross formation with ions trapped at the center of the cross. The diagonally opposite blades possess the same RF phase, while the remaining two electrodes are 180° out of phase. Each blade is divided into five segments, all of which experience identical amplitudes or phases of the RF voltage.

Our electrical connections allow the incorporation of an independently controllable bias voltage V_{DC}^{ij}, where $i \in 1, 2, 3, 4$ and $j \in 1, 2, 3, 4, 5$ represent the blade and segment indices, respectively. This feature enables us to engineer the anharmonic trap potentials along the z-axis, resulting in a more uniform ion chain compared to a harmonic trap such as the four-rod trap. In order to provide axial confinement in the trap, similar to the end caps in the four-rod trap, the end segments (1,5) primarily operate at a higher V_{DC} voltage. Consequently, it becomes possible to eliminate the use of end cap electrodes along the z-axis, thereby clearing the area for optical access by laser beams.

In the blade-trap design, the larger dimensions of the end segments play a crucial role in achieving axial confinement, leading to the generation of a sufficiently uniform harmonic potential along the z-axis, while effectively mitigating edge effects. To optimize the controllability of the axial potential and minimize the influence of electrode segments, comprehensive simulations were conducted, with the resulting dimensions depicted in Fig-

ure 6.2. The central segments introduce additional degrees of freedom, allowing further adjustments to the potential generated by the end segments. This flexibility enables the creation of potentials, such as quartic potentials, which facilitate the trapping of a linear ion chain with more uniform spacing [59]. Although the ideal gap between segments should be as small as possible, a reliable fabrication process necessitates a minimum gap size of 50 μm (as detailed in the Fabrication section below). Moreover, the blades are tapered at an angle of 8° to ensure that the electrode thickness facing the ion at the center remains approximately 50 μm. This configuration provides high optical access, facilitating efficient light collection and precise ion manipulation using beams traveling in the XY plane. Notably, the tapering is implemented on a single side, as opposed to both sides, simplifying the fabrication process while preserving high optical access.

The angles and the gap ($2R_0$) between the blades are chosen with considerations of higher optical access in both X, Y directions, the ability to create the required trapping frequencies ($\approx 2\pi \times 5$ MHz), and the creation of asymmetric trapping frequencies along X, Y directions while still being mechanically feasible to mount the blades with ease and apply other electrical connections. After optimization, we choose the angle between the blades to be 120° and R_0 to be $200\mu m$.

The blades are also equipped with multiple holes that facilitate their mounting and handling during the alignment process. Two holes of 2.4mm diameter each, on either side, facilitate mounting using an M2 screw. The central hole is used for a screw that acts as a pivot for rotations during the alignment process. The top $\approx$ 1mm holes are for pulling and pushing the blades for fine adjustments during the alignment process. With the above geometry, I have simulated that the electrode configuration could generate effective trapping frequencies of approximately $2\pi \times 5$ MHz in both X and Y directions for a V_{RF} of about 400 V.

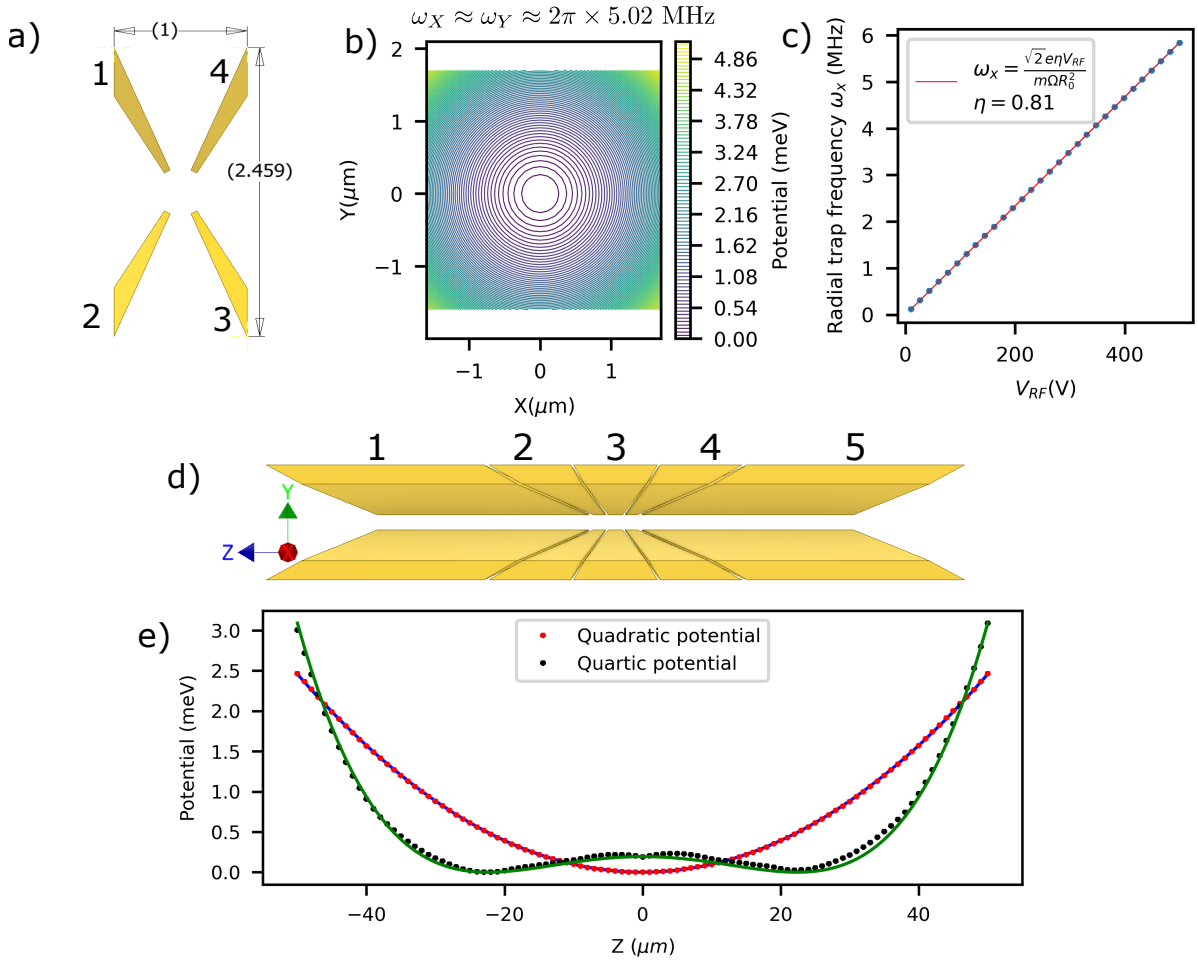

Figure 6.3: **Blade Trap Potential Simulation:** The figure illustrates the simulation of the blade trap potential, showcasing various aspects of the trap design and performance. (a) Shows the truncated geometry of electrodes used for COMSOL simulation. Length units are in mm. (b) 2D cross-section of the pseudopotential along the XY direction. (c) Calibration of ω_X as a function of V_{RF} and determination of the fudge factor η (see chapter 2). (d) Numerical simulation of the axial potential, demonstrating both quadratic and quartic potential forms.

Simulation: Unlike the four-rod trap, the blade-trap has a complex geometry, and I use numerical simulations to calculate the trap potentials and extract the trap frequencies in the X, Y, and Z directions. To simulate the potential created by the blade electrodes,

first, I truncate the whole geometry to a 1mm × 2.5mm representation in the XY plane. This simplifies the numerical simulation process, and since the part of the electrode far from the ion does not affect the trapping potentials, this is a valid approximation. Once truncated, the resulting geometry consists of 20 electrodes. The geometry is then imported to COMSOL Multiphysics to calculate the electrostatic potential created by each of the electrodes. Since using COMSOL to calculate potentials in every configuration of voltages could be time-consuming, I first calculate the basis functions from each electrode separately. To calculate the basis functions, I apply a voltage of 1V on one of the electrodes as a boundary condition and ground the remaining electrodes. The whole geometry is encapsulated in a cubical volume whose boundary is grounded for simulations. Once the boundary conditions are set, the whole geometry is meshed using fine settings in COMSOL. Additionally, a small cuboidal volume of dimensions (10μm × 10μm × 100μm) along the X, Y, and Z directions, respectively, is meshed with a resolution of less than 100nm.

Once meshed, the Laplace equation is solved numerically with the boundary conditions to calculate the static electric potential. The electric potential calculated using this method is exported to a text file within the above cuboidal volume with a resolution of 100nm. This procedure is repeated for all the electrodes to calculate the basis functions of each electrode U_{DC}^{ij}. The static potential U_{DC} for the whole geometry, given a specific configuration of electrode voltages, can be calculated from the superposition principle in electrostatics. The electric field (E_0) is calculated by taking the gradient of the generated potential. The effective pseudo potential can be extracted from

$$U_{PS} = \frac{eE_0^2}{4m\Omega^2}$$

where e is the charge of the electron, m is the mass of the Yb atom, and Ω is the drive frequency for the RF field.

Using the above-mentioned simulation procedure, the trap frequencies are extracted and optimized as a function of different geometric parameters such as R_0, angle between the blades, and blade segment sizes to meet the key requirements for the trap design. The radial trap frequencies ω_X and ω_Y are obtained by fitting the 2D cross-section of the calculated potential (Fig. 6.3b) with a 2D harmonic potential. For the chosen configuration and $^{171}\mathrm{Yb}^+$ ions, the trap produces approximately $2\pi \times 5.02$ MHz radial trap frequencies (ω_X and ω_Y) for a voltage of 430 V. Here, the trap drive frequency Ω is chosen to be $2\pi \times 35$ MHz. The degeneracy in ω_X and ω_Y is lifted, and the trap axis can be rotated by adding an additional DC potential to the electrodes. Furthermore, the simulations are utilized to calibrate ω_X as a function of V_{RF} (Fig. 6.3c) to determine the fudge factor $\eta = 0.81$ (see chapter 2). The fudge factor η represents the geometric correction factor of the trap geometry to the ideal hyperbolic geometry.

Figure 6.3e illustrates the axial potential as a function of position along the Z-axis. The numerical simulation demonstrates a quadratic-shaped potential with a trap frequency of $\omega_z = 2\pi \times 160$ kHz, generated by applying 2 V to the end electrodes (1,5). Additionally, a quartic-type potential can be generated to create a more uniform chain of ions.

In Figure 6.3e, the potential from numerical simulations is shown with specific voltage settings: $V_{DC} = 150$ V for end electrodes (1,5), $V_{DC} =$ -10 V for the side segments (2,4), and $V_{DC} =$ -0.5 V for the central segment (3). The green trace indicates that the numerically simulated potential exhibits a quartic potential form. This type of potential enables us to trap a chain of ions with more uniformly spaced ions compared to the quadratic potential.

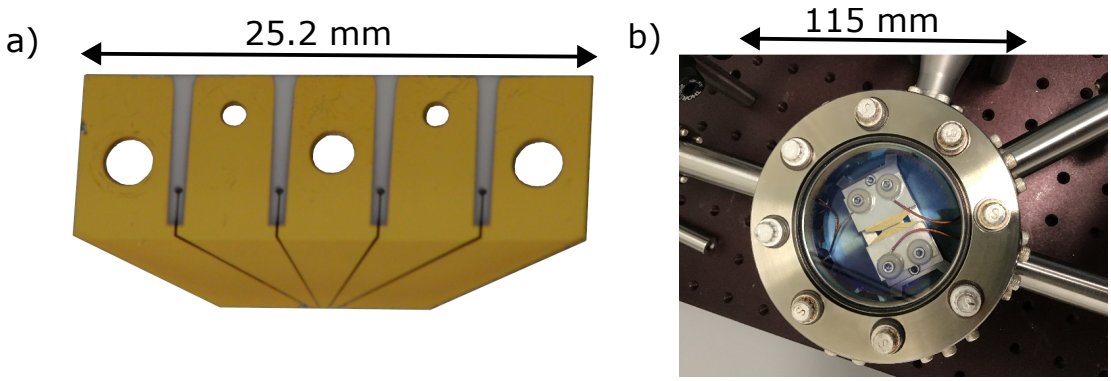

Figure 6.4: **Blade Electrode Fabrication and Testing:** (a) A photograph of the gold-coated blade electrode, illustrating the successful outcome of the fabrication process. (b) The setup for testing the blade electrodes, highlighting the positioning of two electrodes within a vacuum chamber to evaluate potential failures under high-voltage conditions.

Fabrication: The blade electrodes are fabricated using polished Alumina ceramic due to its desirable properties, including low RF loss, high thermal conductivity (compared to other ceramics), the ability to achieve a mirror-like surface finish, low thermal expansion, and high dielectric strength. Although Alumina is not easily machinable, the availability of highly polished Alumina wafers of varying thicknesses in the market has facilitated the process. Through advancements in laser machining techniques, we were able to precisely machine[1] intricate patterns in 2D on the Alumina wafers. The laser machining process allowed us to precisely machine the required features along the length and breadth of the blade, such as the overall shape, segments, and mounting holes, with a tolerance of $\pm$ 25 μm. However, laser machining could not achieve the desired 50 μm chamfer on the edges

[1]Centerline Technologies, LLC

of the blade. Chamfering the edges is crucial as this surface comes into close proximity with the ions. To address this, we utilized a wafer polisher available in our Nano fab facility at IQC. The chamfering process was meticulously carried out by my colleague, Nikhil Kotibhaskar. It involved mounting the blade at a shallow angle of 8 degrees and conducting careful polishing to create the desired chamfered edges. This process ensured the precise shaping of the blade electrodes while maintaining the necessary surface quality.

To define the electrodes on the chamfered blades, a coating of approximately 1 µm of gold was applied. This gold coating process was carried out using RF sputtering with argon buffer gas, which took place in-house at the IQC Nano Fab facility. The procedure was performed by Nikhil Kotibhaskar. During the gold coating process, a mask was utilized to ensure that the individual segments of the electrodes remained electrically isolated and prevented any unintended short circuits between them. By employing RF sputtering and employing a mask to maintain electrical isolation, we achieved the necessary electrode definition on the chamfered blades, enabling effective trapping and manipulation of ions in the blade trap design. Figure 6.4a showcases a photograph of the gold-coated blade electrode, illustrating the final result of the fabrication process.

Testing: One common source of failure for the blade electrodes, as reported by other research groups, is the flaking of the gold coating at high operating voltages. Another issue arises from dielectric breakdown at high voltages, which leads to electrode shorting. Additionally, the electrodes can experience high heating, causing the spacing between them to change, and in severe cases, mechanical failure. To address these concerns, we conducted tests to assess the potential failure of the blade coating at high voltages. In this particular test, we positioned two blade electrodes with their tips facing each other at a distance of approximately $2R_0$. These electrodes were mounted on a customized fixture within a vacuum chamber, as shown in Figure 6.4b. The chamber housing the blades was maintained at a pressure of 1×10^{-5} mbar throughout the tests. Initially, we applied a high DC voltage, gradually ramping it up from 100V to 1.8kV over a period of approximately 15 minutes. Using an in-vacuum thermocouple, we measured the temperature of the blades and confirmed that it did not exceed room temperature. After completing the test, we visually inspected the electrodes and found that the gold coating remained intact, with no visible signs of flaking or dielectric breakdown.

In another test, we subjected the electrodes to an oscillating voltage at around 40 MHz with an amplitude of approximately 1 kV using a helical resonator. Visual inspection did not reveal any changes to the gold coating. However, the overall temperature of the system increased to 130°C within two hours. We attribute this temperature rise to RF losses in the test mounting structure, which is constructed from ceramic MACOR known for its poor thermal conductivity and higher loss tangent (as indicated in Table 6.1), along with

inadequate thermal conductivity between the mounting groove grabbers and the vacuum chamber. In conclusion, our tests demonstrated that our electrodes could withstand high RF and DC voltages, nearly double the maximum operating voltages, without experiencing breakdown or failure.

Technical insights: During the design, fabrication, and testing of the blade electrodes, we have gained several technical insights. Firstly, as mentioned previously, incorporating a single-sided chamfer in the blade design has proven to be advantageous. This chamfer not only makes the machining process easier but also enhances the repeatability of the blades. Additionally, the inclusion of additional holes for alignment purposes has greatly facilitated the handling of the blades, minimizing the risk of scratching the gold coating surfaces. Furthermore, choosing to carry out the blade chamfer and gold coating in-house has led to higher-quality polished blade tips and reduced manufacturing costs. This approach has also made the revision process more streamlined and efficient, allowing for easier modifications and improvements to the blade electrodes.

6.3 Trap holder

The trap holder serves as the mechanical support for the blade electrodes and plays a critical role in ensuring the stability of the trap. In designing our trap holder, we have prioritized the following requirements:

- Robust stability for the trap.
- High optical access in various directions.
- Easy electrode alignment and electrical connections.
- Ease of machining with tight tolerances.
- Ultra-high vacuum (UHV) compatible material with zero porosity.
- Desirable properties such as electrically insulating, low thermal expansion, high thermal conductivity, and low RF loss.

Design details: Figure 6.5 illustrates the geometry of the trap holder that I have designed to meet the above requirements. The holder is constructed from a ceramic Shapal material with dimensions of 25.1mm x 39mm x 40mm. The trap holder provides four

surfaces for mounting the blades, defining the angle and geometry of the trap. The mounting holes (2.4 mm diameter) allow for easy blade installation without obstructing optical access. These holes also enable fine adjustments during alignment, offering sufficient degrees of freedom while securely mounting the blades. However, the degrees of freedom provided are limited to adjustments within the plane of the blades, without freedom in the perpendicular direction.

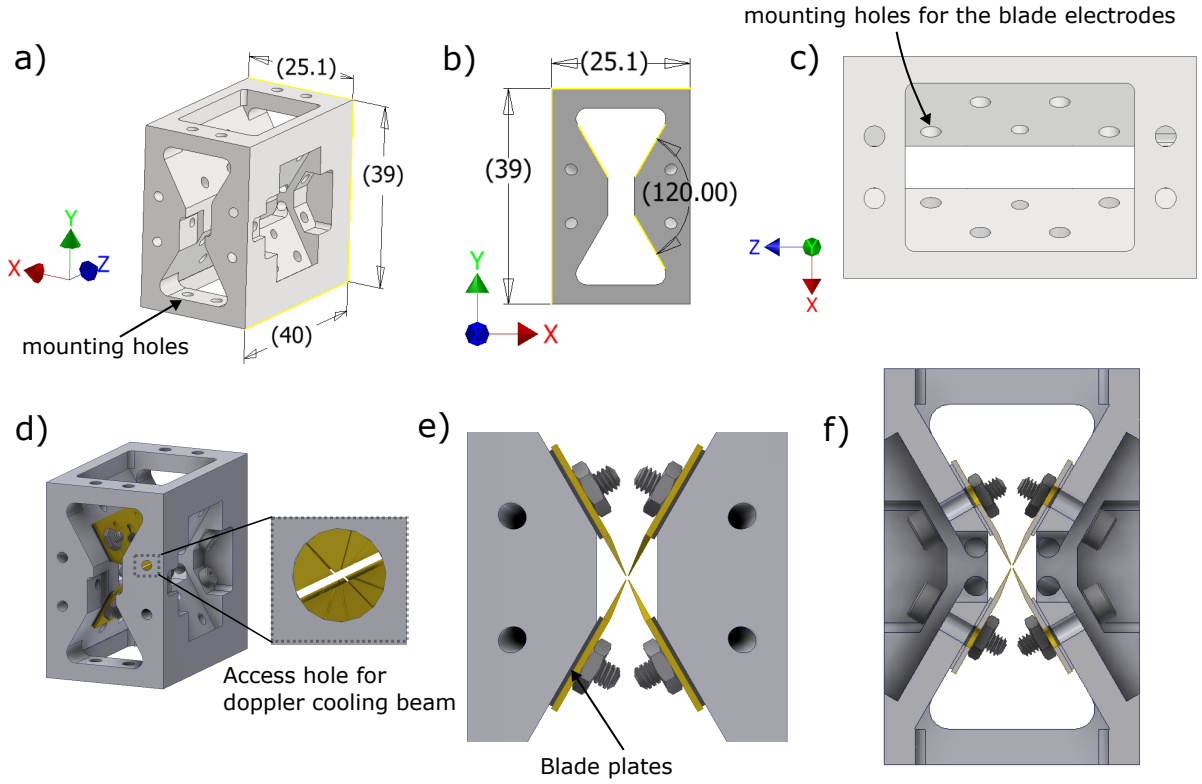

Figure 6.5: **Blade Trap Holder Design:** This figure illustrates the geometry of the trap holder, which is designed using ceramic Shapal material. It features four mounting surfaces for blades, allows for easy installation and alignment adjustments through mounting holes, and incorporates a blade plate for perpendicular adjustments of the blades. Length units are in mm, and angle units are in degrees.

To address the need for perpendicular adjustments and avoid relying solely on trap holder machining tolerances, an additional ceramic plate, referred to as the "blade plate,"

is placed between the blades and the holder. The thickness of this blade plate can be varied to adjust the position of the blades in the perpendicular direction. The holder design ensures high numerical aperture clearance from the top (Y) and side (X) directions. Furthermore, four access holes (referred to as "111" holes) with a diameter of 2mm are incorporated, allowing the doppler cooling beam to enter at a non-trivial angle. The axis of this hole makes an angle of 27.57 degrees with the Z-axis, with projections of (0.41, 0.22, 0.89) in the X, Y, and Z directions, respectively. This hole facilitates efficient cooling in all trap axes by providing the doppler cooling beam with projections in all directions. Machining the access hole with the required specifications presents a complex challenge during fabrication. It is optimized for ease of machining, enabling all critical geometries to be machined in a single setting using a CNC process. Furthermore, the holder incorporates provisions for mounting two temperature sensors/thermocouples to monitor the holder's temperature when operating in a vacuum environment.

Additionally, the holder design facilitates easy mounting of the blades' electrical connections and access to other laser beams. The blade electrodes are equipped with electrical connections using four PCBs (printed circuit boards)[2], which are then connected to the feedthrough using Kapton wires. The connections between the blade electrodes and the PCBs are established using high-performance electrical connecting pins known as Fuzz buttons[3], which offer superior high-frequency connections compared to simple surface-to-surface contacts.

Fabrication: Ceramics, being electrically insulating, possess favorable properties that align with our mentioned requirements. Traditionally, MACOR has been the preferred ceramic for machining due to its good machinability and the availability of vendors capable of achieving tight tolerances. However, MACOR is known for its high RF losses, indicated by the loss tangent, and poor thermal conductivity (see Table 6.1). These properties can lead to significant heating of the blade holder and potential dimensional changes during operation.

In Table 6.1, I have listed other UHV-compatible ceramics. Among them, Aluminum Nitride exhibits excellent properties, but it is notoriously challenging to machine, especially for complex geometries as discussed earlier. Shapal, on the other hand, is a machinable ceramic that consists of Aluminum Nitride doped with Boron Nitride, offering the combined benefits of machinability and good properties similar to Aluminum Nitride. Shapal is highly thermally conductive, giving it a metallic feel when touched with bare hands. We had the trap holder machined by Precision Ceramics USA, leveraging the machinability of Shapal.

[2]Rogers Corporation : RO4350B
[3]Custom Interconnects, LLC : 88-040100

While Shapal is relatively easier to machine, it still requires design optimization to achieve tight tolerances for critical dimensions. The surfaces where the blades are mounted, including their relative angles and hole positions, are the most crucial dimensions that require precise machining. The process of designing does not always guarantee machinability, and prototyping using methods like 3D printing can be deceptive since CNC machining and 3D printing operate differently.

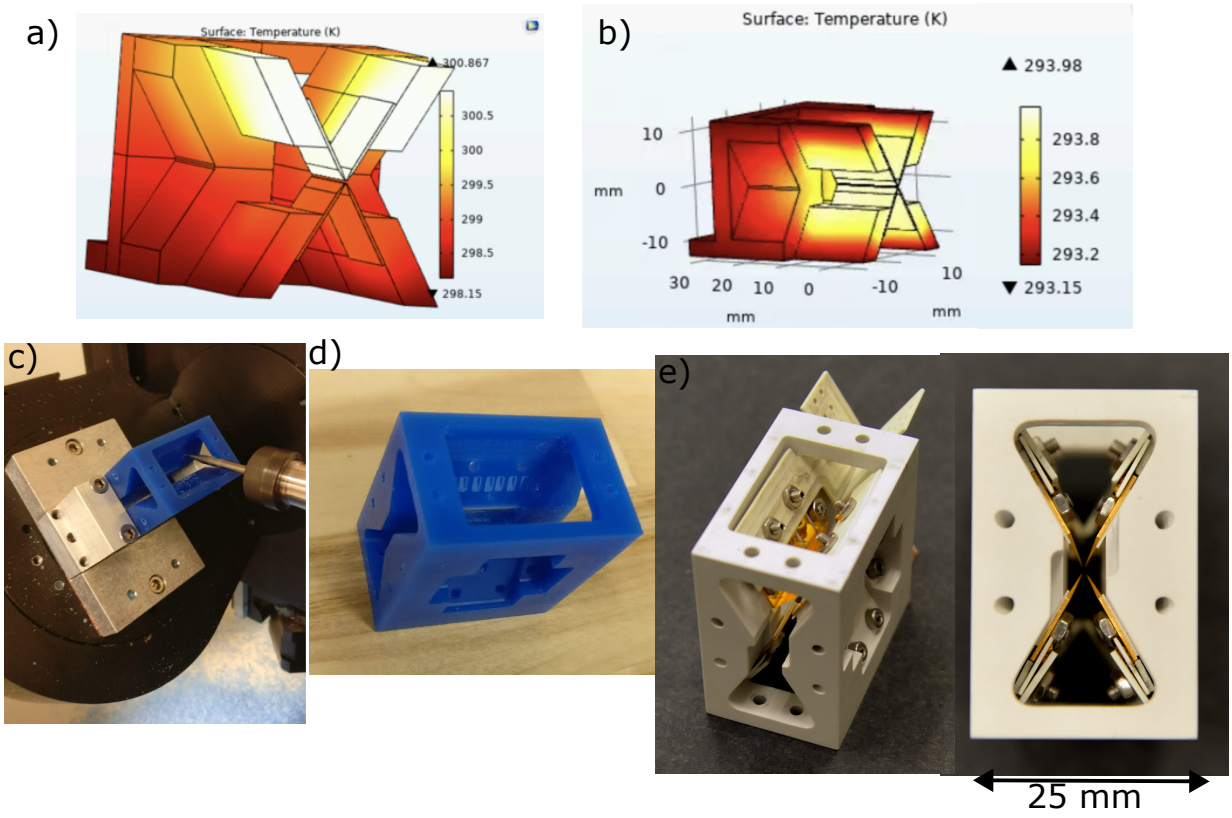

Figure 6.6: **Blade Trap Holder Fabrication and Testing:** (a) Temperature profile with a boundary condition applied only at the bottom of the holder, displaying an asymmetric temperature gradient along the Y-axis. (b) Temperature profile with boundary conditions applied to both the top and bottom of the holder, resulting in a symmetric temperature distribution. (c-d) Prototype plastic blade holder machined using an in-house 5-axis CNC machine to optimize design tolerances and achieve better machining results. (e) Machined ceramic holder with mounted blades and printed circuit boards.

To gain a better understanding and optimize the design with machinability in mind, I machined a prototype plastic blade holder (see Fig.6.6c-d) using an in-house 5-axis CNC machine. Programming the paths for the CNC machine allowed me to realize how certain design choices could be modified to achieve better tolerances. One insight I gained during this process is that tight tolerances can be achieved between features machined in a single orientation axis, without the need for part removal and remounting. This led me to modify the design so that the surfaces holding the blades could be machined in a single orientation along the Z-axis.

Further optimizations in the design resulted in increased machining ability with tolerances smaller than $\pm 50 \mu m$ and reduced machining costs. The cost of machining the part ended up being only around $1000 USD, significantly lower compared to other designs that could have cost an order of magnitude more. Fig. 6.6e shows the machined ceramic holder with the blades and printed circuit boards (needed for electrical connections) mounted, showcasing the successful fabrication of the trap holder.

Table 6.1: Holder Ceramic Material Properties

Holder Material	Thermal Conductivity (W/m·K)	Loss Tangent (10^{-4})	Thermal Expansion (10^{-6}/K)	Dielectric Strength (kV/mm)
Alumina	30	1	8.4	31.5
Sapphire	40	0.2	7.8	48
Macor	4.6	70	9	45
Aluminum Nitride	180	5	4.5	17
Shapal	92	10	4.3	65
Boron Nitride	80	12	2	79
Fused Silica @ 25°C	1.38	< 10	0.55	30

Simulation: To accurately estimate the heat generated by the trap holder, including the blades, and assess whether heat dissipation is efficient and if the holder's temperature increases during operation, we conducted simulations using COMSOL. These simulations were performed by Gaurav Tathed, one of our undergraduate students, under my guidance. To simplify the model and facilitate the meshing process, we removed small features from the design. Additionally, we applied symmetry by cutting the model in half along the Z-axis, as symmetry should not affect the results.

In the simulations, we applied a temperature boundary of 25°C to the bottom of the holder, representing the interface where the holder is mounted to the bridge structure (refer to the Bridge Holder Assembly section below). When applying an RF voltage with an

amplitude of 500V oscillating at a frequency of 35 MHz, we observed a temperature increase of a few degrees, as shown in Figure 6.6a. Notably, the temperature profile exhibited asymmetry along the Y-axis.

We realized that this asymmetry was due to the boundary condition being applied only at the bottom. To address this issue, we added a boundary condition of 25°C to the top of the holder as well, resulting in a symmetric temperature gradient, as depicted in Figure 6.6b. These simulation results prompted us to modify the bridge holder assembly that connects the trap holder to the vacuum chamber, aiming to enhance thermal conductivity and mitigate any asymmetry or undesired temperature gradients.

6.4 Bridge holder assembly

The bridge holder assembly serves as the structural support for the blade trap holder, connecting it to the vacuum chamber. It plays a crucial role in setting the reference of the trap to the vacuum chamber, which is essential for aligning all external optics and referencing them to the chamber. Additionally, the bridge holder assembly facilitates the integration of other internal components within the vacuum chamber, such as atomic sources and electrical connections. The following are the requirements for the bridge holder assembly:

- Structural rigidity and vibration dampening
- Fine adjustment capabilities
- Access for electrical connections and atomic sources
- Unobstructed optical access
- Efficient thermal connectivity for heat dissipation

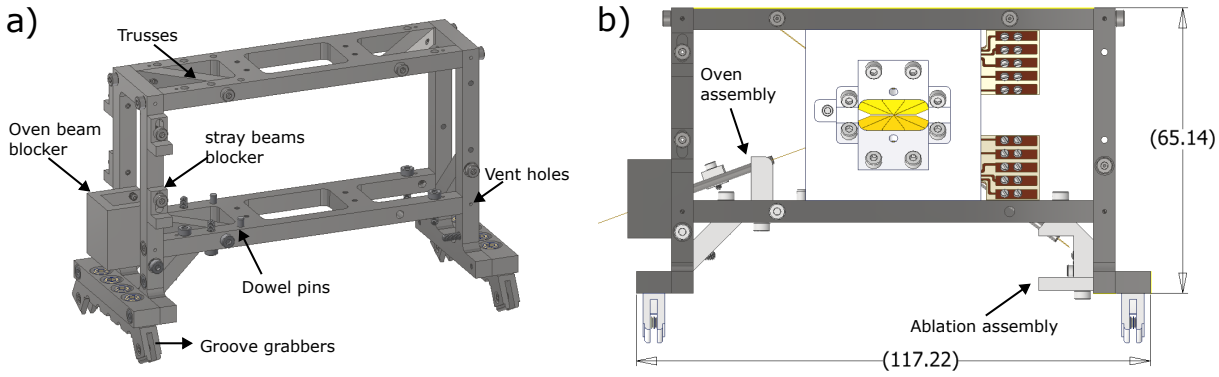

Figure 6.7: **Blade Trap Bridge Holder Assembly:** The designed bridge holder assembly features secure attachment to the vacuum chamber, precise positioning using mounting screws and dowel pins, and enhanced structural rigidity through trusses for uniform thermal conduction and stability. Length units are in mm.

Design details: Fig. 6.7 depicts the designed bridge holder assembly that fulfills the above requirements. The bridge holder is positioned on top of the groove grabbers, which are securely connected to the grooves of the vacuum chamber. To support the trap holder, mounting screws and dowel pins are utilized, providing a precise reference during installation. The bridge holder ensures uniform thermal conduction from the trap holder by establishing contact from both the top and bottom surfaces. Structural rigidity is enhanced through the incorporation of trusses at various locations, promoting stability. Additionally, the bridge holder accommodates the integration of the oven and ablation atomic sources, which are strategically mounted on either side of the trap holder. This arrangement grants access to the atomic beams and maintains unimpeded optical access along the X, Y, and Z axes. To mitigate stray optical and atomic beams, beam blockers are implemented. The bridge holder offers sufficient degrees of freedom to facilitate fine adjustments of the trap holder's position relative to the chamber, enabling precise alignment. Furthermore, employing blind holes or vent holes to prevent potential virtual leaks that may compromise the vacuum integrity.

Fabrication: The bridge holder is machined using stainless-steel 316L, chosen for its non-magnetic properties compared to other grades of stainless-steel. The machining process was carried out by the in-house machinists at Science Technical Services (STS). To ensure optimal machinability, the entire assembly is divided into multiple components. The design of the trusses, in particular, involves separate cross pieces attached to the bridge using screws. This design choice not only facilitates ease of machining but also provides

improved vibration dampening properties.

6.5 Atomic sources

$^{171}Yb^{+}$ ions are loaded in our trap by singly ionizing neutral Yb atoms. To achieve this, a flux of neutral atoms is generated from a chunk of Yb metal and subsequently ionized through a two-step process using 399nm and 369nm lasers (refer to Chapter 2 for detailed information). To create the required neutral atom beams for trapping the ions, we employ various mechanisms, including both thermal oven-based and ablation-based atomic sources, each offering distinct advantages. The requirements for designing the atomic sources are as follows:

- Provide a flux of atoms to the trap center on demand as quickly as possible.
- Ensure decent collimation of the atomic flux to prevent unintentional coating of other trap components.
- Allow rapid on/off switching of the atomic flux to avoid increasing chamber pressure.
- Ensure the atomic beam is perpendicular to the first ionization laser beam to prevent Doppler broadening of the ionization transition, which is necessary for good isotope-selective atom loading.
- Provide optical access (for ablation-based source) for the ablation beam to reach the target Yb metal chunk.
- Accommodate the mounting of multiple sources.
- Enable the trapping of approximately 50 isotopically pure ions with a high probability without inadvertently trapping ions of other atomic species.

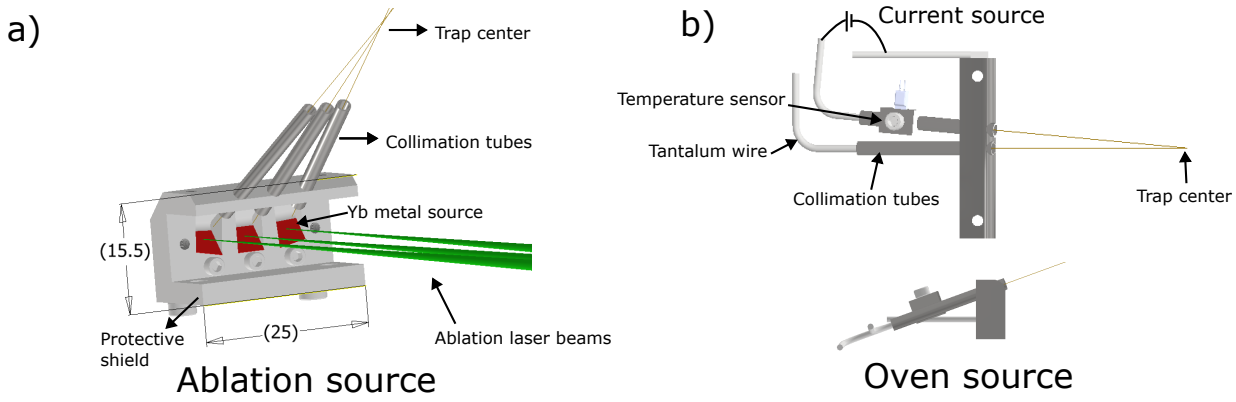

Figure 6.8: **Blade Trap Atomic Sources:** (a) Ablation mounts feature a surface for mounting metal sheets, with the normal pointing toward the trap center, enabling precise laser ablation. (b) Oven-based atomic sources consist of stainless-steel tubes heated to 100-200°C, containing Yb metal chunks placed near tantalum wires. These sources are oriented toward the trap center in the YZ plane. Length units are in mm, and angle units are in degrees.

Design details: The oven-based atomic source (Fig. 6.8b) consists of a stainless-steel tube with an inner diameter (ID) of 1.5mm and an outer diameter (OD) of 2.0mm. The oven tube is connected to the bridge holder using a stainless-steel arch. On the opposite side of the tube, a tantalum wire is connected. High current is passed through the tantalum wire and the stainless-steel arch to heat the oven tube to temperatures ranging from 100-200°C. Inside the tube, a chunk of Yb metal is placed closer to the tantalum wire, where the oven is hottest. The length of the tube is selected to provide necessary collimation to the trap center. This design allows for the use of two independent ovens, one for natural source Yb and another for an enriched source with the 171Yb isotope. The angles of both oven tubes are oriented towards the center of the trap in the YZ plane.

On the other hand, the ablation mounts (Fig. 6.8a) feature a surface where a target, typically in the form of a metal sheet, is mounted. The normal to this surface is pointed towards the center of the trap. The mount provides access for a tightly focused laser beam (1550nm) to illuminate the Yb metal sheet. The focused beam ablates the surface of the substrate, creating a plume of atoms that are collimated through stainless-steel tubes pointing towards the trap center. These stainless-steel tubes have the same diameter as those used for the oven. Additionally, a protective shield is incorporated to prevent stray atom flux from coating the optical windows located below the ablation mount.

Simulation: Yb metal naturally occurs in various stable isotopes with masses rang-

ing from 170 to 176. However, for our quantum simulator, we are primarily interested in trapping $^{171}Yb^{+}$ ions. Unfortunately, naturally occurring Yb metal has a low abundance of the desired 171Yb isotope (14%) and is predominantly composed of 174Yb (34%). This presents challenges in trapping isotopically pure chains of ions, as accidentally trapping other Yb isotopes hampers quantum simulations due to their different transitions compared to $^{171}Yb^{+}$ ions. Selectively removing the unwanted ions from the trap becomes particularly difficult, often requiring the complete dumping of all ions by turning off the trap potentials and restarting the trapping process. This task becomes extremely challenging when attempting to trap a large number of ions (e.g., 50) using natural abundance.

To address this issue, the first step is to procure a source of Yb metal that is enriched in the 171Yb isotope. We obtained a source with 95% Yb171 and 5% of the remaining isotopes. Even with a 95% probability of trapping Yb171, the probability of trapping 50 $^{171}Yb^{+}$ ions drops to less than 0.1%. Therefore, laser frequency selectivity is employed to achieve even better isotope selectivity. Figure 6.9c shows the fluorescence spectrum of neutral Yb atoms taken from Ref. [54], demonstrating the isotope shifts of different ions. However, targeting a single species of Yb can be challenging due to the Doppler broadening of these profiles at high atom temperatures.

To efficiently target a single species without the Doppler broadening effect, the ionization beam needs to be perpendicular to the direction of the atomic beam. The required geometry for this setup is illustrated in Figure 6.9a. Numerical simulations were performed to determine the necessary requirements for an atomic beam flux with a divergence of approximately $\theta = 10^{\circ}$, oriented perpendicular to the ionization beam (with a tolerance of $\pm 5^{\circ}$). The simulation results shown in Figure 6.9b indicate that with a flux of atoms at 300°C, a chain of 50 ions can be trapped with a high probability approaching 1 using the enriched Yb source compared to natural abundance.

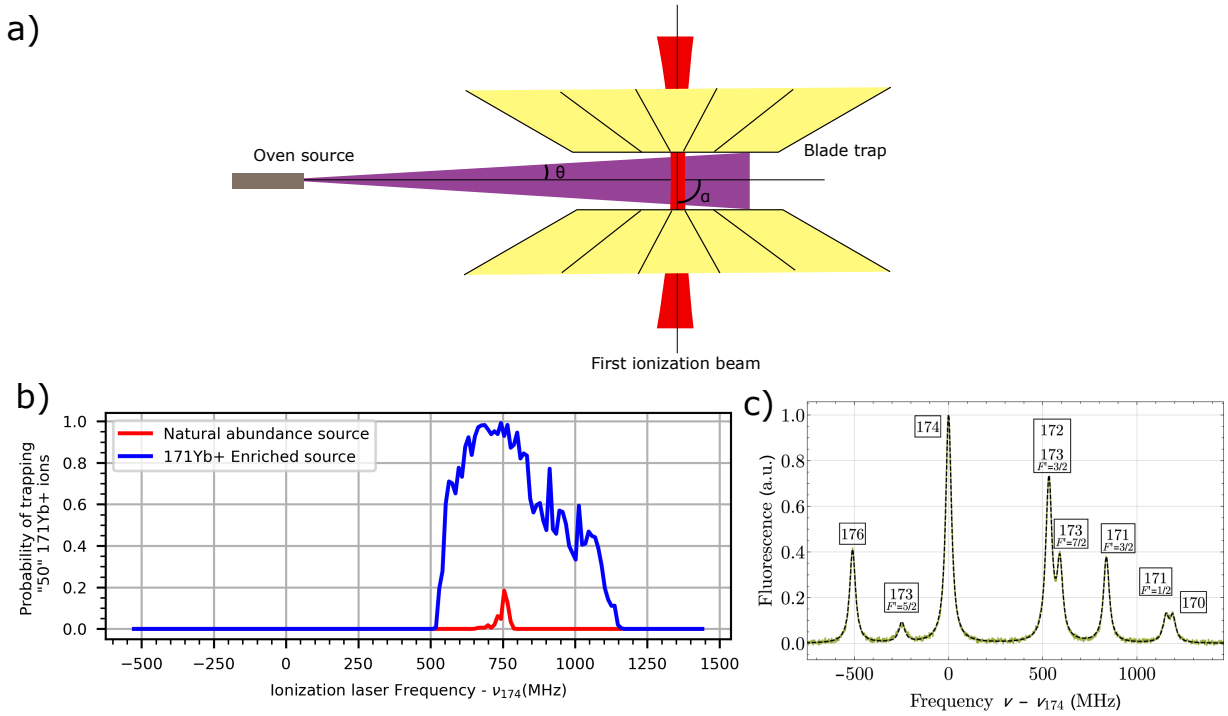

Figure 6.9: **Blade Trap Atomic Sources Isotope Selectivity Simulation:** (a) A schematic representation of the required geometry for efficiently targeting a single species of Yb atoms in an atomic beam using perpendicular ionization. (b) Numerical Monte Carlo simulation results illustrating the probability of trapping a chain of 50 ions as a function of ionization laser frequency. The enriched source with 95% Yb171 shows significantly higher probability compared to the natural abundance source at 300°C. (c) Fluorescence spectrum of neutral Yb atoms demonstrating isotope shifts, data taken from Ref. [54].

Fabrication: Both the oven mount and the ablation mount are machined from SS316L stainless-steel. Machining the holes for the collimation tubes and the surfaces for mounting the ablation target posed a challenge due to the non-trivial angles involved. To overcome this, the assembly was divided into multiple pieces, allowing clearance for the machining tool to reach the required areas. One of the significant challenges encountered during this project was procuring the enriched Yb metal source. Initially, the only vendor available was the National Isotope Development Center at Oak Ridge National Laboratory. However, during the project's early stages, they had ceased selling the enriched metal. This prompted us to search for alternative vendors worldwide. While we found vendors offering small amounts of enriched Yb at exorbitant prices exceeding $50,000 USD and lead times of over

a year, after several months of waiting, Oak Ridge National Laboratory agreed to provide us with the enriched source.

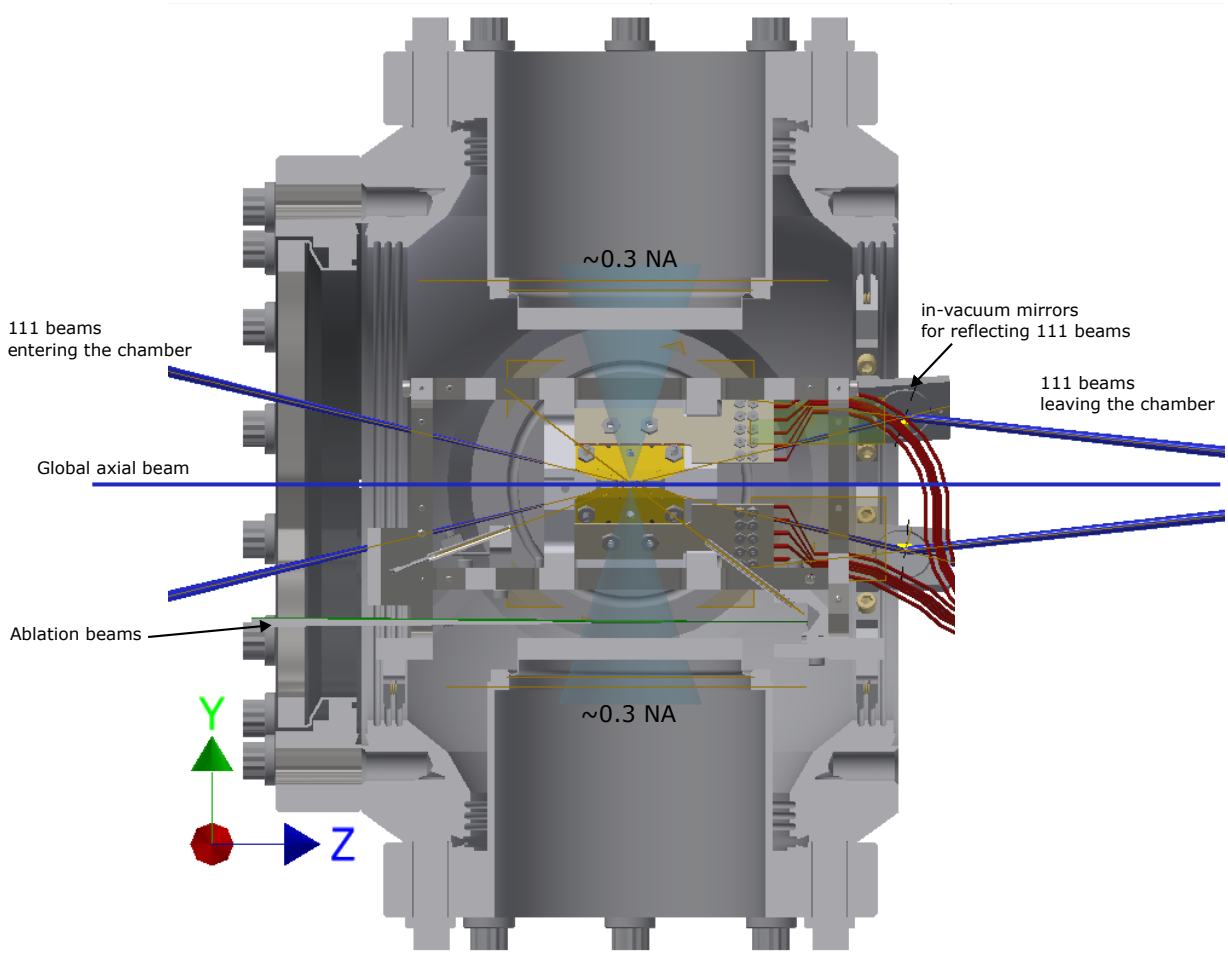

Figure 6.10: **Blade Trap Optical Access YZ Cross-Section:** This figure provides a side view of our science chamber, highlighting the optical access configuration along the YZ plane.

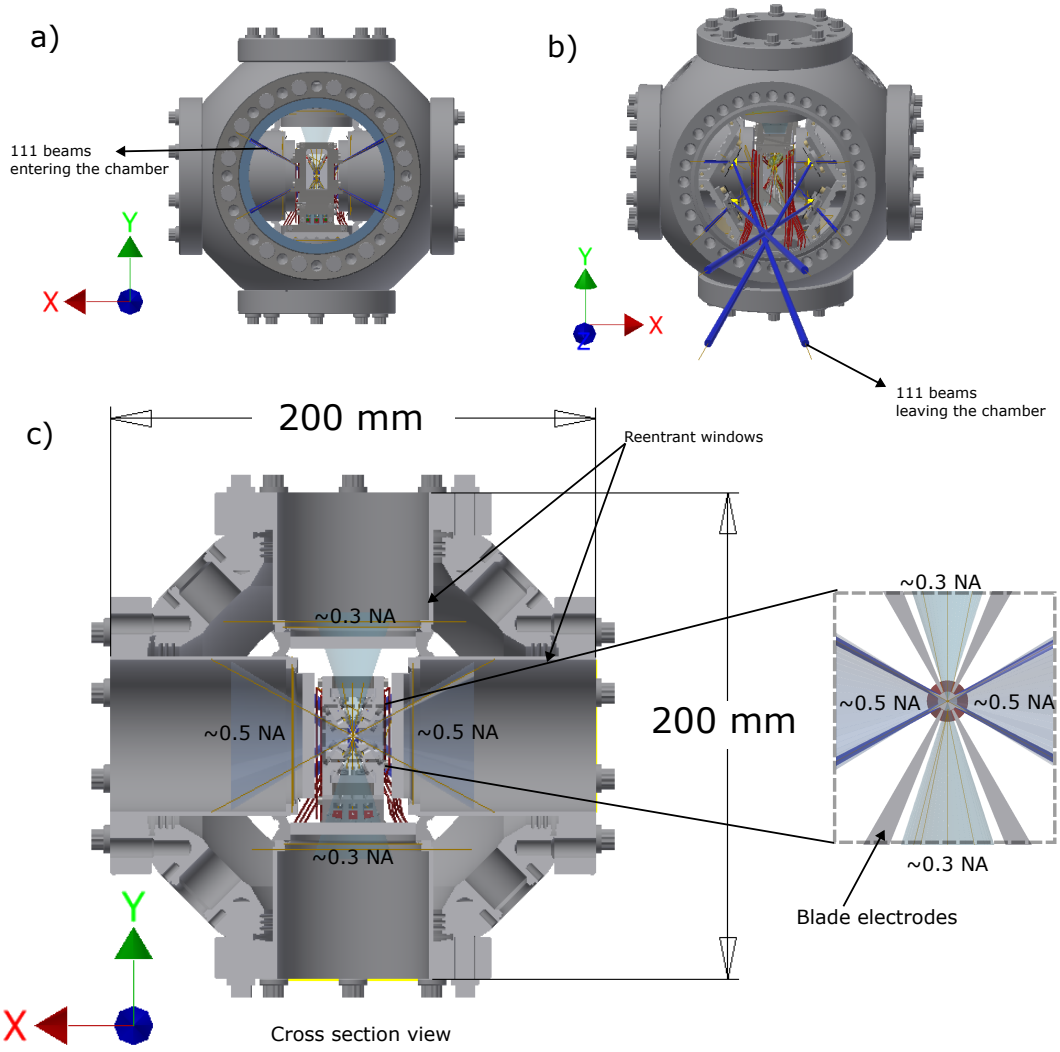

Figure 6.11: **Blade Trap Optical Access XY Cross-Section:** This figure presents a front view of our science chamber, highlighting the optical access configuration along the XY plane. The re-entrant windows along the X-axis allow for objective placement outside the vacuum chamber, enabling imaging and addressing of the trapped ions. The inset in panel (c) illustrates the limitation imposed by the blade trap holder on the numerical aperture (NA) in the Y direction. Length units are in mm, and angle units are in degrees.

6.6 Optical access

The optical access to the trapped ions is a crucial consideration in the overall system design. The following requirements are essential for achieving high optical access:

- High Numerical Aperture (NA) Access in the X Direction: The system should provide high NA access from both sides to the trapped ions for imaging the ions and addressing them with Raman beams. This allows for precise manipulation and control of individual ions in the X direction.
- High Numerical Aperture (NA) Access in the Y Direction: Similar to the X direction, high NA access from both sides is required in the Y direction for individual addressing of ions, as discussed in Chapter 4. Additionally, it allows for imaging the ions, which is crucial for monitoring the ion chain and its behavior.
- Access to a Doppler Cooling Beam: The system should provide access to a Doppler cooling beam at an angle that allows the beam to have projections in all three dimensions (X, Y, and Z). This ensures efficient cooling of the ions in all directions and helps maintain their stability.
- Access to Other Global Beams: Along the Z direction, the system should provide access to other global beams.

Design details: Figures 6.11 and 6.10 showcase different views of our science chamber, providing insights into the optical access configuration. Along the X-axis, two re-entrant windows are attached with a working distance of $15.7\,\mathrm{mm}$, allowing placement of an objective outside the vacuum chamber. These windows provide a numerical aperture (NA) of approximately 0.5, limited by the blade trap holder along the Y direction (as depicted in Fig. 6.11c). They serve the purpose of imaging the ions (collecting light at $369\,\mathrm{nm}$) and addressing the ions with Raman beams ($355\,\mathrm{nm}$) for coherent operations. Additionally, the first ionization beam (399nm) is directed along this axis for isotope selectivity.

Similarly, two re-entrant windows are installed along the Y-axis, with a working distance of $35.7\,\mathrm{mm}$, accommodating an objective with a 0.3 NA. The aperture providing this NA is limited by the blade electrodes themselves (as observed in the inset of Fig. 6.11c) along the X direction. These re-entrant windows have a glass thickness of $5\,\mathrm{mm}$ and an inner diameter of approximately $60\,\mathrm{mm}$, allowing the use of 2-inch optics with additional flexibility for mounting and fine adjustment.

Regarding the 111 beams, they enter the trapping region at an angle of 27.37 degrees with respect to the Z-axis through a 6-inch viewport in the XY plane. These beams enter and exit the trap holder via the access hole. They are elliptical in shape and tightly focused at the trap center, with a beam waist of $20, \mu\text{m} \times 200, \mu\text{m}$, ensuring a narrow gap between the blades to prevent scattering. To prevent stray background interference in the vacuum chamber, the beams exiting the trap holder are deflected using in-vacuum mirrors mounted on the backside of the chamber's groove grabbers.

In addition to the above, another set of laser beams, with a beam waist of approximately $90, \mu\text{m}$, is focused at the trap center to illuminate ions traveling along the Z-axis. These beams enter through the viewport in the XY plane and exit from the backside of the chamber. Lastly, a set of ablation laser beams, used for surface ablation, enter the chamber through the 6-inch viewport in the XY plane.

Fabrication: The re-entrant windows, crucial for achieving high numerical aperture (NA) access along the X and Y directions, were manufactured by MPF Products. However, the anti-reflection coating provided by MPF did not meet our specific requirements. As a result, we collaborated with a different vendor, FiveNine Optics, Inc. , who guaranteed us a custom coating with a reflectivity of less than 0.5% for both 355nm and 369nm at an NA of 0.6. Furthermore, this coating exhibited a reflectivity of less than 15% over a broad wavelength range of 400nm to 1800nm.

Obtaining the final re-entrant windows from both vendors posed a considerable challenge. The inherent issue was that the glass windows could not be coated with an anti-reflective coating once they were installed inside the re-entrant window tubes. Conversely, brazing the glass windows to the metal after coating would risk damaging the coating due to the high temperatures involved. To overcome this dilemma, we employed an approach: the glass windows were initially brazed to shorter metal sleeves. Subsequently, the assemblies were sent to FiveNine Optics, Inc. for coating. Once the coating process was complete, the assemblies were returned to MPF, where the glass windows were welded to longer tubes, which were in turn attached to the conflat flange. Coordinating and ensuring the smooth execution of this complex process required meticulous planning and redundancy to avoid any potential issues. Overall, this entire process took more than 1.5 years from the initial order submission to the final delivery of the coated re-entrant windows.

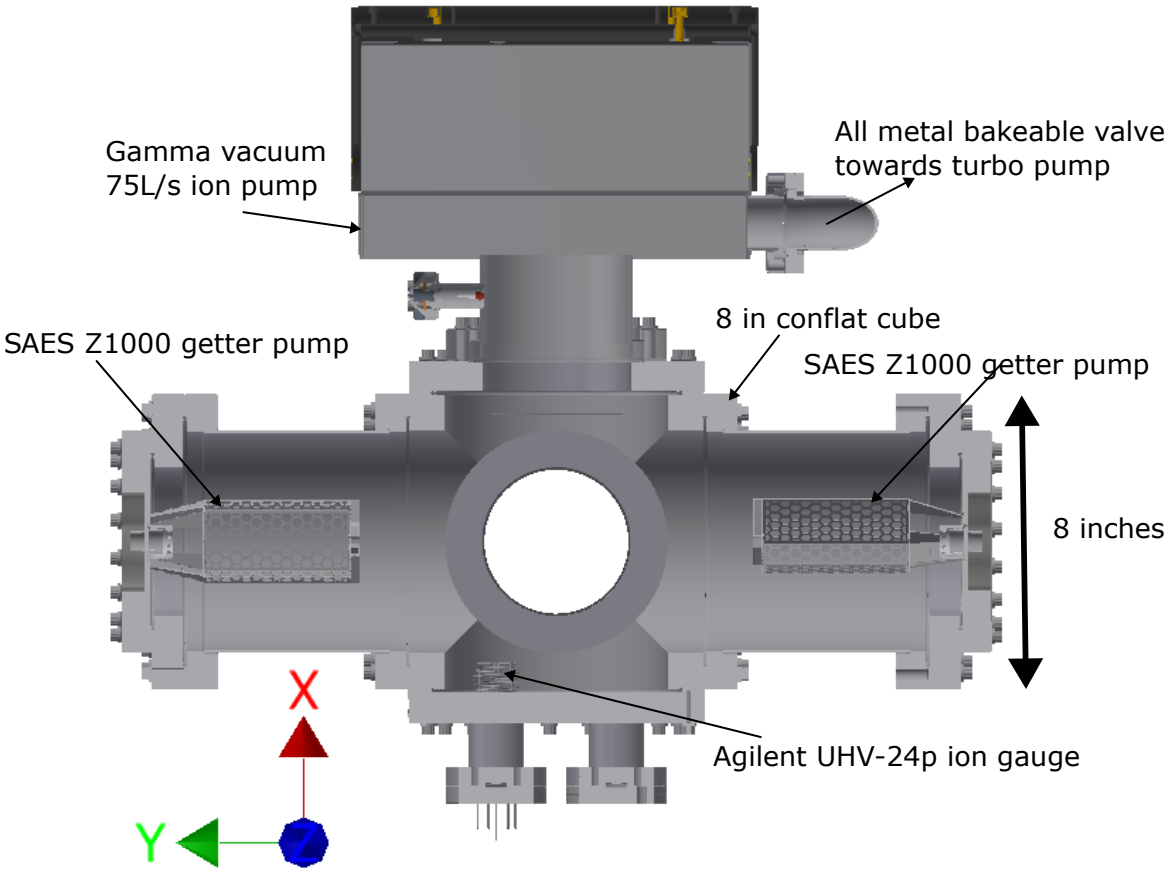

Figure 6.12: **XY Plane Cross-Section of Final Optimized UHV Assembly Configuration:** This figure illustrates the optimized ultra-high vacuum (UHV) assembly configuration designed to achieve the desired low pressures. It showcases two NEG pumps, an ion pump, and pressure measurement using an ion gauge.

6.7 UHV system

The main objective of designing the UHV assembly is to achieve pressures suitable for quantum simulation experiments with a large number of ions, such as 50 ions, over extended periods. Our target is to attain pressures in the range of 5×10^{-13} to 1×10^{-12} mbar. To accomplish this, we follow the following heuristics:

- Maximize conductance: Opt for vacuum chambers and peripherals that maximize conductance, promoting efficient gas flow and minimizing pressure buildup.
- Low outgassing materials: Choose materials with minimal outgassing to reduce contamination and maintain low pressures within the system.
- Compatible pumping system: Select pumps that do not interfere with other functionalities of the blade trap apparatus.
- Continuous monitoring: Implement measurement and inference techniques at each stage of assembly to assess pressure and outgassing levels and identify any issues hindering pressure goals.

Design details: To achieve the desired low pressures, we went through an iterative process of designing and optimizing the UHV assembly. We explored 9 to 10 different configurations of chambers and pump setups, considering factors such as conductance and the ability to achieve high numerical aperture optical access to the ions. One of the challenges we encountered during the iterations was accommodating the non-trivial angles required for the 111 beams.

Figure 6.12 illustrates the final configuration that we adopted in order to optimize pumping speeds and conductance towards the trapping region. Our setup comprises two non-evaporable getter (NEG) pumps, specifically the Z1000 model from SAES, which offer a pumping speed of 1250 lt/s for hydrogen. Additionally, we have integrated a 75 lt/s ion pump from Gamma Vacuum. To maximize the pumping conductance, the NEG pumps are affixed to 8-inch conflat nipples. These pumps are then connected to the science chamber, a Kimball Physics MCF600-SphSq-F2E4A4 model, via an 8-inch conflat cube, which ensures high pumping conductance.

For pressure measurement, an ion gauge (Agilent UHV-24p) is connected at the bottom of the cube. This gauge offers the capability to measure pressure with an x-ray limit of 5×10^{-12} Torr. It provides valuable pressure readings to assess the achieved vacuum levels within the system. Even with the maximized pumping speeds, it is crucial to address potential points of failure in the system, such as leaks, virtual leaks, and materials with high outgassing rates. To mitigate leaks, we adhere to best practices for ultra-high vacuum (UHV) by utilizing conflat components that guarantee minimal leak rates. To counter virtual leaks, we incorporate careful design considerations to ensure that no pockets of air are trapped within the system. Additionally, we incorporate relief holes at suspected locations to prevent the accumulation of trapped air. Reducing outgassing from different materials presents another challenge in achieving low pressures. Despite selecting materials

with minimal outgassing, it is necessary to meticulously treat each component in the system to remove potential outgassing elements from their bulk or surfaces.

In the following section, we outline our treatment process for every individual component in the system to minimize outgassing. Furthermore, we conduct thorough testing of each component to ensure that their outgassing and leak levels are below our required limits

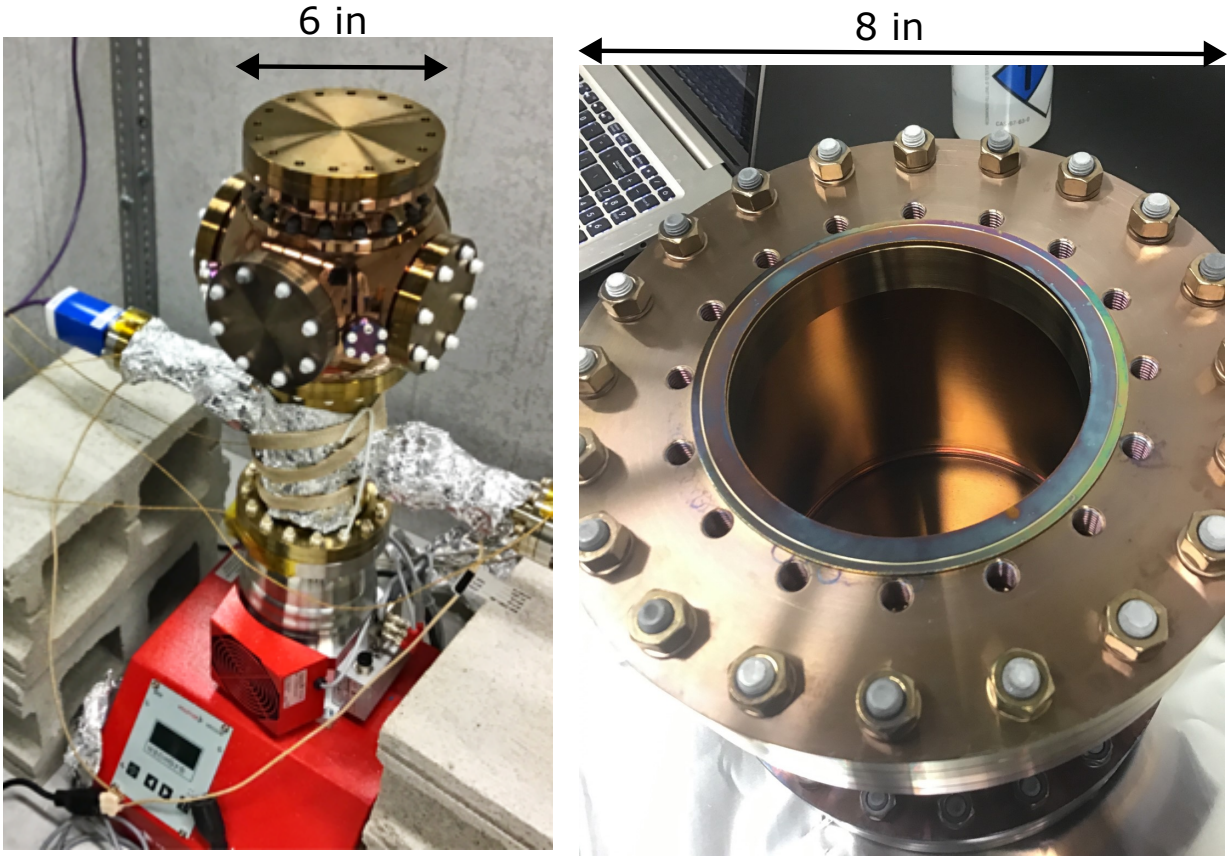

Figure 6.13: **Blade Trap UHV Surface Preparation:** The figure illustrates the baking process at 400°C for ultra-high vacuum (UHV) surface preparation, resulting in the formation of an oxide layer on the chamber components.

Vacuum surface preparation: To achieve ultra-high vacuum pressures in the vacuum chamber, all the materials need to be of low outgassing. Materials such as stainless-steel, ceramics, OFHC (oxygen-free copper), and Kapton are a few examples of low outgassing

materials. Even with such low outgassing, they still limit the low pressures achievable. Hence, they need to be subjected to accelerated outgassing to remove all the outgassing elements from the bulk and surface of the materials.

The components, after getting machined, are thoroughly cleaned using a multi-step cleaning process starting from ultrasonic cleaning with 3-4 rounds of Sparkleen + DI water with steps of 15 min followed by 15 min cleaning with DI water. The parts are dried with nitrogen after every step to remove excess water. The parts are then sonicated using Acetone followed by IPA for 15 min each. Since the parts associated are large, a large sonicator is used, and the parts are cleaned in multiple rounds by flipping around. Following the general cleaning process, the stainless-steel components are heated at 400°C while maintaining vacuum levels. This is maintained until the pressure measured in the chamber at high temperatures (400°C) reaches lower than 5×10^{-8} mbar pressures.

This requires high conductance pumping through a turbo pump. For high conductance, the parts are directly mounted on top of the turbo pump and heated to 400°C. Care was taken to not heat the turbo pump more than 60°C. A picture of baking the science chamber at 400°C is shown in Fig.6.13. Typically, this process took more than 15-20 days per component. After the pressure at 400°C reaches the desired value, the chamber is vented to atmosphere while still maintaining it at 400°C. The chamber is left exposed to atmosphere at 400°C for 1 day. This step creates an oxide layer, which gives the beautiful color as seen in Fig.6.13, and acts as a barrier for the remaining hydrogen in the bulk to outgas.

Then, the components are evacuated to high vacuum again for 1 day before gradually ramping down the temperature to room temperature while maintaining pumping from the turbo pump. Similarly, all the stainless-steel components are treated to reduce the outgassing of hydrogen from the bulk stainless-steel. Other components undergo heat treatment as well. For example, the hapal blade holder mentioned earlier is heated to 900°C while maintaining a pressure level of about 1×10^{-4} mbar for almost 10-14 days. This significantly reduces the outgassing of the Shapal piece. Without the heat treatment, the base pressure obtained with the Shapal piece is about 1×10^{-11} mbar. However, after the heat treatment, the pressure has reached below 9×10^{-13} mbar. More details of the measurements can be found in the outgassing measurements section below. Similarly, other components such as the Kapton wire and PCBs are baked at 200°C for prolonged periods of time to accelerate the outgassing levels.

Main setbacks: Before delving into the section on outgassing measurements, I will provide a brief overview of the main setbacks we encountered during the entire process of UHV assembly. I believe that others in the community can benefit from our experiences.

One of the most frustrating setbacks, which set back the overall progress by more than 1.5 years, was related to the Ion pump. Instead of the Gamma pump depicted in the design above, we initially opted for an Agilent Ion pump along with a Ti sub combination pump, which weighed around 100 kilograms. During the assembly of the system, we painstakingly put together the entire structure. After completing the extensive baking process, the final step was to activate the ion pump. However, upon pressing the button, we discovered that the pump was short-circuited.

Upon investigation, we found that the pump had an electrical short circuit inside. We reached out to the company through numerous emails and eventually had a representative from Agilent visit our location. Unfortunately, the representative opened the pump in an unclean environment to fix the short circuit. As a result, the pressures we achieved afterward were higher than expected due to plausible internal contamination caused during the repair. Consequently, we had to purchase a new pump from Gamma Vacuum.

Having learned from the previous pump failure, we decided to test the newly acquired pump separately as soon as we received it, without assembling it into the chamber. Unfortunately, luck was not on our side, as this pump also turned out to be non-functional. The pumping sparked inside, and the pressure of the bare chamber never dropped below 1×10^{-7} mbar. After exploring all possibilities, we agreed that the pump was faulty and sent it back for servicing.

After waiting for approximately a month, we received the pump back from Gamma, with them claiming that it had been repaired. When I tested the pump for the third time, it exhibited the same issues as before, failing to reach pressures below 1×10^{-7} mbar. When I asked Gamma for the test report from the second run, they did not provide one. Moreover, this time we noticed a dent on one of the pump's flanges. Upon sending the pump back to Gamma, they asserted that it was completely damaged beyond repair.

We assured them that no damage had occurred on our end and that we had simply unboxed and tested it. It is worth noting that the packaging of the pump was subpar, with the pinch-off valve consistently positioned near the edge of the packing box, resulting in noticeable damage every time we received a pump from them. Despite our repeated requests for improved packaging, they made no changes. Nonetheless, we managed to convince them that the fault lay with them, and they kindly agreed to provide us with a new pump of the same model.

After enduring considerable delays caused by periods of lockdown and restrictions in the product lines, we finally received the pump. This time, we recorded a comprehensive unboxing video from multiple angles and confirmed that the pump was finally functional.

The entire process was compounded by the lockdown periods, restrictions, and delays

in the product lines. One valuable lesson I learned from this experience is to immediately test every component, especially those with long lead times and high costs, as soon as they are received to ensure their functionality before making payment.

Another issue we faced was with the re-entrant windows, as mentioned in the previous section. We had to coordinate between two companies, MPF and FiveNine Optics, Inc., to have the re-entrants manufactured. Despite careful coordination and thorough documentation of all relevant aspects, it took over 1.5 years for them to be delivered. Upon receiving them, I quickly inspected one and it seemed fine. However, when we opened all of them prior to installation, we were surprised to find sharpie marks on the vacuum side of the re-entrants. The metal parts of the re-entrants had already undergone vacuum firing, so no cleaning process was required, and they could be used directly as received. However, the sharpie marks were located very close to the window, making it difficult to clean them forcefully. Even after meticulous cleaning, some residues remained on the re-entrant windows.

To eliminate the sharpie marks, we proceeded with a lengthy bake at 180°C to outgas them. In the end, we were able to achieve a pressure of $< 9 \times 10^{-13}$ mbar, despite the presence of the residue marks. It is interesting to note that these marks persisted even at such low pressures.

UHV Assembly: After cleaning, surface treating all the stainless-steel components. They are assembled in a cleanroom environment (Fig. 6.14) for avoiding contamination to the internals. The following procedure is used to bake and bring the whole chamber to $< 9 \times 10^{-13}$ mbar pressures.

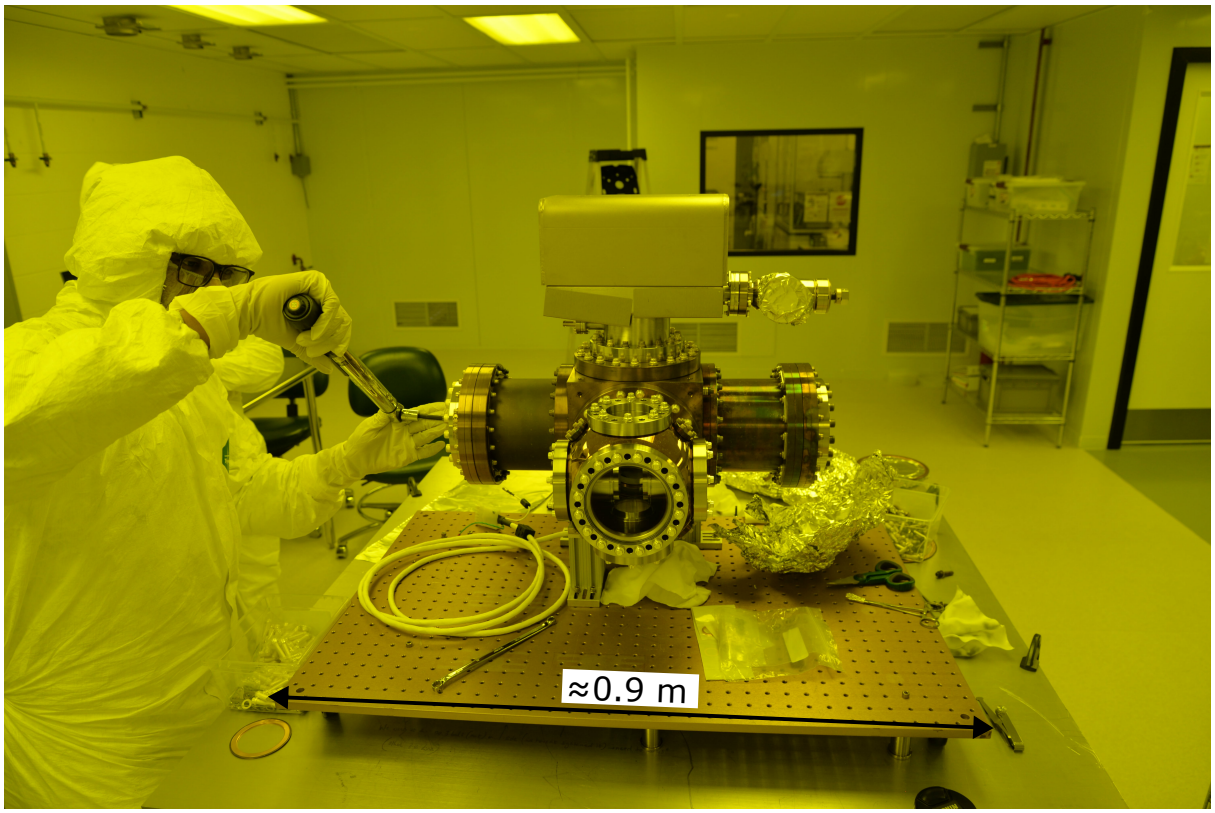

Figure 6.14: **Blade Trap UHV Assembly in a Cleanroom Environment:** This image illustrates the assembly of the entire blade trap vacuum chamber in a cleanroom environment. To prevent contamination of the chamber internals, strict cleanroom practices are followed, including the use of cleanroom personal protective equipment (PPE) such as coveralls, hairnets, beard nets, and gloves, along with thorough cleaning of the surroundings.

1. Assemble all the components, including the internals, UHV chambers, gauges, pumps, blanks, valves, and viewports, on top of a breadboard, according to the CAD model. Additionally, install a residual gas analyzer (RGA) to measure external and virtual leaks, as well as the outgassing of various internals.

2. Tighten all the bolts on the flanges using a star pattern, as specified in [79], and use a torque wrench. For CF 4.5-inch, 6-inch, and 8-inch flanges, tighten the bolts to a maximum torque of 190 in-lbs. This tightening process consists of four steps. Begin with hand tightening, followed by increments of 60, 120, and finally 190 in-lbs. For flanges located in tight corners or without access for a torque wrench, use a

regular wrench and tighten them in three steps. In such cases, after each round of tightening, use a feeler gauge to check the uniformity (variation of about 2-3 milli-inch is acceptable) of the tightening. After tightening, ensure that the gap between the two flanges falls within the range of 10-13 milli-inches.

3. Carefully transport the chamber inside the oven[4] using the detachable castors assembled on the breadboard. Ensure that the breadboard, equipped with pedestals of adjustable height, is positioned in a way where the pedestals do not make contact with the floor, and only the castors are in contact with the floor.

4. After placing the chamber assembly inside the oven, raise the breadboard using an inflatable pry bag until the castors are lifted above the floor. Then, lower the height of pedestals and remove the castor wheels. The entire process should be carried out in a manner that avoids any shock to the chamber system.

5. Install a turbo pump along with bellows outside the oven. Then, route the bellows through the viewport of the oven to attach them to the valve on the chamber. To enable baking of the bellows, wrap both the bellows and the flange on the turbo pump with heater tape and install thermocouples. Make sure to check the resistance (should be around 30 ohms) of the heater tape (used to heat bellows and turbo flange) before connecting it to the controller.

6. Attach all the necessary cables for the ion pump, getter pump, and the ion gauge that are connected to the chamber. Ensure that the attached cables are rated for the high-temperature (200°C) baking process.

7. After ensuring that all the flanges are tightened, turn on the turbo pump and wait until the pressure decreases to 1×10^{-7} mbar.

8. Perform a leak check using IPA by spraying all the places where flanges are joined while simultaneously observing the RGA (leak check mode) and turbo pump pressure. If the pressure measured on either the RGA or the turbo pump suddenly rises, indicating a leak, locate the position of the leak. Abort the process by turning off the turbo pump and venting the chamber with nitrogen, followed by inspecting and tightening the flange as required. If no leak is found (usually the case if flanges are tightened using the above-mentioned procedure), proceed to the next step. Additionally, turn on the RGA to perform a scan (up to 200 amu) and save data for reference.

[4] TestEquity 1027C

9. Once the stable pressure (approximately 1×10^{-7} mbar on the turbo gauge) is reached, attach the ion gauge cables, switch it on, and record the pressure reading on the ion gauge.

10. Degas both filaments of the ion gauge, which takes about 15 minutes each. Wait until the pressure settles, and then record the pressure after degassing.

11. Attach the cables for both the NEG pumps and the ion pump. Turn on the respective controllers for each pump to check for any errors or issues. If no problems are found, turn off the controllers. This procedure helps ensure that there are no issues with the pumps or any shorts in the ion pump.

12. Attach thermocouples at various locations, such as around the viewport locations and pumps of the chamber, to monitor temperatures. Also, attach the thermocouple used by the oven to the center of the science chamber near the re-entrant window.

13. Ground the chamber to the same reference as all the controllers, using a star configuration. Additionally, ensure proper cable management for all cables both inside and outside the oven to maintain organization and prevent interference.

14. Check the following before closing the oven door:

    (a) All units are grounded.

    (b) Ion pump and NEG pump controllers are turned off.

    (c) Thermocouple locations are properly mapped.

    (d) A glass piece is inserted into the oven for checking if the coating performance changes after baking.

    (e) The RGA controller is taken out of RGA.

    (f) A hose to push dry air into the oven is installed.

    (g) Both the feedthroughs of the oven are closed.

    (h) The TestEquity chamber is set to ON mode.

15. Close the oven door and increase the chamber temperature setpoint to 185°C (limited by the maximum temperature of th viewports and re-entrants) in steps of 2.5°C every 7.5 minutes at a rate slower than 20°C/hr. Ensure that the air temperature never overshoots more than 200°C. In parallel, raise the temperature of the turbo pump flange, bellows, and RGA to 180°C using external heater tape, while ensuring that the maximum temperature ratings are observed.

(a) 55°C for Pfiefer PKR 361 gauge with electronics.

(b) 150°C for Pfiefer PKR 361 gauge without electronics.

(c) 70°C for SRS RGA with electronics.

(d) 300°C for SRS RGA without electronics.

(e) Maximum temperature of 50°C on turbo 6-inch flange.

16. Once the temperature reaches 180°C, leave the system to bake while continually monitoring the pressure and temperature of various sensors. Caution must be taken to ensure that the turbo pump is not disturbed or its power disconnected during the bake.

17. The baking process is stopped once the pressure, as measured by the ion gauge, reaches approximately 1×10^{-8} mbar. Once this criterion is met, the temperature of the chamber, along with the turbo pump bellows, is ramped down to 110°C at the same rate as mentioned above.

18. At 110°C, turn on the ion pump and monitor for any pressure spikes. Occasionally, the ion pump, when operated at high voltage, can cause momentary pressure spikes due to shorts caused by tiny Titanium particles inside the pump. Wait until all pressure spikes have settled down, and then turn off the ion pump.

19. Turn on the NEG (Non-Evaporable Getter) activation for both getter pumps simultaneously, ensuring that the activation parameters are thoroughly checked against the datasheet. The getter activation process involves ramping up the temperature of the getters, which takes approximately 2 hours. During this time, the getter's temperature is gradually increased to 550°C. Initially, the pressure, as measured by the ion gauge, may increase to as high as 1×10^{-6} mbar.

20. After completing the NEG activation, wait until the temperature of the NEGs cools down to 110°C, which typically takes about 1-1.5 hours. Once they reach this temperature, begin ramping down the temperature of the entire chamber to 25°C at the same rate as mentioned above. Then, wait for both the chamber's temperature and the NEG to settle to room temperature.

21. Turn on the ion pump again and wait until any pressure spikes, if any, caused by the ion pump have settled down.

22. Close the valve that connects the chamber to the turbo pump bellows until it reaches a mark beyond the latest mark or 50 in lbs, whichever occurs first.

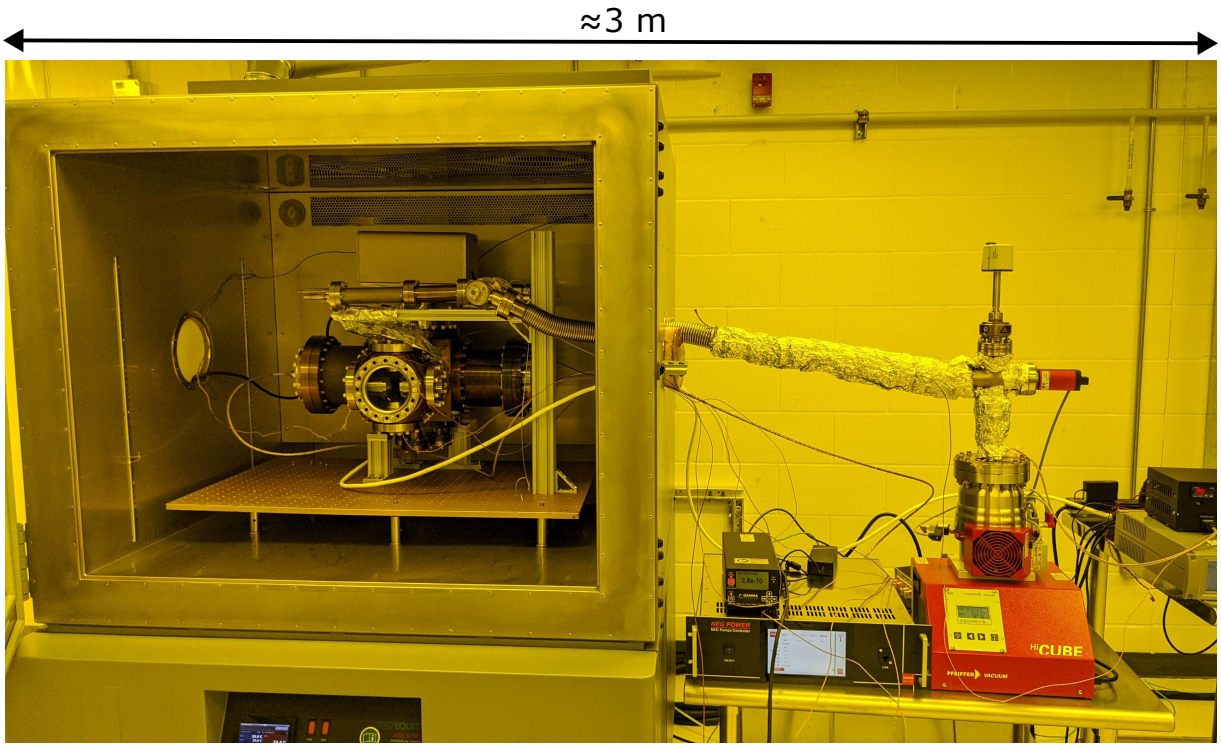

Figure 6.15: **Blade Trap UHV Assembly Baking:** This picture depicts the blade trap ultra-high vacuum (UHV) chamber installed inside an industrial oven for baking. The chamber includes additional attachments, such as a residual gas analyzer (RGA) for measuring contaminants or leaks at low pressures. The turbo pump used for evacuating the chamber is situated on the right, connected to the chamber via a bellows that is routed through a viewport on the oven.

Base pressure measurements: Using the described procedure, the chamber (Fig. 6.15) was baked along with the Shapal holder installed inside, utilizing a commercial convection oven for uniform heating of the entire system. Following the baking process, the chamber was subjected to pumping under the NEG and ion pumps. The pressure, measured using the ion gauge, eventually settled to a value of less than 9×10^{-13} mbar within approximately 2-3 days. It is important to note that the ion gauge used has an x-ray limit of 5×10^{-12} mbar. It is my understanding that below this limit, the gauge may provide measurements higher than the actual pressure. The final assessment of performance needs to be conducted by testing the lifetimes of a chain of ions.

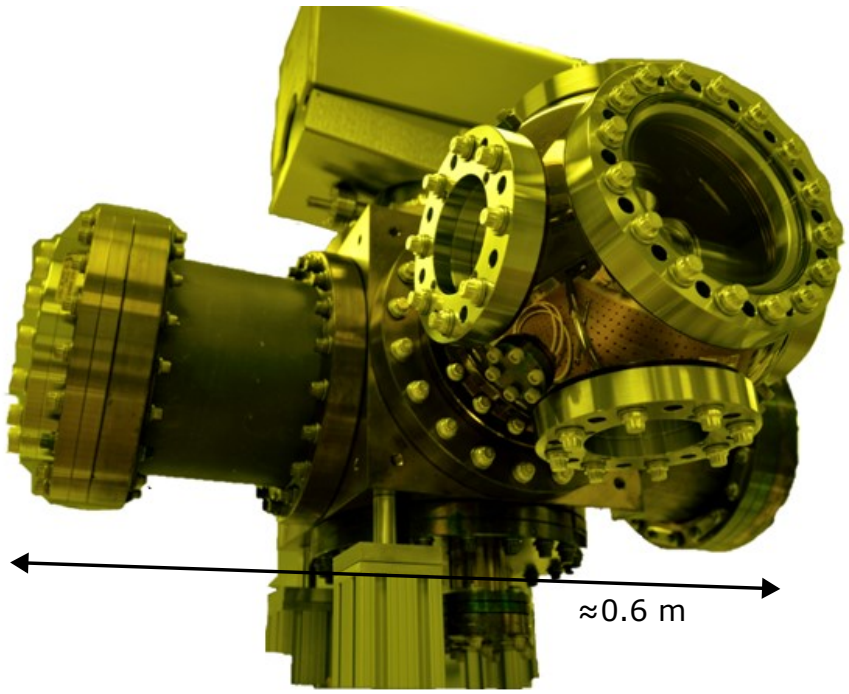

Figure 6.16: **Blade Trap UHV Current Status:** This close-up picture showcases the blade trap ultra-high vacuum (UHV) chamber assembly, featuring vacuum pumps, re-entrant windows, and viewports.

6.8 Current status

With the vacuum chamber successfully installed, we are now preparing for the internal assembly process. All necessary alignment procedures for the components have been established, and we are making final preparations before the assembly for trapping the ions. Once trapped, we will be able to conduct quantum simulations using this ion trap, taking us one step closer to our experimental goals.

Chapter 7

Conclusion and Outlook

In conclusion, throughout my PhD journey, I have had exceptional opportunities to construct two trapped ion experimental apparatus entirely from the ground up. In one of these experiments, I successfully demonstrated the preservation of asset qubits within an ion chain, even when a subsystem is measured or reset. This demonstration showcases the feasibility of performing mid-circuit measurements and resets with in-situ operation on trapped ions. Building upon this achievement, I conducted experiments such as dissipative many-body cooling, yielding preliminary yet promising results.

Additionally, I played a pivotal role in the design and development of a large-scale quantum simulator called the Blade trap. Every step of the design process was meticulously executed, with careful attention to detail. Rigorous testing was conducted at each stage to validate our designs. As a result of our efforts, we have achieved a significant milestone by attaining pressures below 9×10^{-13} mbar as our base pressure (in the UHV chamber containing most of the outgassing elements and the glass windows).

Our demonstrated results have opened up new avenues for exploring novel physics in open quantum systems, particularly in the realms of quantum simulations involving local dissipation, measurements, and quantum reservoir engineering. The success of our mid-circuit reset experiments, combined with our state-of-the-art four-rod quantum simulator apparatus, has paved the way for exciting possibilities, such as the ability to prepare non-trivial states using state reset beams and engineer dissipations.

Furthermore, our protocol for achieving mid-circuit measurements and resets can be synergistically combined with other error-mitigation methods. For example, incorporating shorter-distance shuttling or utilizing a different isotope of the same ion species can help reduce crosstalk errors, which are compatible with quantum error correction protocols.

Short-distance shuttling (on the order of tens of microns) would enhance the speed of quantum algorithms and minimize errors caused by motional heating, as opposed to the current experiments that employ hundreds of microns shuttling.

By considering a typical isotope shift of a few hundred MHz and taking into account our demonstrated intensity crosstalk of less than $\lesssim 8 \times 10^{-5}$, the probability of error (P_{AQM}) for state reset and measurement can be reduced to the level of 10^{-6}. Furthermore, incorporating a different isotope of the same ion species would address challenges related to reduced motional coupling between ions of disparate masses during mid-circuit sympathetic cooling and quantum gate operations, as highlighted in previous studies [104, 43, 101].

The preliminary results of the dissipative many-body cooling experiment are promising. While Chapter 5 presents various exploratory considerations, there are additional factors that warrant careful examination. Our investigation must continue into why the system's energy does not decrease as close to the ground state as initially anticipated. It is important to validate the hypothesis suggesting the involvement of decoherence or additional terms in the Hamiltonian. Furthermore, we need to determine whether the cooling process genuinely leads to the creation of a many-body state or inadvertently destroys correlations during its course. This aspect is of paramount importance and requires further investigation. Additionally, even in our simulations, it is evident that the system does not reach the exact ground state. It is imperative to gain a comprehensive understanding of the underlying reasons for this behavior and to identify any contributing factors.

Exploring the selection of spins to reset is another avenue to consider. By leveraging the symmetries present in the ground state, we can selectively reset the spins that break or forbid higher excited states. This approach may lead to improved cooling results by exploiting the inherent properties of the system. Additionally, the timing of the reset operations needs careful consideration. Periodic resets may not be the optimal strategy. Instead, we can base the decision to reset on the measurements performed, setting a threshold for a spin expectation value of the bath. Adaptive strategies of this kind would be beneficial, especially when dealing with a large number of ions, where classical simulations to find the correct parameters are not feasible. Furthermore, the protocol requires an additional transverse field to be present for effective cooling to occur. Exploring the parameter regimes in which this protocol works optimally is necessary.

Considering the integration of adiabatic simulations or classical optimization algorithms could also enhance the results. Adapting the protocol to take the system closer, if not to the ground state, would benefit classical optimization algorithms. By reducing the Hilbert space to search from, overall performance could be improved. Lastly, the issue of heating due to the number of resets in the Hilbert space needs to be addressed. Understanding and

mitigating the heating effects associated with the reset operations is crucial for achieving the desired cooling results.

In summary, there are several aspects that require further investigation, including understanding the limitations of the current cooling results, addressing the impact on many-body correlations, optimizing the selection and timing of resets, exploring parameter regimes and additional field requirements, and mitigating heating effects. By addressing these areas, we can enhance the performance and effectiveness of the protocol.

While the current base pressure results for the Blade trap appear promising, it is essential to install and test the internals of the Blade trap to obtain actual pressure results, which can also be determined from ion lifetimes. Determining the achievable lower limit of pressures is a critical consideration. Investigating the possibility of achieving even lower pressures by operating at cryostat temperatures should be explored. Another significant uncertainty that arises during the assembly of an ion trap pertains to the electrical connections. Despite thorough planning and testing, many experiments encounter failures as the entire trap is assembled, baked, transported, and made functional. Even slight changes in the electrical and mechanical properties of DC and RF electrical connections can result in unexpected outcomes. Therefore, it is crucial to conduct comprehensive testing of the electrical connections to ensure their functionality and reliability. Furthermore, it is important to assess whether the alignment of the system deteriorates during the baking process. In light of the transportation of the entire chamber to the laboratory, potential issues must be identified and addressed. It is necessary to evaluate whether any challenges or complications would arise from moving the chamber and whether they would affect the system's performance.

Once the chamber is assembled and transported, one of the most significant challenges in ensuring the fruitful operation of the apparatus is its interaction with external components, such as optics and various electronics. The high optical access provided by the Blade trap introduces stability-related challenges. Despite the overall robust design of the system, it is imperative to ensure that external mechanical components are equally robust and properly referenced to the UHV chamber. This is vital for minimizing system drifts and reducing the necessity for frequent calibrations. This challenge is further compounded by the need to use mechanical structures like translation stages to align the optics with the ions accurately, with a precision of tens of micrometers. Balancing flexibility and stability in the design of these external structures adds complexity to the system.

While we have designed the Blade trap apparatus to be operational for a chain of up to 50 ions, sufficient to demonstrate interesting physics, there is no reason why we cannot scale to a larger number of ions. However, various challenges emerge when attempting

to operate with a single long chain of ions in a single trap. One of the major physical limitations encountered when scaling up to a larger number of ions is mode crowding. As the number of ions increases with fixed radial trap frequencies, the number of motional modes also increases, leading to overcrowding of these modes and a slowing down of the interaction time scale. Addressing this issue and finding suitable solutions are imperative for the successful operation of the system. One possible solution is to increase the trap frequencies, which would require higher trap voltages. It is essential to evaluate the feasibility of using higher voltages to achieve faster simulation speeds while considering the limitations of feedthrough and the materials used in the setup. Furthermore, it's worth considering the implementation of multiple traps instead of a single trap with a long chain, as this approach could offer additional benefits and improved performance. Integrating microfabricated blade trap setups with chip traps presents an intriguing possibility. This integration would allow for enhanced control over electrode geometry, potential shaping, and precise alignment for addressing micromotion concerns, all while achieving higher simulation speeds. Lastly, it is crucial to assess whether all components and functionalities can be integrated into a compact, scalable architecture. This evaluation will determine the overall feasibility and practicality of the system's design and implementation.

The field of analog quantum simulation still presents ample opportunities for tackling various problems. Currently, the primary limitation resides in the hardware aspect. There is hope that advancements in hardware will soon catch up, allowing quantum computers to transcend proof-of-principle experiments and become genuinely useful tools. Overcoming this hardware bottleneck is pivotal for the practical implementation and realization of analog quantum simulation. In addition to addressing this challenge, it is essential to explore alternative protocols, such as analog-digital simulations [84]. In these protocols, the Hamiltonian is partitioned into multiple analog steps, offering enhanced functionality. By demonstrating different Hamiltonians at discrete time steps, we can broaden the capabilities and versatility of our setups.

Through the exploration of diverse simulation protocols, the expansion of hardware capabilities, and the proactive addressing of current limitations, we can lay the foundation for more sophisticated and practical applications of quantum simulations in the future.

References

[1] M. Acton. *Detection and Control of Individual Trapped Ions and Neutral Atoms*. PhD thesis, The University of Michigan, 2008.

[2] F. Arute, K. Arya, R. Babbush, D. Bacon, J. Bardin, R. Barends, R. Biswas, S. Boixo, F. Brandao, D. Buell, et al. Quantum supremacy using a programmable superconducting processor. *Nature*, 574(7779):505–510, 2019.

[3] A. Aspuru-Guzik and P. Walther. Photonic quantum simulators. *Nature physics*, 8(4):285–291, 2012.

[4] A. Auerbach. *Interacting Electrons and Quantum Magnetism*. Springer New York, NY, 2^{nd} edition, 1994.

[5] C. Bauer, Z. Davoudi, A. Balantekin, T. Bhattacharya, M. Carena, W. de Jong, P. Draper, A. El-Khadra, N. Gemelke, M. Hanada, D. Kharzeev, H. Lamm, Y. Li, J. Liu, M. Lukin, Y. Meurice, C. Monroe, B. Nachman, G. Pagano, J. Preskill, E. Rinaldi, A. Roggero, ro, D. Santiago, M. Savage, I. Siddiqi, G. Siopsis, D. Van Zanten, N. Wiebe, Y. Yamauchi, K. Yeter-Aydeniz, and S. Zorzetti. Quantum Simulation for High-Energy Physics. *PRX Quantum*, 4:027001, 5 2023.

[6] P. Becker. *Non-Integrable Dynamics in a Trapped-Ion Quantum Simulator*. PhD thesis, University of Maryland, 2021.

[7] Berkel, D. , and M. Boshier. Destabilization of dark states and optical spectroscopy in Zeeman-degenerate atomic systems. *Physical Review A*, 65(3):033413, 2 2002.

[8] Berkel, D. , J. Miller, J. Bergquist, W. Itano, Winel, and D. . Minimization of ion micromotion in a Paul trap. *Journal of applied physics*, 83(10):5025–5033, 1998.

[9] R. Blatt and C. Roos. Quantum simulations with trapped ions. *Nature Physics*, 8(4):277–284, 2012.

[10] A. Browaeys and T. Lahaye. Many-body physics with individually controlled Rydberg atoms. *Nature Physics*, 16(2):132–142, 2020.

[11] C. Bruzewicz, R. McConnell, J. Sedlacek, J. Stuart, W. Loh, J. Sage, and J. Chiaverini. High-fidelity, single-shot, quantum-logic-assisted readout in a mixed-species ion chain. *arXiv preprint arXiv:1706.05102*, 2017.

[12] T. Brydges, A. Elben, P. Jurcevic, B. Vermersch, C. Maier, B. Lanyon, P. Zoller, R. Blatt, and C. Roos. Probing Rényi entanglement entropy via randomized measurements. *Science*, 364(6437):260–263, 2019.

[13] D. Budker, D. Kimball, and D. DeMille. *Atomic physics: an exploration through problems and solutions*. Oxford University Press, USA, 2004.

[14] A. Chan, N, R. Kishore, M. Pretko, and G. Smith. Unitary-projective entanglement dynamics. *Physical Review B*, 99(22):224307, 6 2019.

[15] L. Chen, H. Li, Y. Lu, C. Warren, C. Križan, S. Kosen, oko, M. Rommel, S. Ahmed, A. Osman, J. Biznárová, A. Fadavi Roudsari, B. Lienhard, M. Caputo, K. Grigoras, L. Grönberg, J. Govenius, A. Kockum, P. Delsing, Byl, J. er, and G. Tancredi. Transmon qubit readout fidelity at the threshold for quantum error correction without a quantum-limited amplifier. *npj Quantum Information 2023 9:1*, 9(1):1–7, 3 2023.

[16] E. Chertkov, J. Bohnet, D. Francois, J. Gaebler, D. Gresh, A. Hankin, K. Lee, D. Hayes, B. Neyenhuis, R. Stutz, A. Potter, and M. Foss-Feig. Holographic dynamics simulations with a trapped-ion quantum computer. *Nature Physics*, 18(9):1074–1079, 9 2022.

[17] C. Conti. Adiabatic evolution on a spatial-photonic Ising machine — newcomplexlight.org.

[18] S. Crain, C. Cahall, G. Vrijsen, E. Wollman, M. Shaw, V. Verma, S. Nam, and J. Kim. High-speed low-crosstalk detection of a 171Yb+ qubit using superconducting nanowire single photon detectors. *Communications Physics*, 2(1):97, 12 2019.

[19] S. Czischek, G. Torlai, S. Ray, R. Islam, and R. Melko. Simulating a measurement-induced phase transition for trapped-ion circuits. *Physical Review A*, 104(6):062405, 12 2021.

[20] A. Daley, I. Bloch, C. Kokail, S. Flannigan, N. Pearson, M. Troyer, and P. Zoller. Practical quantum advantage in quantum simulation. *Nature 2022 607:7920*, 607(7920):667–676, 7 2022.

[21] A. Das and B. Chakrabarti. Colloquium: Quantum annealing and analog quantum computation. *Rev. Mod. Phys.*, 80:1061–1081, 9 2008.

[22] Z. Davoudi, M. Hafezi, C. Monroe, G. Pagano, A. Seif, and A. Shaw. Towards analog quantum simulations of lattice gauge theories with trapped ions. *Physical Review Research*, 2(2):023015, 4 2020.

[23] D. DiVincenzo. The Physical Implementation of Quantum Computation. *Fortschritte der Physik*, 48(9-11):771–783, 9 2000.

[24] S. Earnshaw. On the nature of the molecular forces which regulate the constitution of the luminiferous ether. *Transactions of the Cambridge Philosophical Society*, 7:97, 1848.

[25] T. Einwohner, J. Wong, and J. Garrison. Analytical solutions for laser excitation of multilevel systems in the rotating-wave approximation. *Physical Review A*, 14(4):1452–1456, 10 1976.

[26] S. Ejtemaee, R. Thomas, and P. Haljan. Optimization of Yb+ fluorescence and hyperfine-qubit detection. *Physical Review A*, 82(6):063419, 2010.

[27] A. Friedenauer, H. Schmitz, J. Glueckert, D. Porras, and T. Schätz. Simulating a quantum magnet with trapped ions. *Nature Physics*, 4(10):757–761, 2008.

[28] J. Gaebler, C. Baldwin, S. Moses, J. Dreiling, C. Figgatt, M. Foss-Feig, D. Hayes, and J. Pino. Suppression of midcircuit measurement crosstalk errors with micromotion. *Physical Review A*, 104(6):062440, 12 2021.

[29] J. Gaebler, C. Baldwin, S. Moses, J. Dreiling, C. Figgatt, M. Foss-Feig, D. Hayes, and J. Pino. Suppression of midcircuit measurement crosstalk errors with micromotion. *Physical Review A*, 104(6):062440, 12 2021.

[30] I. Georgescu, S. Ashhab, and F. Nori. Quantum simulation. *Reviews of Modern Physics*, 86(1):153, 2014.

[31] E. Gibney. Hello quantum world! Google publishes landmark quantum supremacy claim. *Nature*, 574(7779):461–463, 2019.

[32] C. Gross and I. Bloch. Quantum simulations with ultracold atoms in optical lattices. *Science*, 357(6355):995–1001, 2017.

[33] P. Harrington, E. Mueller, and K. Murch. Engineered dissipation for quantum information science. *Nature Reviews Physics 2022 4:10*, 4(10):660–671, 8 2022.

[34] M. Hartmann. Quantum simulation with interacting photons. *Journal of Optics*, 18(10):104005, 2016.

[35] K. He, X. Geng, R. Huang, J. Liu, and W. Chen. Quantum computation and simulation with superconducting qubits. *Chinese Physics B*, 30(8):080304, 2021.

[36] R. He, J. Cui, R. Li, Z. Qian, Y. Chen, M. Ai, Y. Huang, C. Li, and G. Guo. An ion trap apparatus with high optical access in multiple directions. *Review of Scientific Instruments*, 92(7):073201, 7 2021.

[37] C. Hempel, C. Maier, J. Romero, J. McClean, T. Monz, H. Shen, P. Jurcevic, B. Lanyon, P. Love, R. Babbush, A. Aspuru-Guzik, R. Blatt, and C. Roos. Quantum Chemistry Calculations on a Trapped-Ion Quantum Simulator. *Phys. Rev. X*, 8:031022, 7 2018.

[38] J. Hilder, D. Pijn, O. Onishchenko, A. Stahl, M. Orth, B. Lekitsch, A. Rodriguez-Blanco, M. Müller, F. Schmidt-Kaler, and U. Poschinger. Fault-Tolerant Parity Readout on a Shuttling-Based Trapped-Ion Quantum Computer. *Physical Review X*, 12(1):011032, 2 2022.

[39] S. Hirthe, T. Chalopin, D. Bourgund, P. Bojović, A. Bohrdt, E. Demler, F. Grusdt, I. Bloch, and T. Hilker. Magnetically mediated hole pairing in fermionic ladders of ultracold atoms. *Nature*, 613(7944):463–467, 2023.

[40] J. Home, D. Hanneke, J. Jost, J. Amini, D. Leibfried, Winel, and D. . Complete Methods Set for Scalable Ion Trap Quantum Information Processing. *Science*, 325(5945):1227–1230, 9 2009.

[41] A. Houck, H. Türeci, and J. Koch. On-chip quantum simulation with superconducting circuits. *Nature Physics*, 8(4):292–299, 2012.

[42] D. Hume, Rosenb, T. , Winel, and D. . High-Fidelity Adaptive Qubit Detection through Repetitive Quantum Nondemolition Measurements. *Physical Review Letters*, 99(12):120502, 9 2007.

[43] I. Inlek, C. Crocker, M. Lichtman, K. Sosnova, and C. Monroe. Multispecies Trapped-Ion Node for Quantum Networking. *Physical Review Letters*, 118(25):250502, 6 2017.

[44] R. Islam. *Quantum Simulation of Interacting Spin Models with Trapped Ions*. PhD thesis, University of Maryland, 2012.

[45] R. Islam, E. Edwards, K. Kim, S. Korenblit, C. Noh, H. Carmichael, G. Lin, L. Duan, C. Joseph Wang, J. Freericks, et al. Onset of a quantum phase transition with a trapped ion quantum simulator. *Nature communications*, 2(1):377, 2011.

[46] R. Islam, C. Senko, W. Campbell, S. Korenblit, J. Smith, A. Lee, E. Edwards, C. Wang, J. Freericks, and C. Monroe. Emergence and frustration of magnetism with variable-range interactions in a quantum simulator. *Science*, 340(6132):583–587, 2013.

[47] J. Johansson, P. Nation, and F. Nori. QuTiP 2: A Python framework for the dynamics of open quantum systems. *Computer Physics Communications*, 184(4):1234–1240, 4 2013.

[48] P. Jurcevic, H. Shen, P. Hauke, C. Maier, T. Brydges, C. Hempel, B. Lanyon, M. Heyl, R. Blatt, and C. Roos. Direct Observation of Dynamical Quantum Phase Transitions in an Interacting Many-Body System. *Phys. Rev. Lett.*, 119:080501, 8 2017.

[49] K. Kim, M. Chang, S. Korenblit, R. Islam, E. Edwards, J. Freericks, G. Lin, L. Duan, and C. Monroe. Quantum simulation of frustrated Ising spins with trapped ions. *Nature*, 465(7298):590–593, 2010.

[50] N. Kotibhaskar. Design and construction of an ion trapping apparatus for quantum simulation experiments. Master's thesis, University of Waterloo, 2019.

[51] N. Kotibhaskar, N. Greenberg, S. Motlakunta, C. Shih, and R. Islam. Fast and high-yield fabrication of axially symmetric ion-trap needle electrodes via two step electrochemical etching. *Review of Scientific Instruments*, 94(3):033201, 3 2023.

[52] T. Ladd, F. Jelezko, R. Laflamme, Y. Nakamura, C. Monroe, and J. O'Brien. Quantum computers. *Nature*, 464(7285):45–53, 3 2010.

[53] C. Langer. *High Fidelity Quantum Information Processing with Trapped Ions*. PhD thesis, University of Colorado, 2006.

[54] T. Lauprêtre, L. Groult, B. Achi, M. Petersen, Y. Kersalé, M. Delehaye, and C. Lacroûte. Absolute frequency measurements of the 1S01P1 transition in ytterbium. *OSA Continuum*, 3(1):50, 1 2020.

[55] A. Lavasani, Y. Alavirad, and M. Barkeshli. Measurement-induced topological entanglement transitions in symmetric random quantum circuits. *Nature Physics*, 17(3):342–347, 3 2021.

[56] A. Lee, J. Smith, P. Richerme, B. Neyenhuis, P. Hess, J. Zhang, and C. Monroe. Engineering large Stark shifts for control of individual clock state qubits. *Physical Review A*, 94(4):042308, 2016.

[57] Leibr, D. T, and J. Heidecker. An open source digital servo for AMO physics experiments. *arXiv preprint arXiv:1508.06319*, 8 2015.

[58] Y. Li, X. Chen, and M. Fisher. Quantum Zeno effect and the many-body entanglement transition. *Physical Review B*, 98(20):205136, 11 2018.

[59] G. Lin, S. Zhu, R. Islam, K. Kim, M. Chang, S. Korenblit, C. Monroe, and L. Duan. Large-scale quantum computation in an anharmonic linear ion trap. *Europhysics Letters*, 86(6):60004, 2009.

[60] Y. Lin, J. Gaebler, F. Reiter, T. Tan, R. Bowler, A. Sørensen, D. Leibfried, Winel, and D. . Dissipative production of a maximally entangled steady state of two quantum bits. *Nature 2013 504:7480*, 504(7480):415–418, 11 2013.

[61] J. Lis, A. Senoo, W. McGrew, F. Rönchen, A. Jenkins, and A. Kaufman. Mid-circuit operations using the omg-architecture in neutral atom arrays. *arXiv preprint arXiv:2305.19266*, 2023.

[62] T. Manovitz, Y. Shapira, L. Gazit, N. Akerman, and R. Ozeri. Trapped-Ion Quantum Computer with Robust Entangling Gates and Quantum Coherent Feedback. *PRX Quantum*, 3(1):010347, 3 2022.

[63] J. Martinis. Qubit metrology for building a fault-tolerant quantum computer. *npj Quantum Information 2015 1:1*, 1(1):1–3, 10 2015.

[64] P. Maunz. High Optical Access Trap 2.0. Technical report, Sandia National Laboratories (SNL), 1 2016.

[65] J. McClean, S. Boixo, V. Smelyanskiy, R. Babbush, and H. Neven. Barren plateaus in quantum neural network training landscapes. *Nature communications*, 9(1):4812, 2018.

[66] X. Mi, A. Michailidis, S. Shabani, K. Miao, P. Klimov, J. Lloyd, E. Rosenberg, R. Acharya, I. Aleiner, T. Andersen, et al. Stable quantum-correlated many body states via engineered dissipation. *arXiv preprint arXiv:2304.13878*, 4 2023.

[67] K. Mølmer and A. Sørensen. Multiparticle Entanglement of Hot Trapped Ions. *Phys. Rev. Lett.*, 82:1835–1838, Mar 1999.

[68] C. Monroe, W. Campbell, L. Duan, Z. Gong, A. Gorshkov, P. Hess, R. Islam, K. Kim, N. Linke, G. Pagano, P. Richerme, C. Senko, and N. Yao. Programmable quantum simulations of spin systems with trapped ions. *Reviews of Modern Physics*, 93(2):025001, 4 2021.

[69] S. Morita and H. Nishimori. Mathematical foundation of quantum annealing. *Journal of Mathematical Physics*, 49(12), 2008.

[70] S. Motlakunta. Developing theoretical and experimental tools for a hybrid quantum simulator based on trapped ions. Master's thesis, University of Waterloo, 2018.

[71] S. Motlakunta, N. Kotibhaskar, C. Shih, A. Vogliano, D. Mclaren, L. Hahn, J. Zhu, R. Hablützel, , and R. Islam. Preserving a qubit during adjacent measurements at a few micrometers distance. *arXiv preprint arXiv:2306.03075*, 6 2023.

[72] V. Negnevitsky, M. Marinelli, K. Mehta, H. Lo, C. Flühmann, and J. Home. Repeated multi-qubit readout and feedback with a mixed-species trapped-ion register. *Nature*, 563(7732):527–531, 11 2018.

[73] B. Neyenhuis, J. Zhang, P. Hess, J. Smith, A. Lee, P. Richerme, Z. Gong, A. Gorshkov, and C. Monroe. Observation of prethermalization in long-range interacting spin chains. *Science advances*, 3(8):e1700672, 2017.

[74] M. Nielsen and I. Chuang. *Quantum Computation and Quantum Information*. Cambridge University Press, 6 2012.

[75] R. Noek, G. Vrijsen, D. Gaultney, E. Mount, T. Kim, P. Maunz, and J. Kim. High speed, high fidelity detection of an atomic hyperfine qubit. *Optics Letters*, 38(22):4735, 11 2013.

[76] C. Noel, P. Niroula, D. Zhu, A. Risinger, L. Egan, D. Biswas, M. Cetina, A. Gorshkov, M. Gullans, D. Huse, and C. Monroe. Measurement-induced quantum phases realized in a trapped-ion quantum computer. *Nature Physics*, 18(7):760–764, 7 2022.

[77] S. Olmschenk, K. Younge, D. Moehring, D. Matsukevich, P. Maunz, and C. Monroe. Manipulation and detection of a trapped Yb+ hyperfine qubit. *Physical Review A*, 76(5):052314, 11 2007.

[78] G. Pagano, P. Hess, H. Kaplan, W. Tan, P. Richerme, P. Becker, A. Kyprianidis, J. Zhang, E. Birckelbaw, Hern, M. ez, et al. Cryogenic trapped-ion system for large scale quantum simulation. *Quantum Science and Technology*, 4(1):014004, 2018.

[79] Varun Patel. Flange Bolt torque sequence.

[80] W. Paul and H. Steinwedel. Ein neues Massenspektrometer ohne Magnetfeld. *Zeitschrift fur Naturforschung - Section A Journal of Physical Sciences*, 8(7):448–450, 7 1953.

[81] F. Pedregosa, G. Varoquaux, A. Gramfort, re, V. Michel, B. Thirion, , O. Grisel, M. Blondel, P. Prettenhofer, R. Weiss, V. Dubourg, et al. Scikit-learn: Machine learning in Python. *the Journal of machine Learning research*, 12:2825–2830, 2011.

[82] J. Pino, J. Dreiling, C. Figgatt, J. Gaebler, S. Moses, M. Allman, C. Baldwin, M. Foss-Feig, D. Hayes, K. Mayer, C. Ryan-Anderson, and B. Neyenhuis. Demonstration of the trapped-ion quantum CCD computer architecture. *Nature*, 592(7853):209–213, 4 2021.

[83] P. Poggi, N. Lysne, K. Kuper, I. Deutsch, and P. Jessen. Quantifying the Sensitivity to Errors in Analog Quantum Simulation. *PRX Quantum*, 1(2):020308, 10 2020.

[84] F. Rajabi, S. Motlakunta, C. Shih, N. Kotibhaskar, Q. Quraishi, A. Ajoy, and R. Islam. Dynamical Hamiltonian engineering of 2D rectangular lattices in a one-dimensional ion chain. *npj Quantum Information 2019 5:1*, 5(1):1–7, 4 2019.

[85] P. Richerme, C. Senko, J. Smith, A. Lee, S. Korenblit, and C. Monroe. Experimental performance of a quantum simulator: Optimizing adiabatic evolution and identifying many-body ground states. *Phys. Rev. A*, 88:012334, 07 2013.

[86] M. Riebe, H. Häffner, C. Roos, W. Hänsel, J. Benhelm, G. Lancaster, T. Körber, C. Becher, F. Schmidt-Kaler, D. James, and R. Blatt. Deterministic quantum teleportation with atoms. *Nature*, 429(6993):734–737, 6 2004.

[87] C. Ryan-Anderson, J. Bohnet, K. Lee, D. Gresh, A. Hankin, J. Gaebler, D. Francois, A. Chernoguzov, D. Lucchetti, N. Brown, T. Gatterman, S. Halit, K. Gilmore, J. Gerber, B. Neyenhuis, D. Hayes, and R. Stutz. Realization of Real-Time Fault-Tolerant Quantum Error Correction. *Physical Review X*, 11(4):041058, 12 2021.

[88] M. Sajjan. Experimental and theoretical investigations of radio-frequency and optical trapping potentials for atomic ions. Master's thesis, University of Waterloo, 2020.

[89] S. Sang and T. Hsieh. Measurement-protected quantum phases. *Physical Review Research*, 3(2):023200, 6 2021.

[90] P. Schindler, D. Nigg, T. Monz, J. Barreiro, E. Martinez, S. Wang, S. Quint, Br, M. l, V. Nebendahl, C. Roos, M. Chwalla, M. Hennrich, and R. Blatt. A quantum information processor with trapped ions. *New Journal of Physics*, 15(12):123012, 12 2013.

[91] C. Schneider, D. Porras, and T. Schaetz. Experimental quantum simulations of many-body physics with trapped ions. *Reports on Progress in Physics*, 75(2):024401, 2012.

[92] C. Senko. *Dynamics and excited states of quantum many-body spin systems with trapped ions*. PhD thesis, University of Maryland, 2014.

[93] C. Shih, S. Motlakunta, N. Kotibhaskar, M. Sajjan, R. Hablützel, , and R. Islam. Reprogrammable and high-precision holographic optical addressing of trapped ions for scalable quantum control. *npj Quantum Information*, 7(1):57, 12 2021.

[94] P. Shor. Scheme for reducing decoherence in quantum computer memory. *Physical Review A*, 52(4):R2493–R2496, 10 1995.

[95] P. Sierant, G. Chiriacò, F. Surace, S. Sharma, X. Turkeshi, M. Dalmonte, R. Fazio, and G. Pagano. Dissipative Floquet Dynamics: from Steady State to Measurement Induced Criticality in Trapped-ion Chains. *Quantum*, 6:638, 2 2022.

[96] K. Singh, C. Bradley, An, S. , V. Ramesh, R. White, and H. Bernien. Mid-circuit correction of correlated phase errors using an array of spectator qubits. *Science*, 5 2023.

[97] J. Siverns, L. Simkins, S. Weidt, and W. Hensinger. On the application of radio frequency voltages to ion traps via helical resonators. *Applied Physics B: Lasers and Optics*, 107(4):921–934, 6 2012.

[98] B. Skinner, J. Ruhman, and A. Nahum. Measurement-Induced Phase Transitions in the Dynamics of Entanglement. *Physical Review X*, 9(3):031009, 7 2019.

[99] J. Smith, A. Lee, P. Richerme, B. Neyenhuis, P. Hess, P. Hauke, M. Heyl, D. Huse, and C. Monroe. Many-body localization in a quantum simulator with programmable random disorder. *Nature Physics*, 12(10):907–911, 2016.

[100] A. Sørensen and K. Mølmer. Quantum Computation with Ions in Thermal Motion. *Physical Review Letters*, 82(9):1971, 3 1999.

[101] K. Sosnova, A. Carter, and C. Monroe. Character of motional modes for entanglement and sympathetic cooling of mixed-species trapped-ion chains. *Physical Review A*, 103(1):012610, 1 2021.

[102] A. Steane. The ion trap quantum information processor. *Applied Physics B: Lasers and Optics*, 64(6):623–643, 6 1997.

[103] J. Sterk, H. Coakley, J. Goldberg, V. Hietala, J. Lechtenberg, H. McGuinness, D. McMurtrey, L. Parazzoli, J. Van Der Wall, and D. Stick. Closed-loop optimization of fast trapped-ion shuttling with sub-quanta excitation. *npj Quantum Information*, 8(1):68, 6 2022.

[104] Y. Teoh, M. Sajjan, Z. Sun, F. Rajabi, and R. Islam. Manipulating phonons of a trapped-ion system using optical tweezers. *Physical Review A*, 104(2):022420, 8 2021.

[105] F. Verstraete, M. Wolf, and J. Ignacio Cirac. Quantum computation and quantum-state engineering driven by dissipation. *Nature Physics 2009 5:9*, 5(9):633–636, 7 2009.

[106] A. Vogliano. Coherent interactions and thermometry in a trapped ion quantum simulator. Master's thesis, University of Waterloo, 2022.

[107] Y. Wan, D. Kienzler, S. Erickson, K. Mayer, T. Tan, J. Wu, H. Vasconcelos, S. Glancy, E. Knill, Winel, D. , A. Wilson, and D. Leibfried. Quantum gate teleportation between separated qubits in a trapped-ion processor. *Science*, 364(6443):875–878, 5 2019.

[108] P. Wang, C. Luan, M. Qiao, M. Um, J. Zhang, Y. Wang, X. Yuan, M. Gu, J. Zhang, and K. Kim. Single ion qubit with estimated coherence time exceeding one hour. *Nature Communications*, 12(1):233, 1 2021.

[109] J. Zhang, G. Pagano, P. Hess, A. Kyprianidis, P. Becker, H. Kaplan, A. Gorshkov, Z. Gong, and C. Monroe. Observation of a many-body dynamical phase transition with a 53-qubit quantum simulator. *Nature*, 551(7682):601–604, 2017.

[110] H. Zhong, H. Wang, Y. Deng, M. Chen, L. Peng, Y. Luo, J. Qin, D. Wu, X. Ding, Y. Hu, et al. Quantum computational advantage using photons. *Science*, 370(6523):1460–1463, 2020.

[111] D. Zhu, G. Kahanamoku-Meyer, L. Lewis, C. Noel, O. Katz, B. Harraz, Q. Wang, A. Risinger, L. Feng, D. Biswas, L. Egan, A. Gheorghiu, Y. Nam, T. Vidick, U. Vazirani, N. Yao, M. Cetina, and C. Monroe. Interactive protocols for classically-verifiable quantum advantage. *arXiv preprint arXiv:2112.05156*, 12 2021.

[112] D. Zhu, N. Linke, M. Benedetti, K. Landsman, N. Nguyen, C. Alderete, A. Perdomo-Ortiz, ro, N. Korda, A. Garfoot, C. Brecque, et al. Training of quantum circuits on a hybrid quantum computer. *Science advances*, 5(10):eaaw9918, 2019.